Quantum Monte Carlo simulations of the Fermi-polaron problem and bosons with Gaussian interactions

Dissertation
der Fakultät für Physik
der Ludwig-Maximilians-Universität München

vorgelegt von

Peter Michael Kroiss
aus Penzberg

2016

Erstgutachter: Prof. Dr. Lode Pollet
Zweitgutachter: Prof. Dr. Matthias Punk
Datum der mündlichen Prüfung: 1. Februar 2017
Datum der Einreichung: 16. Dezember 2016

Kurzfassung

Diese Arbeit verwendet Quanten-Monte-Carlo Algorithmen, um bosonische und fermionische Vielteilchensysteme zu untersuchen.

Im ersten Teil wird diagrammatisches Monte Carlo auf den Fall eines Fermipolarons angepasst, eines Systems, welches aus einem Störteilchen und einem nichtinteragierenden Fermibad besteht, welche in resonanter Interaktion zueinander stehen. Es kann gezeigt werden, dass Anregungen mit drei-Teilchen-Loch-Paaren keinen signifikanten Beitrag in einer quasizweidimensionalen Geometrie leisten, wodurch eine nahezu komplette Auslöschung von Beiträgen aus Teilräumen mit einer höheren Anzahl an Teilchen-Loch-Paaren demonstriert wird. Der Übergang zwischen den polaronischen und molekularen Grundzuständen bei einer starken Einschließung in der dritten Ortsrichtung liefert daher eine gute Übereinstimmung mit puren zweidimensionalen Resultaten und Wellenfunktionen mit zwei-Teilchen-Loch-Anregungen.

In dreidimensionalen Fermipolaronen mit ungleichen Massen von Störteilchen und Badatomen können Polaronenergie und Quasiteilchenresiduum für viele Massenverhältnisse akkurat bestimmt werden. Außerdem zeigt die Spektralfunktion des Polarons die Stabilität des Quasiteilchens und die Position des repulsiven Polarons, eines angeregten Zustands. Die quantitative Exaktheit der zwei-Teilchen-Loch-Wellenfunktionen wird untersucht; es zeigt sich, dass es zu einer relativen Schwächung der Polaronenergie im massenungleichen Phasendiagram kommt. Tans Kontaktkoeffizient wird in guter Übereinstimmung mit variationalen Methoden für das massengleiche Fermipolaron bestimmt. Massenungleichheit von Störteilchen und Badatomen wird experimentell mit ultrakalten Atommischungen wie ^{6}Li – ^{40}K untersucht.

Im zweiten Teil der Arbeit wird der Grundzustand eines zweidimensionalen Systems aus spinlosen Bosonen, die über ein repulsives gaußsches Potential interagieren, mittels Pfadintegral Monte Carlo Simulationen erforscht. Das Quantenphasendiagram ist qualitativ identisch zu zweidimensionalen Yukawabosonen. Während das System für schwache Kopplung bei allen Dichten flüssig ist, geht es für starke Interaktion unter Kompression von einer superfluiden Phase zu einem Kristall über, bis es schließlich abermals superfluid wird. Es können keine Anzeichen eines (supersoliden) Clusterkristalls gefunden werden.

Abstract

This thesis deals with the application of current Quantum Monte Carlo algorithms to many-body systems of fermionic and bosonic species.

The first part applies the diagrammatic Monte Carlo method to the Fermi polaron problem, a system of an impurity interacting resonantly with a homogeneous Fermi bath. It is numerically shown that the three particle-hole diagrams do not contribute significantly to the final answer in a quasi-two-dimensional setup, thus demonstrating a nearly perfect destructive interference of contributions in subspaces with higher-order particle-hole lines. Consequently, for strong-enough confinement in the third direction, the transition between the polaron and the molecule ground state is found to be in good agreement with the pure two-dimensional case and agrees very well with the one found by the wave-function approach in the two-particle-hole subspace.

In three-dimensional Fermi-polaron systems with mass imbalance of impurity and bath atoms, polaron energy and quasiparticle residue can be accurately determined over a broad range of impurity masses. Furthermore, the spectral function of an imbalanced polaron demonstrates the stability of the quasiparticle and also allows us to locate the repulsive polaron as an excited state. The quantitative exactness of two-particle-hole wave functions is investigated, resulting in a relative lowering of polaronic energies in the mass-imbalance phase diagram. Tan's contact coefficient for the mass-balanced polaron system is found to be in good agreement with variational methods. Mass-imbalanced systems can be studied experimentally by ultracold atom mixtures such as ^{6}Li – ^{40}K.

In the second part of the thesis, the ground state of a two-dimensional system of Bose particles of spin zero, interacting via a repulsive Gaussian-Core potential, is investigated by means of path integral Monte Carlo simulations. The quantum phase diagram is qualitatively identical to that of two-dimensional Yukawa bosons. While the system is a fluid at all densities for weak coupling, in the strong coupling regime it transitions upon compression from a low density superfluid to a crystal, and then into a reentrant superfluid phase. No evidence of a (supersolid) cluster crystal phase is seen.

Publications

This work is based on three refereed articles published in Physical Review B which are partially reprinted.

Publication I

Peter Kroiß, Lode Pollet

Diagrammatic Monte Carlo study of quasi-two-dimensional Fermi polarons

Physical Review **B** 90, 104510 (2014) [1]

This article presents our results for a three-dimensional Fermi polaron problem with very tight confinement in one direction, rendering the problem essentially two-dimensional. The ground-state of the system changes from a bosonic molecule to a fermionic polaron, agreeing with variational results.

Publication II

Peter Kroiß, Lode Pollet

Diagrammatic Monte Carlo study of a mass-imbalanced Fermi-polaron system

Physical Review **B** 91, 144507 (2015) [2]

This article extends Diagrammatic Monte Carlo to the case of a mass-imbalanced Fermi polaron. After a detailed explanation of the simulation technique, the effects of different masses on polaron energy and residue are presented. An extensive discussion of resummation, regrouping and extrapolation procedures is given.

Publication III

Peter Kroiß, Massimo Boninsegni, Lode Pollet

Ground-state phase diagram of Gaussian-core bosons in two dimensions

Physical Review **B** 93, 174520 (2016) [3]

This article investigates the ground state of two-dimensional bosons with Gaussian-core interactions by means of path integral Monte Carlo simulations. Two phases are found, a superfluid (which is reentrant for high densities) and a crystalline phase. For the case of high particle mass, the reentrant superfluid phase shows unexpected behavior regarding basic analysis quantities such as superfluid density or one-body-density-matrix.

Contents

General introduction

One of the most established methods in computational physics is the Monte Carlo method. With the help of random numbers, it mimics stochastic processes in order to generate a statistical estimate of the true process, converging to the correct result as a consequence of the law of large numbers (within the bounds of an inherent statistical uncertainty).

Back in 1777, Georges-Louis Leclerc, Comte de Buffon performed one of the first applications of Monte Carlo; throwing needles randomly on a striped floor, he estimated the probability that a needle would lie across two stripes [4]. Pierre-Simon Laplace adjusted this method to compute the irrational number π by random sampling [5]. Later, Enrico Fermi used a statistical approach to study the behavior of neutrons interacting with condensed matter [5], before Stanislaw Ulam and Nicholas Metropolis gave a generic description of the Monte Carlo approach [6] in 1949. This was the first time that the name 'Monte Carlo' was used. With the digital revolution, the method spread dramatically, allowing for the simulation of more and more complicated high-dimensional problems. An end to this growth is not in sight – on the contrary, the advent of computers with a large number of cores favors Monte Carlo algorithms as these are often easily parallelized.

The above historical examples demonstrate that the Monte Carlo method is a general strategy that has to be adapted to different systems and situations rather than a specific algorithm. This is especially true in the case of Quantum Monte Carlo, a family of algorithms that apply sampling to an appropriate representation of quantum mechanical problems. The art of Quantum Monte Carlo consists of finding efficient and illuminating representations for these systems.

The main constriction of Quantum Monte Carlo is the sign problem [7] which is due to a near-cancellation of terms with comparable magnitude but different signs. Roughly speaking, the error bars of the observable are on a different scale than the error bars of the Monte Carlo simulation. Typical systems that are likely affected by the sign problem are problems with frustration and fermionic systems.

In this thesis, we will present two different flavors of Quantum Monte Carlo, namely diagrammatic Monte Carlo and path integral Monte Carlo. We apply diagrammatic Monte Carlo, a method based on the stochastic evaluation of Feynman diagrams up to a maximum order limited by the sign problem, to the Fermi-polaron problem, a system in which an impurity (which will be denoted as $\uparrow$) is interacting with a noninteracting fermionic bath (denoted as $\downarrow$). On the other hand, we use path integral Monte Carlo, a technique expanding the thermodynamic partition sum to a so-called worldline representation of geometric paths, to determine the ground-state phase diagram of bosons interacting via an exponential Gaussian-core potential.

More concretely, the Fermi-polaron problem is a limiting case of two-component Fermi gases, a system generating huge interest in the last years because of its BEC-BCS crossover from a Bardeen-Cooper-Schrieffer (BCS) superfluid of paired atoms in momentum space to a Bose-Einstein-condensate (BEC) of spatially localized $(\uparrow,\downarrow)$-molecules [8]. If the Fermi gas is made species-imbalanced, the Fermi-polaron problem is expected to describe the essential physics in the case of few remaining impurities. For example, the BCS side of the crossover translates into a spin-1/2 polaronic state, a dressed impurity propagating through the bath with its quasiparticle residue and effective mass, while the BEC side is seen as the interaction of a tightly bound $(\uparrow,\downarrow)$-state (referred to as molecule [9, 10]) with the remaining bath atoms (cf. Fig. 0.1). This molecular state is bosonic with total spin of 0.

The Fermi-polaron problem was simulated in several experiments [11–13]. As these experiments always use finite concentrations of the impurity species, it is important to note that the

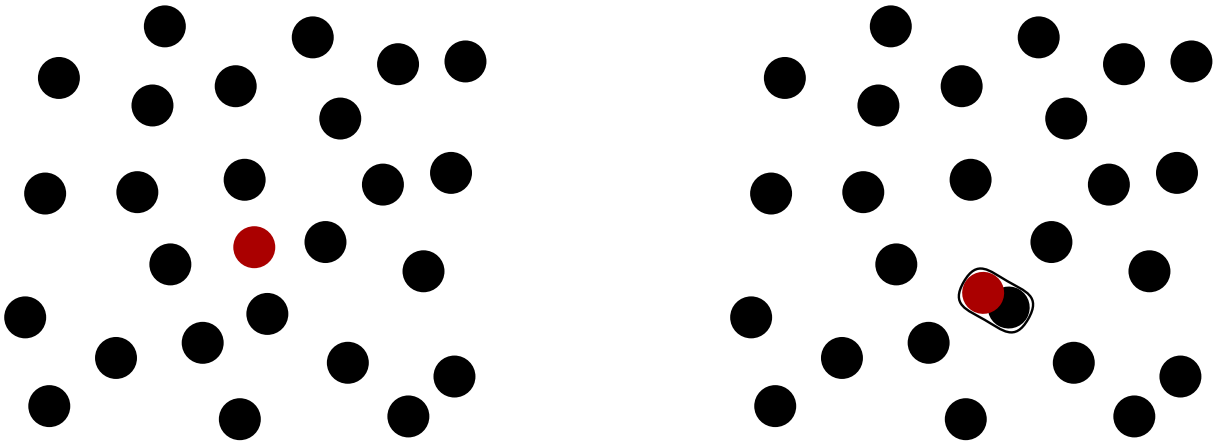

Figure 0.1.: Illustration of polaronic (left) and molecular (right) states.

correspondence between the polaron system and a strongly species-imbalanced Fermi gas is not trivial, as the latter is affected by phase separation into a fully polarized normal phase and an unpolarized superfluid phase [14–16]. However, as a precise calculation of the boundaries of these separated phases depends on polaronic quasiparticle energies and effective masses as parameters for Landau-Pomeranchuk Hamiltonians [15, 17], the Fermi-polaron problem is still able to give valuable insight into the physics of strongly species-imbalanced Fermi gases.

While many studies focused on three-dimensional (3D) polarons [18–28], the problem is also of interest in the reduced dimensionalities of two-dimensional (2D) and one-dimensional (1D) impurity problems [29, 30]. Furthermore, if the gas is confined by a harmonic trap, intermediate dimensionalities can be realized as well, e.g., quasi-2D polarons, a system that connects directly with experiments[1] in contrast to pure 2D geometries. For the latter, it was initially believed that no molecular ground state is stable [32], but treating polaronic and molecular variational wave-functions on a similar footing finally showed that 2D polarons experience a polaron-molecule transition as well [33].

Another aspect of the Fermi-polaron problem was investigated by varying the relative mass of impurity and bath particles: For increasing mass of the bath particles, Mathy et al. showed that a third distinct ground state is possible: a trimer consisting of two ↑-atoms and the impurity [17, 34]. Tetramers and agglomerations of more particles were not found to be stable [17, 35, 36]. Note that the trimer remains stable in pure-2D systems [14].

Since the diagrammatic Monte Carlo method simulates the full many-body system without any major approximation, an implementation for the Fermi-polaron problem promises to shed further light on two major questions:

- Is the variational ansatz of Ref. [33] an accurate description of the polaron-molecule transition in two-dimensional geometries?
- Is the ground-state phase diagram of Ref. [17] for mass-imbalanced polaron systems compatible with a full many-body diagrammatic expansion?

Apart from addressing these questions, the first part of this thesis examines several quasiparticle properties such as energy, residue and spectral function that enable a better understanding of the quality of the variational ansätze. In addition, we will give a detailed discussion of the Fermi-polaron diagrammatic series with an emphasis on its convergence properties for reordered or resummed series. We present a special regrouping in terms of particle-hole diagrams that

[1] Here, the effective harmonic potential is generated by an external laser [31].

combines the advantages of diagrammatic Monte Carlo with the advantages of variational methods.

The second part of this work deals with the Gaussian-core model, a system of bosons with Gaussian interactions confined to a periodic box. This model was introduced by Stillinger [37] as a model system for interpenetrating polyatomic molecules with favorable mathematical properties. The original paper showed that the classical three-dimensional Gaussian-core system is characterized by the following temperature regions:

- For high temperature, the system is fluid.
- For intermediate temperature, the system is fluid in the limit of high and low densities with a crystal phase in-between, where the high-density fluid region is called reentrant. The crystal region is enhanced for decreasing temperature.
- For zero temperature, the system is a crystal for all densities.

More recent studies showed that this picture remains qualitatively correct in a numerical simulation of the system by classical Monte Carlo [38]. Furthermore, the crystal phase could be divided into regions of face-centered-cubic (fcc) and body-centered-cubic (bcc) structure.

A later paper extended this study to the two-dimensional case [39] and showed that the qualitative phase diagram of Ref. [37] remains accurate (where the crystalline phase is given by a triangular lattice). Remarkably, the fluid and the crystal phase were separated by a tiny region of orientational order; several predictions of the Kosterlitz-Thouless-Halperin-Nelson-Young theory of two-dimensional melting were found to be fulfilled for this finite system.

It is an interesting question whether these effects persist for a quantum mechanical Gaussian-core system. In particular, quantum fluctuations are expected to modify the ground state of the system by making crystalline order weaker. We perform extensive path integral Monte Carlo simulations in order to map out the complete ground-state phase diagram for different densities and values of the quantum-mechanical coupling. It is particularly important to examine whether the system admits unconventional states such as *supersolid* ground states [40] or cluster crystals [41].

The structure of this thesis is as follows. In Chapter 1, a brief summary of the Monte Carlo method is given, focusing on problems and techniques that will be encountered in later chapters. Chapter 2 reviews quantum scattering in two and three dimensions, a formalism that introduces the scattering length, a specific two-body property which will later be used to renormalize the interaction.

The thesis then advances on to the Fermi-polaron problem in the context of diagrammatic Monte Carlo. This will be the topic of Part 1. The Fermi-polaron system is presented in Chapter 3 in a diagrammatic approach where special emphasis is given to a clean introduction of the respective T matrices in two, three and quasi-two-dimensional situations. Chapter 4 defines our diagrammatic Monte Carlo algorithm together with our resummation and extrapolation framework. In Chapter 5, our results for a quasi-two-dimensional geometry are discussed in detail. Mainly, the position of the polaron-molecule transition is estimated in a full diagrammatic extrapolation to infinite order. This chapter also presents a regrouping in terms of particle-hole diagrams. Chapter 6 concludes the first part by our findings for a three-dimensional polaron with mass imbalance by calculating basic quasiparticle properties and analyzing the mass-imbalanced phase diagram.

Moving on to bosonic systems, Part 2 begins with a detailed derivation of the path integral Monte Carlo method in Chapter 7. Next, Chapter 8 uses this method for a two-dimensional system of bosons interacting by a Gaussian-core potential and calculates the ground-state phase diagram of this system. Chapter 9 highlights our findings and gives a short outlook.

1

Preliminaries: The Monte Carlo method

The main numerical tool of this thesis is the Monte Carlo method. It allows for the computation of high-dimensional integrals with an error that has favorable scaling with the dimension of the integrals. Since Monte Carlo is based on a sampling of an appropriate configuration space, it is a flexible method with applications ranging from many-body physics to the modeling of financial markets. As the basic principles of Monte Carlo are discussed in a huge variety of textbooks and reviews, we restrict ourselves to a short summary clarifying our notations. A more detailed introduction is given in Ref. [4].

Markov chain sampling In our Monte Carlo sampling, we will always build a Markov chain of appropriate configurations in a random way. Markov chain sampling has to be used for complicated situations where direct sampling is not feasible. From a starting configuration, the Markov chain gradually transforms this configuration in order to decorrelate the samples; after several steps, an independent configuration is reached, where this number of steps is linked to the autocorrelation time of the simulation. In order to generate samples according to the underlying probability density, global balance has to be established between the configurations [4]. Commonly, this is done by using detailed balanced and the Metropolis-Hastings algorithm [42]. The transition probability $P(x \to x')$ between configurations x and x' is given by

$$P(x \to x') = \min\left(1, \frac{W(x')}{W(x)}\right), \tag{1.1}$$

where W labels the weight of the configurations. Generally, this weight corresponds to the integrand. The transition probability is the probability with which a proposed move from x to x' is accepted.

In many cases, it is advantageous to guide the Markov sampling by proposing configurations with an increased weight more often, i.e., configurations are selected according to some *a priori* probability $\mathcal{A}$ for a move from x to x'. Incorporating this into the Metropolis algorithm yields

$$P(x \to x') = \min\left(1, \frac{\mathcal{A}(x' \to x)W(x')}{\mathcal{A}(x \to x')W(x)}\right). \tag{1.2}$$

Apart from balance, there is another crucial requirement for Markov chain algorithms: Starting from a random configuration, it must be possible to reach any configuration in a finite number of Monte Carlo steps. This is called ergodicity.

The Markov chain approach has several common problems:

1. If the sampling domain consists of more than one region of significant weight, it could happen that these regions become practically disconnected with local Markov chain updates. Often, this problem can be solved by further updates that connect the different branches in a direct way.

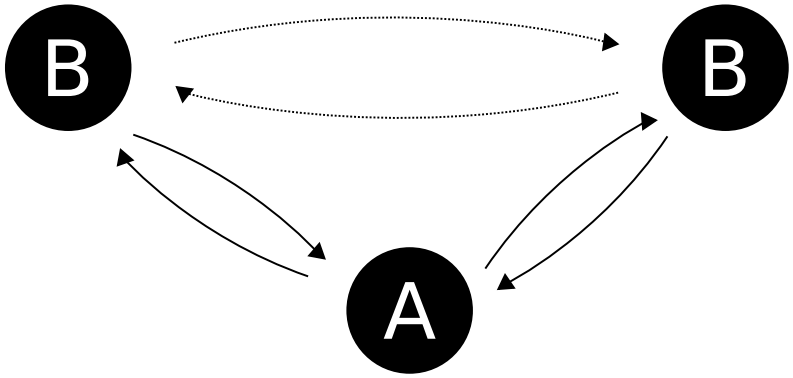

Figure 1.1.: Illustration of a common problem of establishing detailed balance.

2. A good design of the Markov chain updates is fundamental because naive updates could increase the autocorrelation time of the simulation to times that exceed the program runtime.

3. Before measurements are performed, a certain number of Markov chain steps has to be executed to let the system equilibrate – a process that is called thermalization. As a rule of thumb, about one fifth of the simulation time should be spent thermalizing [43].

4. If a statistical physics simulation is performed with Monte Carlo, the weights usually include exponential functions. It is important to handle these functions in a controlled way: If the argument of the function is too big (which happens on the order of 100), the numerical evaluation will overflow and return undefined behavior or infinity. Most of these situations can be cured by using the exponential identity $e^a \cdot e^b = e^{a+b}$ and by manually returning a very high number or 0 for large absolute values of the argument.

5. A subtle issue is illustrated in Fig. 1.1. From a starting configuration A, a configuration B can be reached by two different updates. If the dotted updates between the two representations of B do not exist, the total weight of B will be affected by double counting. If only one of the dotted updates is implemented, detailed balance will be broken. Even including both dotted updates does not remove the double counting.

Measurements and error analysis A common goal of Monte Carlo simulations is the evaluation of observables, i.e., the statistical average of a quantity measured on a regular basis during the simulation. If a sufficient number of independent samples is generated, this can be expected to converge towards the actual physical value according to the central limit theorem [4]. In practice, a challenging question is whether the simulation already produced decorrelated configurations or not. Hence, a detailed error analysis is required, enabling the extraction of honest error bars and autocorrelation times from the Monte Carlo data. A common method for this purpose is the binning analysis [43]. By grouping successive measurements, the naive error bar of each hierarchical level is determined until saturation of error bars is observed. Typically, the naive error bar of correlated data is too small since the correlations pretend reduced fluctuations. For this reason, a controlled error analysis is of paramount importance. Conveniently, the error estimation can be left to general Monte Carlo libraries like ALPS [44]. Note that the error scales as $1/\sqrt{N}$ where N is the number of independent measurements.

Having established error estimation, this brings us to the main drawback of Monte Carlo – the sign problem, which occurs if the weights of the simulation are not strictly sign-positive. For the case of conventional Quantum Monte Carlo, this results in observable errors that scale

exponentially with the particle number and inverse temperature [7], making it unfeasible to reach novel parameter regimes in many cases. This is due to a near cancellation of large positive and negative contributions that are of the same magnitude. Since the anticommutation relations of fermions usually introduce sign alternation, many fermionic systems are effected by the sign problem. No generic solution to the sign problem is possible unless there are polynomial-time solutions to NP problems [7]. This does not exclude that the sign problem can be circumvented in specific cases.

Normalization Given that our Monte Carlo simulations will use two different approaches for normalization, we will give a short revision of these concepts. The first situation is given by programs that need to calculate thermodynamic expectation values of the form

$$\langle \mathcal{O} \rangle = \frac{\mathrm{tr}\left(\hat{\mathcal{O}} e^{-\beta \hat{H}}\right)}{\mathrm{tr}\left(e^{-\beta \hat{H}}\right)}, \tag{1.3}$$

where $\mathcal{O}$ is a quantum-mechanical observable, β is the inverse temperature and $\hat{H}$ is the Hamiltonian of the system. The path integral Monte Carlo simulation of the second part of this thesis will be corresponding to this class. The usual strategy to get access to $\langle \mathcal{O} \rangle$ is to start with an appropriate Markov chain that samples the partition function $Z = \mathrm{tr}(e^{-\beta \hat{H}})$. Once this works, it is often possible to find a simple expression that assigns the corresponding value of the observable $\mathcal{O}$ to the current sample of Z, allowing to keep separate estimators for numerator and denominator of Eq. (1.3). Hence, the normalization is usually straightforward because the only important aspect is the ratio of $\mathrm{tr}(\hat{\mathcal{O}} e^{-\beta \hat{H}})$ and Z (and not their absolute value).

In the second situation, this is different – here, the goal is to calculate integrals like

$$G = \int \mathrm{d}x \; g(x) \tag{1.4}$$

for some given function g. The diagrammatic Monte Carlo routine of the first part of this thesis is an example for situation two. For simplicity, we assume $g(x) > 0$. A common strategy which solves the problem of normalizing the results is the use of a *fake integral* $F = \int \mathrm{d}x f(x)$ which is analytically known so that a measurement of G relative to F becomes possible, i.e.,

$$\int \mathrm{d}x \; g(x) = \frac{\sum_{\mathrm{MC}} \delta^{(g)}}{\sum_{\mathrm{MC}} \delta^{(f)}} \int \mathrm{d}x f(x), \tag{1.5}$$

where $\sum_{\mathrm{MC}}$ is the sum of Monte Carlo samples and $\delta^{(g)}$ ($\delta^{(f)}$) is one for measurements in the G (F) sector and zero otherwise. Again, we assume that $f(x) > 0$. The Markov chain upon which this estimation is built is specified by the following updates:

- *First-to-Fake* and *Fake-to-First*,
- *Change-Fake* (self-inverse),
- *Change-First* (self-inverse).

The setup is sketched in Fig. 1.2. We assume that each update is called with the same probability[1]; if *First-to-Fake* or *Change-First* are to be applied on the *fake integral*, these updates have to be rejected. The same is true for *Fake-to-First* and *Change-Fake* in the G sector.

[1] This is of purely illustrative purpose. In practice, the probabilities of update selection should be designed to fit the concrete code, implying that the transition probabilities have to be adjusted.

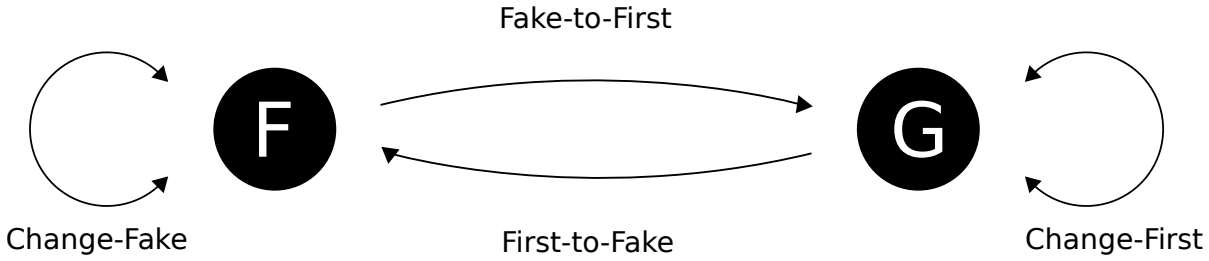

Figure 1.2.: Basic scheme for the normalization with *fake integrals*.

In the simplest case, *Change-First* only attempts to change the x-value of the integrand from x to x' with transition probability

$$P_{\mathrm{CG}}(x \to x') = \min\left(1, \frac{g(x')}{g(x)}\right). \tag{1.6}$$

Change-Fake is constructed in the same way. The updates *First-to-Fake* and *Fake-to-first* link F with G. If the system is sampling in the *fake integral* sector at x, the transition probability to G is

$$P_{\mathrm{FG}}(F \to G) = \min\left(1, \frac{g(x)}{f(x)}\right), \tag{1.7}$$

while the inverse move from G to F has the transition probability

$$P_{\mathrm{GF}}(G \to F) = \min\left(1, \frac{f(x)}{g(x)}\right). \tag{1.8}$$

If detailed balance is fulfilled between the *fake integral* and G in this way, full numerical control of the normalization is established in a generic way.

Technical setup The chapter is concluded by a quick overview of technical concepts that can help to produce efficient and correct Monte Carlo programs:

- Parallelization of Monte Carlo codes is constructed in a straightforward way by starting the same simulation with different seeds. Although this approach requires each thread to thermalize independently, the speed loss in comparison to a truly parallelized code is typically negligible. When the simulation is finished, the acquired data has to be combined and a normal statistical analysis can be performed.

- Since the error analysis depends on huge amounts of statistical data, an appropriate data structure has to be used to store this data in an efficient and tidy way. We recommend the use of the *Hierarchical data format* (HDF) to organize data. It combines archiving, compression and data structuring in a portable and open format. Furthermore, it can handle large amounts of numerical measurements.

- Monte Carlo simulations normally require the use of a pseudorandom number generator (PRNG) in combination with several distributions that map the output of the pseudorandom number generator to the desired range. It is necessary to use a PRNG which ensures that its period is long enough. Note that there is a new development which is claimed to be superior to the usual PRNGs in terms of predictability, statistical quality, time performance and disk space usage [45].

2
Preliminaries: Scattering Theory

This chapter reviews the quantum-mechanical two-body scattering theory in two and three dimensions[1] for particles of masses $m_\uparrow$ and $m_\downarrow$. If the position and momentum operators of the two particles are denoted by $\hat{\boldsymbol{r}}_\uparrow$, $\hat{\boldsymbol{r}}_\downarrow$, $\hat{\boldsymbol{p}}_\uparrow$ and $\hat{\boldsymbol{p}}_\downarrow$, the system is described by a Schrödinger equation

$$\left(\frac{\hat{\boldsymbol{p}}_\uparrow^2}{2m_\uparrow} + \frac{\hat{\boldsymbol{p}}_\downarrow^2}{2m_\downarrow} + \hat{V}(\hat{\boldsymbol{r}}_\uparrow, \hat{\boldsymbol{r}}_\downarrow)\right)|\Psi\rangle = E_{\mathrm{tot}}|\Psi\rangle \tag{2.1}$$

for a two-body state $|\Psi\rangle$, potential energy operator $\hat{V}$ (which is assumed to be a function of $\hat{\boldsymbol{r}}_\downarrow$ and $\hat{\boldsymbol{r}}_\uparrow$ only) and total energy E_{tot}. The total mass $M = m_\uparrow + m_\downarrow$ and the reduced mass $m_r = (1/m_\uparrow + 1/m_\downarrow)^{-1}$ are introduced canonically, just as the center-of-mass position $\boldsymbol{R} = \frac{m_\downarrow \boldsymbol{r}_\downarrow + m_\uparrow \boldsymbol{r}_\uparrow}{M}$, the relative position $\boldsymbol{r} = \boldsymbol{r}_\uparrow - \boldsymbol{r}_\downarrow$, the total momentum $\boldsymbol{P} = \boldsymbol{p}_\uparrow + \boldsymbol{p}_\downarrow$, the relative momentum $\boldsymbol{p} = \frac{m_\downarrow \boldsymbol{p}_\uparrow - m_\uparrow \boldsymbol{p}_\downarrow}{M}$ and the respective operators. We assume $\hbar = 1$.

If $\hat{V}$ only depends on the relative distance of the particles, Eq. (2.1) can be rewritten as

$$\left(\frac{\hat{\boldsymbol{P}}^2}{2M} + \frac{\hat{\boldsymbol{p}}^2}{2m_r} + \hat{V}(\hat{\boldsymbol{r}})\right)|\Psi\rangle = E_{\mathrm{tot}}|\Psi\rangle. \tag{2.2}$$

Switching to the position representation yields

$$\left(-\frac{\boldsymbol{\nabla}_{\boldsymbol{R}}^2}{2M} - \frac{\boldsymbol{\nabla}_{\boldsymbol{r}}^2}{2m_r} + V(\boldsymbol{r})\right)\Psi(\boldsymbol{R}, \boldsymbol{r}) = E_{\mathrm{tot}}\Psi(\boldsymbol{R}, \boldsymbol{r}). \tag{2.3}$$

This equation of two variables can be decoupled by the separation ansatz $\Psi(\boldsymbol{R}, \boldsymbol{r}) = \chi(\boldsymbol{R})\psi(\boldsymbol{r})$ into Schrödinger equations for total and relative motion:

$$-\frac{\boldsymbol{\nabla}_{\boldsymbol{R}}^2}{2M}\chi(\boldsymbol{R}) = E_{\mathrm{com}}\chi(\boldsymbol{R}) \tag{2.4}$$

$$\left(-\frac{\boldsymbol{\nabla}_{\boldsymbol{r}}^2}{2m_r} + V(\boldsymbol{r})\right)\psi(\boldsymbol{r}) = E\psi(\boldsymbol{r}). \tag{2.5}$$

E is the energy of relative motion, while E_{com} is the center-of-mass energy. The total energy E_{tot} is given by $E_{\mathrm{tot}} = E + E_{\mathrm{com}}$. As the solution of the center-of-mass Schrödinger equation is just a plain wave with energy E_{com}, the relevant physics of the problem is contained in the Schrödinger equation that describes the relative motion (Eq. (2.5)) which has to be decomposed further. In the following sections we investigate two and three dimensional scattering, respectively. Both sections comment on the low-energy behavior which is important when analyzing dynamics of ultracold atoms.

[1] Section 2.1 is reprinted from Ref. [46] for completeness.

2.1. Scattering in three dimensions

Scattering amplitude Starting point of the analysis is the Schrödinger equation for the relative motion

$$\left(-\frac{\boldsymbol{\nabla}_{\boldsymbol{r}}^2}{2m_r}+V(\boldsymbol{r})\right)\psi_{\boldsymbol{k}}(\boldsymbol{r})=E\psi_{\boldsymbol{k}}(\boldsymbol{r}). \tag{2.6}$$

Here, $\psi_{\boldsymbol{k}}(\boldsymbol{r})$ is labeled with the relative momentum $\boldsymbol{k}$ and $k^2\equiv 2m_rE$. Expressing the Laplacian in spherical coordinates gives

$$\left(-\frac{1}{r^2}\frac{\partial}{\partial r}\left(r^2\frac{\partial}{\partial r}\right)-\frac{1}{r^2\sin\theta}\frac{\partial}{\partial\theta}\left(\sin\theta\,\frac{\partial}{\partial\theta}\right)-\frac{1}{r^2\sin^2\theta}\frac{\partial^2}{\partial\phi^2}\right)\psi_{\boldsymbol{k}}(\boldsymbol{r})=\left[k^2-2m_rV(r)\right]\psi_{\boldsymbol{k}}(\boldsymbol{r}). \tag{2.7}$$

Physically, the scattering wave-function is expected to be a superposition of the incoming plane wave (which we take to be moving along $\hat{\boldsymbol{e}}_z$) and the outgoing scattered wave for distances far from the scattering center ($kr\gg 1$), i.e.,

$$\psi_{\boldsymbol{k}}(\boldsymbol{r})\sim e^{ikz}+f_k(\theta)\frac{e^{ikr}}{r}, \tag{2.8}$$

where θ is the angle between $\boldsymbol{r}$ and $\boldsymbol{k}$ and $\boldsymbol{kr}=kz$. Note that for the case of a spherically symmetric potential, there is no dependence on the azimuthal angle ϕ. $f_k(\theta)$ is called scattering amplitude. It is the basic quantity of scattering theory and allows the calculation of the differential cross section $\frac{\mathrm{d}\sigma}{\mathrm{d}\Omega}$ by [47]

$$\frac{\mathrm{d}\sigma}{\mathrm{d}\Omega}=\left|f_k(\theta)\right|^2. \tag{2.9}$$

Partial waves In a second step, we introduce the partial wave expansion. In the limit $kr\gg 1$, Eq. (2.7) is solved by

$$\psi_{\boldsymbol{k}}(\boldsymbol{r})\sim\sum_{l=0}^{\infty}\frac{(2l+1)}{ikr}P_l(\cos\theta)\left(e^{2i\delta_l}e^{ikr}-(-1)^le^{-ikr}\right)A_l. \tag{2.10}$$

Here, spherical coordinates are used, A_l is a set of expansion coefficients, P_l denotes the Legendre polynomial of degree l and δ_l labels the scattering phase shifts. A detailed derivation of this equation is given in Appendix A. Note that we omit the k-dependence of δ_l for optical clarity. Since we want to match this result with the expected asymptotic form of Eq. (2.8), the latter also has to be written in terms of partial waves, i.e.,

$$\psi_{\boldsymbol{k}}(\boldsymbol{r})\sim\sum_{l=0}^{\infty}\frac{2l+1}{2ikr}P_l(\cos\theta)\left(e^{ikr}(1+2ikf_l)-(-1)^le^{-ikr}\right) \tag{2.11}$$

with expansion coefficients f_l (which implicitly depend on k). Again, this statement is derived in Appendix A. Comparing these equations, it follows that $A_l=\frac{1}{2}$ and $e^{2i\delta_l}=1+2ikf_l$. This means that the scattering amplitude is

$$f_k(\theta)=\sum_{l=0}^{\infty}(2l+1)P_l(\cos\theta)\frac{e^{2i\delta_l}-1}{2ik}. \tag{2.12}$$

Scattering of indistinguishable particles If particles are not distinguishable, the correct symmetry properties have to be incorporated. Assume that our system is fermionic. The total wave function Ψ of two indistinguishable fermions has to be antisymmetric:

$$\Psi(\boldsymbol{R}, \boldsymbol{r}) = -\Psi(\boldsymbol{R}, -\boldsymbol{r}). \tag{2.13}$$

Note that $\boldsymbol{R} \to \boldsymbol{R}$ and $\boldsymbol{r} \to -\boldsymbol{r}$ under particle exchange. This means that the wave function of relative motion has to be antisymmetric to ensure overall antisymmetry. Eq. (2.8) is antisymmetrized in a straightforward way:

$$\psi_{\boldsymbol{k}}(\boldsymbol{r}) \sim \frac{e^{ikz} - e^{-ikz}}{\sqrt{2}} + \frac{f_k(\theta) - f_k(\pi - \theta)}{\sqrt{2}} \frac{e^{ikr}}{r}. \tag{2.14}$$

The only θ-dependence of $f_k(\theta)$ is $P_l(\cos\theta)$; this means that the relations $\cos(\pi - \theta) = -\cos\theta$ and $P_l(-x) = (-1)^l P_l(x)$ imply that $f_k(\theta)$ and $f_k(\pi - \theta)$ cancel for even l. Consequently, only odd partial waves contribute to the scattering of indistinguishable particles.

Furthermore, not all partial waves can contribute to scattering at ultracold temperatures. The maximal angular momentum l of relative motion can be estimated by ξk, where ξ labels the range of the potential as defined in Ref. [48]. The ultralow energy limit can be expressed by the condition $1/k \gg \xi$ – the details of the potential are not resolved and the pseudo-potential approximation presented in Chapter 3 becomes valid. Rewriting in terms of l yields

$$1 \gg \xi k = l. \tag{2.15}$$

Finally, the reason why the noninteracting spin-polarized Fermi gas is a good approximation at low temperature is that all $l > 0$ are energetically suppressed while $l = 0$ is not allowed because of the indistinguishability of fermions.

Low-energy scattering Last, we introduce the two-body scattering length, a quantity which will be needed to relate physically accessible parameters to the bare coupling constant in the derivation of the T Matrix. Starting with the scattering amplitude for $l = 0$,

$$f_k(\theta) = P_0(\cos\theta) \frac{e^{2i\delta_0} - 1}{2ik} = \frac{e^{2i\delta_0} - 1}{2ik}, \tag{2.16}$$

a rewriting yields

$$f_k(\theta) = e^{i\delta_0} \frac{e^{i\delta_0} - e^{-i\delta_0}}{2ik} = \frac{\sin\delta_0}{e^{-i\delta_0} k} = \frac{1}{k\cot\delta_0 - ik}.$$

Defining the scattering length $a_{3\mathrm{D}} = -\lim\limits_{k\to 0^+} \frac{\delta_0}{k}$, the *effective range expansion* is given by [49]

$$f_k(\theta) = f_k = \frac{1}{k\cot\delta_0 - ik} = \frac{1}{-\frac{1}{a_{3\mathrm{D}}} - ik + \frac{r_{\mathrm{eff}} k^2}{2} + \ldots}. \tag{2.17}$$

In the denominator, the effective range r_{eff} was introduced [50]. Note that δ_0 is a function of k; as the definition of the scattering length should give a nonzero value, this means that $\delta_0 \sim k$ for low k. In principle, physical systems allow arbitrary effective ranges r_{eff}. Nevertheless, broad Feshbach resonances[2] admit [48, 51] $r_{\mathrm{eff}} = 0$. For unitary interaction strength ($a_{3\mathrm{D}}^{-1} \to 0$), the

[2] These are usually used to tune the scattering length to the desired value.

scattering amplitude takes the simple form

$$f_k = \frac{i}{k}. \tag{2.18}$$

For an alternative way of introducing the scattering length, consult Appendix A. This alternative approach is similar to the introduction of the two-dimensional scattering length.

2.2. Scattering in two dimensions

Scattering amplitude Starting point[3] for a two-dimensional system is again the Schrödinger equation for the relative motion of two particles:

$$-\frac{\boldsymbol{\nabla}_{\boldsymbol{r}}^2 \psi_{\boldsymbol{k}}(\boldsymbol{r})}{2m_r} + V(\boldsymbol{r})\psi_{\boldsymbol{k}}(\boldsymbol{r}) = E\psi_{\boldsymbol{k}}(\boldsymbol{r}). \tag{2.19}$$

With $k^2 \equiv 2m_r E$, one gets by using cylindrical coordinates:

$$\frac{1}{r}\frac{\partial}{\partial r}\left(r\frac{\partial \psi_{\boldsymbol{k}}(r,\phi)}{\partial r}\right) + \frac{1}{r^2}\frac{\partial^2 \psi_{\boldsymbol{k}}(r,\phi)}{\partial \phi^2} + \left(k^2 - 2m_r V(r,\phi)\right)\psi_{\boldsymbol{k}}(r,\phi) = 0. \tag{2.20}$$

The scattering amplitude $f_k(\phi)$ is asymptotically defined as [48]

$$\psi_{\boldsymbol{k}}(\boldsymbol{r}) \underset{kr\to\infty}{\longrightarrow} e^{ikx} - \sqrt{\frac{i}{8\pi}} f_k(\phi)\frac{e^{ikr}}{\sqrt{kr}} \tag{2.21}$$

which can be understood as a superposition of an incoming plane wave and an outgoing circular wave, where we take the incoming wave to be propagating along $\hat{\boldsymbol{e}}_x$, and $\phi = 0$ to be the angle corresponding to this direction. The additonal factors are of purely conventional purpose. This form now has to be matched with the asymptotic behavior of the wave function $\psi_{\boldsymbol{k}}(r,\phi)$ for large r, where the potential is essentially zero.

Partial waves The partial wave expansion of the solution of Eq. (2.20) in the limit $kr \gg 1$ is

$$\psi_{\boldsymbol{k}}(\boldsymbol{r}) \sim \sum_{m=0}^{\infty} A_m \frac{\sqrt{2}}{\pi\sqrt{kr}}\cos(m\phi)\frac{1}{2}\left(e^{i(kr-\frac{m\pi}{2}-\frac{\pi}{4}+\delta_m)} + e^{-i(kr-\frac{m\pi}{2}-\frac{\pi}{4}+\delta_m)}\right), \tag{2.22}$$

as proven in Appendix A. Here, cylindrical coordinates were used, A_m is a set of expansion coefficients and δ_m denotes the scattering phase shift. Note that we omit the k-dependence of δ_m for optical clarity. The asymptotic form of Eq. (2.21) can be written in a similar manner as

$$\psi_{\boldsymbol{k}}(\boldsymbol{r}) \sim \sum_{m=0}^{\infty} \epsilon_m i^m \cos(m\phi)\sqrt{\frac{2}{\pi kr}}\frac{1}{2}\left(e^{i(kr-\frac{m\pi}{2}-\frac{\pi}{4})} + e^{-i(kr-\frac{m\pi}{2}-\frac{\pi}{4})}\right) - \sqrt{\frac{i}{8\pi}} f_k(\phi)\frac{e^{ikr}}{\sqrt{kr}} \tag{2.23}$$

for some coefficients ϵ_m. This is also shown in Appendix A, together with a comparison of these equations that makes it possible to get an expression of the scattering amplitude in terms of the scattering phase shifts. This implies that the scattering amplitude is

$$f_k(\phi) = -4\sum_{m=0}^{\infty} \cos(m\phi)\epsilon_m e^{i\delta_m}\sin(\delta_m). \tag{2.24}$$

[3] This section follows Refs. [48, 52–54] in large parts.

Scattering of indistinguishable fermions Just as in three dimensions, the particle statistics have to be reflected by a properly antisymmetrized wave function. The antisymmetrized asymptotic form of the scattering wave function is (cf. Eq. (2.14))

$$\psi_{\boldsymbol{k}}(\boldsymbol{r}) \sim \frac{e^{ikx} - e^{-ikx}}{\sqrt{2}} - \sqrt{\frac{i}{8\pi}} \frac{f_k(\phi) - f_k(\pi + \phi)}{\sqrt{2}} \frac{e^{ikr}}{\sqrt{kr}}. \tag{2.25}$$

Since $\cos(m(\phi + \pi)) = (-1)^m \cos(m\phi)$, $f_k(\phi)$ and $f_k(\pi + \phi)$ cancel out for even m. This means that there is no scattering of indistinguishable fermions at very low temperature, just like in three dimensions. Consequently, a spin-polarized Fermi gas will be effectively noninteracting at low temperatures.

Low energy scattering As a last point on two-dimensional scattering, the behavior of distinguishable particles with low energy is discussed. Appendix A shows that the low energy scattering amplitude is

$$f_k(\phi) = \frac{4\pi}{-2\ln(ka_{2\mathrm{D}}) + i\pi}, \tag{2.26}$$

where the two-dimensional scattering length $a_{2\mathrm{D}}$ was introduced.

Part I.

Fermionic many-body physics: Diagrammatic Monte Carlo

3 The Fermi-polaron problem

The Fermi-polaron problem [29] combines a noninteracting fermionic bath of N atoms with one impurity atom interacting resonantly with the majority atoms. Such a system can be modeled by using different spin states of the same particle, or by introducing a distinct atom species. Since there is no interaction among the bath atoms and since the impurity is a single atom, it follows that the Hamiltonian is

$$\hat{H} = \sum_{\boldsymbol{p},\sigma} \epsilon_{p,\sigma} \hat{c}^\dagger_{\boldsymbol{p},\sigma} \hat{c}_{\boldsymbol{p},\sigma} + g \sum_{\boldsymbol{p},\boldsymbol{p'},\boldsymbol{q}} \hat{c}^\dagger_{\boldsymbol{p}+\boldsymbol{q},\uparrow} \hat{c}^\dagger_{\boldsymbol{p'}-\boldsymbol{q},\downarrow} \hat{c}_{\boldsymbol{p'},\downarrow} \hat{c}_{\boldsymbol{p},\uparrow}. \tag{3.1}$$

Here, $\hat{c}_{\boldsymbol{p},\sigma}$ ($\hat{c}^\dagger_{\boldsymbol{p},\sigma}$) denotes the conventional annihilation (creation) operator of momentum $\boldsymbol{p}$ and species $\sigma = (\uparrow,\downarrow)$, where the notation is conveniently chosen as in a spin system, without necessarily referring to spins. The impurity atom is identified by $\downarrow$. The dispersion $\epsilon_{p,\sigma}$ is given by $\epsilon_{p,\sigma} = \frac{p^2}{2m_\sigma}$, while g labels the bare coupling. Later, this coupling will be replaced by the two-body scattering lengths $a_{3\mathrm{D}}$ and $a_{2\mathrm{D}}$, respectively [48, 51]. These quantities are experimentally accessible and ensure that our results are model-independent and universal. The simulations will be carried out in d dimensions at zero temperature, where $d = 2$ or $d = 3$. The Fermi momentum p_F and its corresponding Fermi energy E_F are linked by the usual relation $E_F = \frac{p_F^2}{2m_\uparrow}$ and set our units of inverse length and energy. These quantities always refer to the majority species. Note that Eq. (3.1) describes a realistic system because at ultracold temperatures, s-wave scattering is not possible, while scattering through higher partial waves is energetically suppressed as discussed in Chapter 2.

The goal of the rest of this chapter is to establish the Feynman series of the Fermi polaron. At first, an overview of Chevy's variational technique is given in Sec. 3.1. This ansatz will turn out to be closely connected with our diagrammatic Monte Carlo approach. Sec. 3.2 introduces the propagators and vertices of our model. In Secs. 3.3, 3.4 and 3.5, the T matrix is derived in three, two and quasi-two-dimensional setups. The chapter is concluded by the full diagrammatic expansions of polarons (Sec. 3.6) and molecules (Sec. 3.7).

3.1. Variational techniques

One of the most successful strategies to tackle the Hamiltonian (3.1) is the use of a so-called *Chevy ansatz* with wave functions of the form

$$|\psi\rangle = \alpha_0 c^\dagger_{\boldsymbol{p},\downarrow}|0\rangle + \sum_{q>p_F}^{p'<p_F} \alpha_{\boldsymbol{p'},\boldsymbol{q}} c^\dagger_{\boldsymbol{p}-\boldsymbol{q}+\boldsymbol{p'},\downarrow} c^\dagger_{\boldsymbol{q},\uparrow} c_{\boldsymbol{p'},\uparrow}|0\rangle, \tag{3.2}$$

where $|0\rangle$ labels the free sea of $\uparrow$-atoms and all α are parameters [18]. If terms with a higher number of particle-hole creations are inserted, this ansatz increases its quantitative exactness and

eventually spans a whole basis for an infinite sequence of terms. Using the quantum mechanical variational method with Eq. (3.2) as trial wave function and variational parameters α is a simple way of approximating the quasiparticle energy and residue of the Fermi-polaron problem.

Ansatz (3.2) was introduced by Chevy in 2006 [18] in order to investigate the species-imbalanced Fermi gas experiments of Refs. [55–57] theoretically. In these works, the Fermi gas was seen to split into a central core of paired (superfluid) atoms surrounded by a normal gas of majority atoms beyond some critical polarization and interaction strength (where the latter was tuned by Feshbach resonances [58]). Chevy used the energy of the corresponding Fermi-polaron problem to estimate the chemical potential of the minority species which helped to localize the phase boundaries of the species-imbalanced Fermi gas [18].

In a next step, Combescot et al. established the correspondence between the variational approach and a so-called T matrix approximation [19]. Secs. 3.3, 3.4 and 3.5 will give an in-depth introduction to this quantity. The important thing to stress is that Ref. [19] showed that analyzing the Fermi-polaron problem by a first-order diagrammatic approach is identical to the *Chevy ansatz*; in Chapter 5, we will show that this one-to-one correspondence remains true for higher approximation orders. Note that Ref. [19] also generalized the problem to unequal masses of impurity and bath atoms which is relevant for atomic mixtures such as ^{6}Li – ^{40}K.

In 2008, Combescot et al. extended the *Chevy ansatz* by including further particle-hole excitations into the trial wave-function [20]. For unitary coupling ($1/p_F a_{3D} \to 0$), it could be shown that higher-order particle-hole channels interfere destructively, thus explaining the remarkable precision of ansatz (3.2) both quantitatively and qualitatively. For example, the ground state estimation within ansatz (3.2) only deviates by about two percent from the exact energy [10, 19] at unitarity for a 3D Fermi polaron. Calculations within the Functional Renormalization Group [27] and fixed-node diffusion Monte Carlo [28] yield similar results, as well as the polaron experiment of Ref. [11].

Inspired by this accuracy, the *Chevy ansatz* was transfered to the molecular state for the specialized case of vanishing hole wave-vectors by Mora et al. [21] and, simultaneously, in a general treatment by Punk et al. [22]. The latter work compared this molecular energy with diagrammatic Monte Carlo results [10] (which are expected to be numerically exact) and found excellent agreement, demonstrating that a wave function dressed by single-particle-hole excitations yields a very good approximation of the true ground state molecular energy. At the same time, it was pointed out that there seems to be a small but systematic discrepancy between the *Chevy ansatz* and the diagrammatic Monte Carlo results of the polaron. Ref. [22] also calculated Tan's contact coefficient, showing that it exhibits a discontinuous jump along the polaron-to-molecule transition; furthermore, the polaron quasiparticle residue could be determined for a broad range of interaction strengths. Interestingly, the residue did not drop to zero in the molecular zero as should be expected since the polaron is no longer the ground state in this region. Concerning the molecular state, also refer to the diagrammatic approaches of Ref. [23] and [10] which preceded the variational formulation of this problem and calculate the quasiparticle effective mass.

In 2010, Mathy et al. revisited the mass-imbalanced Fermi-polaron problem. Mapping the ground state of the system for a large variety of interaction strengths and imbalance ratios, they identified polaronic, molecular, trimer and nonzero-momentum molecular ground states, where a trimer is a bound state of the impurity with two bath atoms. As the nonzero-momentum molecular state was restricted to a narrow region in parameter space, it remained an open question whether the single-particle-hole picture was sufficient to locate this phase unambiguously. Mathy et al. also discussed the effect of phase separation (cf. Ref. [15, 16]).

Further investigations of Zöllner et al. proceeded to the two-dimensional Fermi polaron problem [32]. In contrast to three dimensions, no polaron-to-molecule transition could be found. Parish's subsequent paper [33] showed that the trial wave-functions of Zöllner et al. did not treat the polaron and molecule ansatz on a similar footing. Using the correct wave functions, she was

able to show that the polaron-to-molecule transition persists in two-dimensional setups. Her work readily generalized to mass-imbalanced polaron systems such that the transition could be mapped with respect to the imbalance ratio and the interaction strength.

In 2013, Parish and Levinsen refined the ansatz of Ref. [33] and gave a systematic investigation of different variational ansätze [14] in a pure 2D geometry. Using up to two-particle-hole excitations showed that the pure *Chevy ansatz* is not quantitatively correct, thus explaining the observation of Punk et al. [22]. Parish and Levinsen estimated the ground-state phase diagram in two different approximation levels and found polaronic, molecular, trimer and nonzero-momentum molecular ground states, just as in 3D. They also calculated the quasiparticle residue and effective mass of this pure 2D polaron.

Since this overview was focused on the topics relevant for this thesis, it is by far not complete. Further work based on the *Chevy ansatz* or related diagrammatic techniques includes Ref. [24–26, 59–66].

3.2. Diagrammatic building blocks

In the following, the Fermi-polaron problem is analyzed by using the diagrammatic methods of quantum field theory. First, it is necessary to identify the diagrammatic building blocks.

Green's functions Translating the first part of Eq. (3.1) into a quantum field theory propagator yields [10, 46, 67]

$$G^0_\uparrow(\tau, \boldsymbol{p}) = -\theta(\tau)\theta(p - p_F)e^{-(\epsilon_{p,\uparrow} - E_F)\tau} + \theta(-\tau)\theta(p_F - p)e^{-(\epsilon_{p,\uparrow} - E_F)\tau} \tag{3.3}$$

$$G^0_\downarrow(\tau, \boldsymbol{p}) = -\theta(\tau)e^{-(\epsilon_{p,\downarrow} - \mu^0_\downarrow)\tau}, \tag{3.4}$$

where $\mu^0_\downarrow$ was introduced for tuning purposes of the simulation. Here, both vacuum Green's functions G^0 are expressed as functions of imaginary time τ and momentum $\boldsymbol{p}$ to keep them real and decaying with increasing τ. As the impurity is a single atom, propagation in negative time direction[1] (corresponding to hole-creation with momentum $|\boldsymbol{p}| < p_F$) is excluded for $G^0_\downarrow$.

As it will be necessary to work in frequency space for the derivation of the T matrix, the concrete form of the propagators in ω-$\boldsymbol{p}$ representation is needed:

$$G^0_\uparrow(\omega, \boldsymbol{p}) = \frac{\theta(p - p_F)}{\omega - \epsilon_{p,\uparrow} + E_F + i0} + \frac{\theta(p_F - p)}{\omega - \epsilon_{p,\uparrow} + E_F - i0} \tag{3.5}$$

$$G^0_\downarrow(\omega, \boldsymbol{p}) = \frac{1}{\omega - \epsilon_{p,\downarrow} + \mu^0_\downarrow + i0}, \tag{3.6}$$

where the shifting of the denominator in the complex plane is reflecting the Feynman contour.

Interaction Introducing the interaction is not as straightforward as the basic propagators. The four-point interaction of Eq. (3.1) is conventionally translated [68] into a vertex of strength $g(\boldsymbol{k})$. At low temperatures, the inter-particle interaction can be modeled by a pseudo-potential in case of zero effective range [48, 51]. In this model, $g(\boldsymbol{k}) = g$ is constant and independent of momentum [49].

In principle, this is all that has to be done to write down the full diagrammatic series and calculate all properties of interest. However, it turns out that the series suffers from an ultraviolet divergence which must be cured before we can proceed. This can be achieved by identifying a subclass of all diagrams called ladder diagrams which are defined in Fig. 3.1.

[1] Graphically, we draw positive time from left to right.

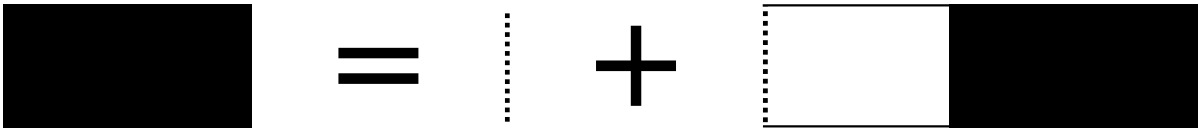

Figure 3.1.: Illustration of the self-consistent T matrix equation. Bare interaction lines are depicted by dotted lines, fermion propagators by horizontal full lines and T matrices by filled rectangles. The impurity propagator line $G^0_\downarrow$ is the lower of the two fermion lines.

Translating this graphical relation according to quantum field theory [68] gives

$$-i\Gamma(\omega,\boldsymbol{p}) = -ig + \int_{q>p_F} \frac{\mathrm{d}\boldsymbol{q}}{(2\pi)^d} \int \frac{\mathrm{d}\omega'}{2\pi} (-ig)\, iG^0_\uparrow(\omega',\boldsymbol{q}) iG^0_\downarrow(\omega-\omega',\boldsymbol{p}-\boldsymbol{q})\, (-i\Gamma(\omega,\boldsymbol{p}))\,, \tag{3.7}$$

where d is the number of dimensions and Γ denotes the full diagrammatic T matrix. In first approximation, Γ replaces an interaction line which means that it has to follow the same sign convention as g. Rewriting this equation as

$$\frac{1}{\Gamma(\omega,\boldsymbol{p})} = \frac{1}{g} - i\int_{q>p_F} \frac{\mathrm{d}\boldsymbol{q}}{(2\pi)^d} \int \frac{\mathrm{d}\omega'}{2\pi} G^0_\uparrow(\omega',\boldsymbol{q}) G^0_\downarrow(\omega-\omega',\boldsymbol{p}-\boldsymbol{q}) \tag{3.8}$$

and using residue calculus for the frequency-integral, one gets

$$\frac{1}{\Gamma(\omega,\boldsymbol{p})} = \frac{1}{g} - \int_{q>p_F} \frac{\mathrm{d}\boldsymbol{q}}{(2\pi)^d} \frac{1}{\omega + E_F + \mu^0_\downarrow - \frac{q^2}{2m_\uparrow} - \frac{(\boldsymbol{p}-\boldsymbol{q})^2}{2m_\downarrow}}. \tag{3.9}$$

In three dimensions, this expression diverges linearly in q, whereas a logarithmic divergence occurs for $d = 2$. That is no problem *per se*: As g does not refer to the physical coupling [69], these infinities can be cured by relating Eq. (3.9) to inherent two-body scattering properties. This procedure exchanges the bare coupling g with the scattering lengths $a_{3\mathrm{D}}$ and $a_{2\mathrm{D}}$. The next sections derive the expressions for Γ in two and three dimensions, as well as the confined three-dimensional case.

3.3. Many-body T matrix in three dimensions

In three dimensions[2], Eq. (3.9) is

$$\frac{1}{\Gamma(\omega,\boldsymbol{p})} = \frac{1}{g} - \int_{q>p_F} \frac{\mathrm{d}\boldsymbol{q}}{(2\pi)^3} \frac{1}{\omega + E_F + \mu^0_\downarrow - \frac{q^2}{2m_\uparrow} - \frac{(\boldsymbol{p}-\boldsymbol{q})^2}{2m_\downarrow}}. \tag{3.10}$$

As we will show in the following, a similar expression appears in the Lippmann-Schwinger equation of quantum scattering and can be used for regularization.

Two-body T matrix It is necessary to step back to a two-particle problem consisting of the impurity interacting with one of the bath particles, as in Eq. (2.2):

$$(\hat{H}_0 + \hat{V})|\psi\rangle = E|\psi\rangle. \tag{3.11}$$

[2]This section is reprinted from Ref. [46] for completeness.

Here, $\hat{H}_0$ was defined to be $\hat{\boldsymbol{p}}^2/2m_r$. If the operator[3] $\frac{1}{E-\hat{H}_0+i0}$ is applied on both sides, this equation can be transformed to Lippmann-Schwinger form

$$|\psi\rangle = \frac{1}{E-\hat{H}_0+i0}\hat{V}|\psi\rangle + |\boldsymbol{k}\rangle. \tag{3.12}$$

The vector $|\boldsymbol{k}\rangle$, an eigenstate of $\hat{H}_0$, has to be introduced by hand to ensure that the correct solution is maintained for $V = 0$. $\boldsymbol{k}$ is the relative momentum of the incoming wave.

Imposing $\hat{V}$ on the left and introducing the two-body T matrix $\hat{T}^{\mathrm{2B}}$ via $\hat{T}^{\mathrm{2B}}|\boldsymbol{k}\rangle \equiv \hat{V}|\psi\rangle$, it follows that

$$\hat{T}^{\mathrm{2B}}|\boldsymbol{k}\rangle = \hat{V}|\boldsymbol{k}\rangle + \hat{V}\frac{1}{E-\hat{H}_0+i0}\hat{T}^{\mathrm{2B}}|\boldsymbol{k}\rangle. \tag{3.13}$$

In the next step, $\langle\boldsymbol{k'}|$ is multiplied from the left with $|\boldsymbol{k'}| = |\boldsymbol{k}|$ and a complete set of eigenfunctions of $\hat{H}_0$ is inserted

$$\langle\boldsymbol{k'}|\hat{T}^{\mathrm{2B}}|\boldsymbol{k}\rangle = \langle\boldsymbol{k'}|\hat{V}|\boldsymbol{k}\rangle + \int\frac{\mathrm{d}\boldsymbol{q}}{(2\pi)^3}\langle\boldsymbol{k'}|\hat{V}|\boldsymbol{q}\rangle\langle\boldsymbol{q}|\frac{1}{E-\hat{H}_0+i0}\hat{T}^{\mathrm{2B}}|\boldsymbol{k}\rangle. \tag{3.14}$$

The matrix elements of the potential are trivial for a pseudo-potential and the newly inserted $|\boldsymbol{q}\rangle$ is an eigenstate of $\hat{H}_0$

$$\langle\boldsymbol{k'}|\hat{T}^{\mathrm{2B}}|\boldsymbol{k}\rangle = g + g\int\frac{\mathrm{d}\boldsymbol{q}}{(2\pi)^3}\frac{1}{E-\frac{q^2}{2m_r}+i0}\langle\boldsymbol{q}|\hat{T}^{\mathrm{2B}}|\boldsymbol{k}\rangle. \tag{3.15}$$

Looking at $\langle\boldsymbol{q}|\hat{T}^{\mathrm{2B}}|\boldsymbol{k}\rangle$ more closely

$$\begin{aligned}\langle\boldsymbol{q}|\hat{T}^{\mathrm{2B}}|\boldsymbol{k}\rangle = \langle\boldsymbol{q}|\hat{V}|\psi\rangle &= \int\frac{\mathrm{d}\boldsymbol{q'}}{(2\pi)^3}\langle\boldsymbol{q}|\hat{V}|\boldsymbol{q'}\rangle\langle\boldsymbol{q'}|\psi\rangle = \int\frac{\mathrm{d}\boldsymbol{q'}}{(2\pi)^3}g\langle\boldsymbol{q'}|\psi\rangle \\ &= \int\frac{\mathrm{d}\boldsymbol{q'}}{(2\pi)^3}\langle\boldsymbol{k'}|\hat{V}|\boldsymbol{q'}\rangle\langle\boldsymbol{q'}|\psi\rangle = \langle\boldsymbol{k'}|\hat{T}^{\mathrm{2B}}|\boldsymbol{k}\rangle.\end{aligned} \tag{3.16}$$

Remarkably, this expression does not depend on the first element. As there is no $\boldsymbol{q}$-dependence left, the T matrix can be extracted from the integral

$$\frac{1}{\langle\boldsymbol{k'}|\hat{T}^{\mathrm{2B}}|\boldsymbol{k}\rangle} = \frac{1}{g} - \int\frac{\mathrm{d}\boldsymbol{q}}{(2\pi)^3}\frac{1}{E-\frac{q^2}{2m_r}}. \tag{3.17}$$

Connecting $\hat{T}^{\mathrm{2B}}$ with Γ The two-body T matrix is related to the scattering length [49] if the effective range can be set to zero

$$\frac{1}{\langle\boldsymbol{k'}|\hat{T}^{\mathrm{2B}}|\boldsymbol{k}\rangle} = \frac{m_r}{2\pi a_{\mathrm{3D}}}(1+ia_{\mathrm{3D}}k). \tag{3.18}$$

k is related to the energy of relative motion (see Chapter 2) and can be generalized to off-shell behavior

$$\frac{k^2}{2m_r} = E = E_{\mathrm{tot}} - E_{\mathrm{com}} = \omega + E_F + \mu_\downarrow^0 - \frac{p^2}{2M}. \tag{3.19}$$

[3]The fraction denotes a formal inverse.

Note that the total energy ω is measured with respect to E_F and $\mu_\downarrow^0$. p is the total momentum of the system. We introduce the abbreviation $\Omega = \omega + E_F + \mu_\downarrow^0$. Inserting the off-shell behavior into Eq. (3.17) yields

$$\frac{1}{g} = \frac{m_r}{2\pi a_{3\mathrm{D}}} - \frac{m_r}{2\pi}\sqrt{\frac{m_r}{M}p^2 - 2m_r\Omega} + \int \frac{\mathrm{d}\boldsymbol{q}}{(2\pi)^3}\frac{1}{\Omega - \frac{p^2}{2M} - \frac{q^2}{2m_r}}. \tag{3.20}$$

Finally, a suitable expression for the T matrix in frequency space can be found by inserting Eq. (3.20) into Eq. (3.10):

$$\begin{aligned}\frac{1}{\Gamma(\omega,\boldsymbol{p})} =& \frac{m_r}{2\pi a_{3\mathrm{D}}} - \frac{m_r}{2\pi}\sqrt{\frac{m_r}{M}p^2 - 2m_r\Omega} + \int \frac{\mathrm{d}\boldsymbol{q}}{(2\pi)^3}\frac{1}{\Omega - \frac{p^2}{2M} - \frac{q^2}{2m_r}} \\ &- \int_{q>p_F} \frac{\mathrm{d}\boldsymbol{q}}{(2\pi)^3}\frac{1}{\Omega - \frac{q^2}{2m_\uparrow} - \frac{(\boldsymbol{p}-\boldsymbol{q})^2}{2m_\downarrow}}.\end{aligned}$$

This can be cast into its final form by a shift $\boldsymbol{q} \to \boldsymbol{q} - \frac{m_\uparrow}{M}\boldsymbol{p}$ in the first integral

$$\Gamma(\omega,\boldsymbol{p})^{-1} = \frac{m_r}{2\pi a_{3\mathrm{D}}} - \frac{m_r}{2\pi}\sqrt{\frac{m_r}{M}p^2 - 2m_r\Omega} + \int_{q<p_F} \frac{\mathrm{d}\boldsymbol{q}}{(2\pi)^3}\frac{1}{\Omega - \frac{q^2}{2m_\uparrow} - \frac{(\boldsymbol{p}-\boldsymbol{q})^2}{2m_\downarrow}}. \tag{3.21}$$

In three dimensions, the T Matrix for unequal masses is known up to a two-dimensional integral; for $\boldsymbol{p} = 0$, the angular integration is trivial and the T Matrix becomes a one-dimensional integral. If the representation in imaginary time is needed, this expression can be analytically continued via $\omega \to i\omega$ to Matsubara frequency space. A subsequent Fourier transform is without complications if a vacuum T matrix

$$\Gamma^0(\omega,\boldsymbol{p})^{-1} = \frac{m_r}{2\pi a_{3\mathrm{D}}} - \frac{m_r}{2\pi}\sqrt{\frac{m_r}{M}p^2 - 2m_r\Omega} \tag{3.22}$$

is subtracted prior to the transform.

3.4. Many-body T matrix in two dimensions

In two dimensions, Eq. (3.9) is

$$\frac{1}{\Gamma(\omega,\boldsymbol{p})} = \frac{1}{g} - \int_{q>p_F} \frac{\mathrm{d}\boldsymbol{q}}{(2\pi)^2}\frac{1}{\Omega - \frac{q^2}{2m_\uparrow} - \frac{(\boldsymbol{p}-\boldsymbol{q})^2}{2m_\downarrow}}. \tag{3.23}$$

Again, a similar expression appears in the standard scattering Lippmann-Schwinger equation and can be used for regularization. The derivation of the two-body T matrix is the same as in 3D:

$$\frac{1}{\langle \boldsymbol{k'}|\hat{T}^{2\mathrm{B}}|\boldsymbol{k}\rangle} = \frac{1}{g} - \int \frac{\mathrm{d}\boldsymbol{q}}{(2\pi)^2}\frac{1}{E - \frac{q^2}{2m_r}}. \tag{3.24}$$

Connecting $\hat{T}^{2\mathrm{B}}$ with the scattering amplitude As the next step, the relation of this two-body T matrix with the asymptotic form of scattering,

$$\psi_{\boldsymbol{k}}(r,\phi) \underset{kr\to\infty}{\longrightarrow} e^{ikx} - \sqrt{\frac{i}{8\pi}}f_k(\phi)\frac{e^{ikr}}{\sqrt{kr}}, \tag{3.25}$$

which was defined in Eq. (2.21), has to be established. Writing Eq. (3.12) in a wave function picture gives

$$\psi_{\boldsymbol{k}}(\boldsymbol{r}) = e^{ikx} + \langle \boldsymbol{r}| \frac{1}{E - \hat{H}_0 + i0} \hat{V}|\psi\rangle. \tag{3.26}$$

Hence, $A \equiv \langle \boldsymbol{r}| \frac{1}{E-\hat{H}_0+i0} \hat{V}|\psi\rangle$ should be investigated further:

$$\begin{aligned} A &= \int \frac{\mathrm{d}\boldsymbol{q}}{(2\pi)^2} \langle \boldsymbol{r}| \frac{1}{E - \hat{H}_0 + i0} |\boldsymbol{q}\rangle \langle \boldsymbol{q}|\hat{V}|\psi\rangle = \\ &= \int \frac{\mathrm{d}\boldsymbol{q}}{(2\pi)^2} \langle \boldsymbol{r}| \frac{1}{E - \frac{q^2}{2m_r} + i0} |\boldsymbol{q}\rangle \langle \boldsymbol{q}|\hat{V}|\psi\rangle = 2m_r \int \frac{\mathrm{d}\boldsymbol{q}}{(2\pi)^2} \frac{e^{i\boldsymbol{q}\boldsymbol{r}}}{k^2 - q^2 + i0} \langle \boldsymbol{q}|\hat{V}|\psi\rangle. \end{aligned} \tag{3.27}$$

Remember that the operator $\hat{H}_0$ is diagonal in momentum space and that $E = \frac{k^2}{2m_r}$. After inserting a position basis, the q-integral gives the modified Bessel function of the second kind, K_0 (up to a factor) [70]:

$$\begin{aligned} A &= 2m_r \int \mathrm{d}\boldsymbol{r'} \int \frac{\mathrm{d}\boldsymbol{q}}{(2\pi)^2} \frac{e^{i\boldsymbol{q}\boldsymbol{r}}}{k^2 - q^2 + i0} \langle \boldsymbol{q}|\boldsymbol{r'}\rangle \langle \boldsymbol{r'}|\hat{V}|\psi\rangle \\ &= 2m_r \int \mathrm{d}\boldsymbol{r'} \int \frac{\mathrm{d}\boldsymbol{q}}{(2\pi)^2} \frac{e^{i\boldsymbol{q}(\boldsymbol{r}-\boldsymbol{r'})}}{k^2 - q^2 + i0} \langle \boldsymbol{r'}|\hat{V}|\psi\rangle \\ &= -\frac{m_r}{\pi} \int \mathrm{d}\boldsymbol{r'} K_0\left(-ik\,|\boldsymbol{r} - \boldsymbol{r'}|\right) \langle \boldsymbol{r'}|\hat{V}|\psi\rangle. \end{aligned} \tag{3.28}$$

Another position basis has to be inserted to study the argument of K_0 further:

$$\begin{aligned} A &= -\frac{m_r}{\pi} \int \mathrm{d}\boldsymbol{r'} \int \mathrm{d}\boldsymbol{r''} K_0\left(-ik\,|\boldsymbol{r} - \boldsymbol{r'}|\right) \langle \boldsymbol{r'}|\hat{V}|\boldsymbol{r''}\rangle \langle \boldsymbol{r''}|\psi\rangle \\ &= -\frac{m_r}{\pi} \int \mathrm{d}\boldsymbol{r'} K_0\left(-ik\,|\boldsymbol{r} - \boldsymbol{r'}|\right) V(\boldsymbol{r'})\psi(\boldsymbol{r'}). \end{aligned} \tag{3.29}$$

For rapidly decaying scattering potentials, this means that only the $\boldsymbol{r'}$ that are close to the origin contribute to the integral. Consequently, $|\boldsymbol{r}| \gg |\boldsymbol{r'}|$ so that the asymptotic behavior of the modified Bessel function for $kr \to \infty$ can be used in Eq. (3.28):

$$A \approx -\frac{m_r}{\pi} \int \mathrm{d}\boldsymbol{r'} \sqrt{\frac{\pi}{2}} \frac{e^{ik|\boldsymbol{r}-\boldsymbol{r'}|}}{\sqrt{-ik\,|\boldsymbol{r} - \boldsymbol{r'}|}} \langle \boldsymbol{r'}|\hat{V}|\psi\rangle. \tag{3.30}$$

The absolute value can be simplified by the approximation

$$|\boldsymbol{r} - \boldsymbol{r'}| = \sqrt{r^2 + r'^2 - 2\boldsymbol{r}\boldsymbol{r'}} \approx \sqrt{r^2 - 2\boldsymbol{r}\boldsymbol{r'}} = r\sqrt{1 - 2\frac{\boldsymbol{r}\boldsymbol{r'}}{r^2}} \approx r\left(1 - \frac{\boldsymbol{r}\boldsymbol{r'}}{r^2}\right). \tag{3.31}$$

This means that

$$A \approx -\frac{m_r}{\pi} \int \mathrm{d}\boldsymbol{r'} \sqrt{\frac{\pi}{2}} \frac{e^{ik(r - \frac{\boldsymbol{r}}{r}\boldsymbol{r'})}}{\sqrt{-ik(r - \frac{\boldsymbol{r}}{r}\boldsymbol{r'})}} \langle \boldsymbol{r'}|\hat{V}|\psi\rangle \approx -m_r \sqrt{\frac{1}{2\pi}} \int \mathrm{d}\boldsymbol{r'} \frac{e^{ik(r - \frac{\boldsymbol{r}}{r}\boldsymbol{r'})}}{\sqrt{-ikr}} \langle \boldsymbol{r'}|\hat{V}|\psi\rangle. \tag{3.32}$$

Defining $\boldsymbol{k'} = k\frac{\boldsymbol{r}}{r}$, the connection with the scattering amplitude is established:

$$A = -m_r \sqrt{\frac{1}{2\pi}} \sqrt{\frac{i}{kr}} e^{ikr} \langle \boldsymbol{k'}|\hat{V}|\psi\rangle = -\sqrt{\frac{i}{8\pi}} \left(2m_r \langle \boldsymbol{k'}|\hat{V}|\psi\rangle\right) \frac{e^{ikr}}{\sqrt{kr}}. \tag{3.33}$$

Since $\langle \boldsymbol{k'}|\hat{V}|\psi\rangle = \langle \boldsymbol{k'}|\hat{T}^{2\mathrm{B}}|\boldsymbol{k}\rangle$, a comparison with Eq. (3.25) gives $f_k(\phi) = 2m_r\langle \boldsymbol{k'}|\hat{T}^{2\mathrm{B}}|\boldsymbol{k}\rangle$. Using the results of the scattering amplitude presented in Eq. (2.26), the Lippmann-Schwinger T matrix is

$$\langle \boldsymbol{k'}|\hat{T}^{2\mathrm{B}}|\boldsymbol{k}\rangle = \frac{2\pi/m_r}{-2\ln(ka_{2\mathrm{D}}) + i\pi}. \tag{3.34}$$

Diagrammatic vacuum T matrix Going back to Eq. (3.24) and generalizing it to off-shell behavior $E = \frac{k^2}{2m_r} = \Omega - \frac{p^2}{2M}$ yields

$$\frac{1}{\langle \boldsymbol{k'}|\hat{T}^{2\mathrm{B}}|\boldsymbol{k}\rangle} = \frac{1}{g} - \int \frac{\mathrm{d}\boldsymbol{q}}{(2\pi)^2} \frac{1}{\Omega - \frac{p^2}{2M} - \frac{q^2}{2m_r}}. \tag{3.35}$$

Now, a shift of integration variables $\boldsymbol{q} \to \boldsymbol{q} - \frac{\boldsymbol{p}m_\uparrow}{M}$ transforms the integral to

$$\frac{1}{\langle \boldsymbol{k'}|\hat{T}^{2\mathrm{B}}|\boldsymbol{k}\rangle} = \frac{1}{g} - \int \frac{\mathrm{d}\boldsymbol{q}}{(2\pi)^2} \frac{1}{\Omega - \frac{q^2}{2m_\uparrow} - \frac{(\boldsymbol{p}-\boldsymbol{q})^2}{2m_\downarrow}}. \tag{3.36}$$

This has to be compared with Eq. (3.23),

$$\frac{1}{\Gamma(\omega,\boldsymbol{p})} = \frac{1}{g} - \int_{q>p_F} \frac{\mathrm{d}\boldsymbol{q}}{(2\pi)^2} \frac{1}{\Omega - \frac{q^2}{2m_\uparrow} - \frac{(\boldsymbol{p}-\boldsymbol{q})^2}{2m_\downarrow}}. \tag{3.37}$$

In vacuum, the Fermi momentum is zero, thus the integrals are exactly the same. This invites the definition of the vacuum T matrix as

$$\Gamma^0(\omega,\boldsymbol{p}) \equiv \langle \boldsymbol{k'}|\hat{T}^{2\mathrm{B}}|\boldsymbol{k}\rangle = \frac{2\pi/m_r}{-2\ln\left(\sqrt{2m_r}a_{2\mathrm{D}}\sqrt{\Omega - \frac{p^2}{2M}}\right) + i\pi}. \tag{3.38}$$

The remaining task is to find Γ.

Diagrammatic T Matrix Using the definition of the vacuum T matrix in Eq. (3.37) yields

$$\frac{1}{\Gamma(\omega,\boldsymbol{p})} = \frac{1}{\Gamma^0(\omega,\boldsymbol{p})} + \int_{q<p_F} \frac{\mathrm{d}\boldsymbol{q}}{(2\pi)^2} \frac{1}{\Omega - \frac{q^2}{2m_\uparrow} - \frac{(\boldsymbol{p}-\boldsymbol{q})^2}{2m_\downarrow}} \equiv \frac{1}{\Gamma^0(\omega,\boldsymbol{p})} + I(\omega,\boldsymbol{p}). \tag{3.39}$$

As the evaluation of this so-called polarization integral is rather long, it will be presented separately in the next paragraph. Introducing $z = \Omega - \frac{p_F^2}{2m_r} - \frac{p^2}{2m_\downarrow} + \frac{p^2 m_r}{m_\downarrow^2}$, $s = \mathrm{sgn}(\Re[\omega] + E_F + \mu_\downarrow^0 - \frac{p_F^2}{2m_r} - \frac{p^2}{2m_\downarrow})$ and $E_B = 1/2m_r a^2$, the final expression of Γ is

$$\begin{aligned}\frac{1}{\Gamma(\omega,\boldsymbol{p})} &= \frac{m_r}{2\pi}\left[\ln\left(\frac{E_B}{\Omega - \frac{p^2}{2M}}\right) + i\pi + \ln\left(\frac{2\left(\Omega - \frac{p^2}{2M}\right)}{z + s\sqrt{\left(z - \frac{p^2 m_r}{m_\downarrow^2}\right)^2 - \frac{p_F^2 p^2}{m_\downarrow^2}}}\right)\right] \\ &= \frac{m_r}{2\pi}\left[\ln\frac{E_B}{\frac{z}{2} + \frac{s}{2}\sqrt{\left(z - \frac{p^2 m_r}{m_\downarrow^2}\right)^2 - \frac{p_F^2 p^2}{m_\downarrow^2}}} + i\pi\right].\end{aligned} \tag{3.40}$$

The analytic continuation of this expression to Matsubara frequencies is straightforward, whereas the Fourier transform of the resulting expression from $i\omega$ to τ-space is not defined because it is decaying as $1/\ln\omega$ for $\omega \to \infty$. The two-dimensional T Matrix is important to estimate the degree of confinement in quasi-2D geometries.

Polarization integral The last missing step is the evaluation of the polarization integral – both integrations are analytic:

$$\begin{aligned} I(\omega, \boldsymbol{p}) &= \int_{q<p_F} \frac{\mathrm{d}\boldsymbol{q}}{(2\pi)^2} \frac{1}{\Omega - \frac{q^2}{2m_\uparrow} - \frac{(\boldsymbol{p}-\boldsymbol{q})^2}{2m_\downarrow}} = \int_0^{p_F} \frac{\mathrm{d}q}{2\pi} q \int_{-\pi}^{\pi} \frac{\mathrm{d}\phi}{2\pi} \frac{1}{\Omega - \frac{q^2}{2m_r} - \frac{p^2}{2m_\downarrow} + \frac{qp\cos(\phi)}{m_\downarrow}} \\ &= \int_0^{p_F} \frac{\mathrm{d}q}{2\pi} q \frac{\operatorname{sgn}\left(\Re[\omega] + E_F + \mu_\downarrow^0 - \frac{q^2}{2m_r} - \frac{p^2}{2m_\downarrow}\right)}{\sqrt{\left(\Omega - \frac{q^2}{2m_r} - \frac{p^2}{2m_\downarrow}\right)^2 - \frac{q^2p^2}{m_\downarrow^2}}} \\ &= \left[\frac{m_r}{2\pi} \ln\left(\frac{m_\downarrow^2}{p^2 m_r}\left[B + \frac{p^2 m_r}{m_\downarrow^2} - \operatorname{sgn}\left(\Re[B]\right)\sqrt{B^2 - \frac{q^2p^2}{m_\downarrow^2}}\right]\right)\right]_0^{p_F}. \end{aligned} \tag{3.41}$$

Here, we abbreviated $B = \Omega - \frac{q^2}{2m_r} - \frac{p^2}{2m_\downarrow}$ and used the identity $c = \sqrt{c^2}\,\operatorname{sgn}\left(\Re[c]\right)$. In principle, it might happen that the argument of sgn changes sign for some intermediate value of q. To avoid this problem, suppose that $\mu_\downarrow^0$ is sufficiently large so that this does not happen – remember that $\mu_\downarrow^0$ is an arbitrary tuning parameter. At this point, we introduce $s = \operatorname{sgn}\left(\Re[\omega] + E_F + \mu_\downarrow^0 - \frac{p_F^2}{2m_r} - \frac{p^2}{2m_\downarrow}\right)$. Defining $z = \Omega - \frac{p_F^2}{2m_r} - \frac{p^2}{2m_\downarrow} + \frac{p^2 m_r}{m_\downarrow^2}$ and noting that the lower bound is zero, the polarization becomes

$$\begin{aligned} I(\omega, \boldsymbol{p}) &= \frac{m_r}{2\pi} \ln\left(\frac{m_\downarrow^2}{p^2 m_r}\left[z - s\sqrt{\left(z - \frac{p^2 m_r}{m_\downarrow^2}\right)^2 - \frac{p_F^2 p^2}{m_\downarrow^2}}\right]\right) = \\ &= \frac{m_r}{2\pi} \ln\left(\frac{m_\downarrow^2}{p^2 m_r} \frac{z^2 - \left(z - \frac{p^2 m_r}{m_\downarrow^2}\right)^2 + \frac{p_F^2 p^2}{m_\downarrow^2}}{z + s\sqrt{\left(z - \frac{p^2 m_r}{m_\downarrow^2}\right)^2 - \frac{p_F^2 p^2}{m_\downarrow^2}}}\right) = \frac{m_r}{2\pi} \ln\left(\frac{2(\Omega - \frac{p^2}{2M})}{z + s\sqrt{\left(z - \frac{p^2 m_r}{m_\downarrow^2}\right)^2 - \frac{p_F^2 p^2}{m_\downarrow^2}}}\right). \end{aligned} \tag{3.42}$$

This result can be shifted to imaginary frequencies by analytic continuation in a straightforward way.

3.5. Many-body T matrix in three dimensions with harmonic confinement

In a realistic experiment, the 2D limit will be approached by tightly confining the three-dimensional gas strongly along the z axis by applying a laser with trapping frequency ω_z, thereby creating a tight harmonic oscillator in the z direction. We model this experimental setup by formally working in three dimensions but choosing ω_z high enough such that only the lowest harmonic oscillator state is populated.

Quasi-two-dimensional geometries are similar to pure 2D ones in the sense that an analytic expression exists for the low energy behavior of the vacuum T matrix, which then can be linked

with the full T matrix by a self-consistent equation.

Vacuum T matrix The low energy expression of the vacuum T matrix is derived in Refs. [64] and [71] and reads

$$\Gamma^0(i\omega, \boldsymbol{p}) = \frac{\frac{4\pi}{m}}{\frac{\sqrt{2\pi}l_z}{a_{3\mathrm{D}}} - \ln\left(-\frac{\pi E}{B\omega_z}\right) + \ln(2)\frac{E}{\omega_z}}, \tag{3.43}$$

where $E = i\omega + E_F + \mu_\downarrow^0 - \frac{p^2}{2M}$, $B \approx 0.905$, and $l_z = \sqrt{\frac{1}{m\omega_z}}$. Note that this expression was already extended to imaginary frequencies. The relationship between the two-dimensional scattering length and its three-dimensional correspondent is [48, 53, 64]

$$a_{2\mathrm{D}} = l_z\sqrt{\frac{\pi}{B}}\exp\left(-\sqrt{\frac{\pi}{2}}\frac{l_z}{a_{3\mathrm{D}}}\right). \tag{3.44}$$

The two-body binding energy E_B must be adjusted to reflect the quasi-two-dimensional nature of our model. As shown in Ref. [64], it is the solution of the following equation

$$\frac{l_z}{a_{3\mathrm{D}}} = \mathcal{F}\left(\frac{E_B}{\omega_z}\right), \tag{3.45}$$

where $\mathcal{F}$ is given by

$$\mathcal{F}(x) = \int_0^\infty \frac{\mathrm{d}u}{\sqrt{4\pi u^3}}\left(1 - \frac{\exp(-xu)}{\sqrt{[1-\exp(-2u)]/2u}}\right). \tag{3.46}$$

Full T matrix The vacuum T matrix can be linked with the full T matrix by [66]

$$\frac{1}{\Gamma(i\omega, \boldsymbol{p})} = \frac{1}{\Gamma^0(i\omega, \boldsymbol{p})} + \int_{q<p_F}\frac{\mathrm{d}\boldsymbol{q}}{(2\pi)^2}\frac{1}{i\omega + E_F + \mu_\downarrow^0 - \frac{q^2}{2m_\uparrow} - \frac{(\boldsymbol{p}-\boldsymbol{q})^2}{2m_\downarrow}}. \tag{3.47}$$

This is the natural strong confinement expansion of Eq. (10) of Ref. [71]. Again, we performed analytic continuation in ω. The polarization integral is the same as in the pure-2D case.

Eq. (3.47) is readily transformed to imaginary times as its high frequency behavior is as $1/\omega$ for $\omega \to \infty$ (although it is necessary to subtract this tail with appropriate coefficients). We would like to emphasize that the quasi-2D T Matrix and the pure-2D T Matrix have to agree for $\omega_z \to \infty$. This was used to test the numerical results.

3.6. Diagrammatic representation of polarons

After establishing the various representations of the T matrix, we are in a position to set up several diagrammatic series for the full Green's function $G_\downarrow(\tau, \boldsymbol{p})$, the quantity that gives us access to the static one-particle properties of our system [68]. Fig. 3.2/I shows the first diagrams contributing to $G_\downarrow$ if no T matrix is used. These are essentially the standard many-body diagrams of a four-point interaction [68] where three types of diagrams are disregarded:

1. Diagrams with interaction lines between atoms of the same species, e.g., $\uparrow$ and $\uparrow$.
2. Diagrams with impurity lines that are disconnected from the backbone impurity line.
3. Diagrams with noninstantaneous interaction lines.

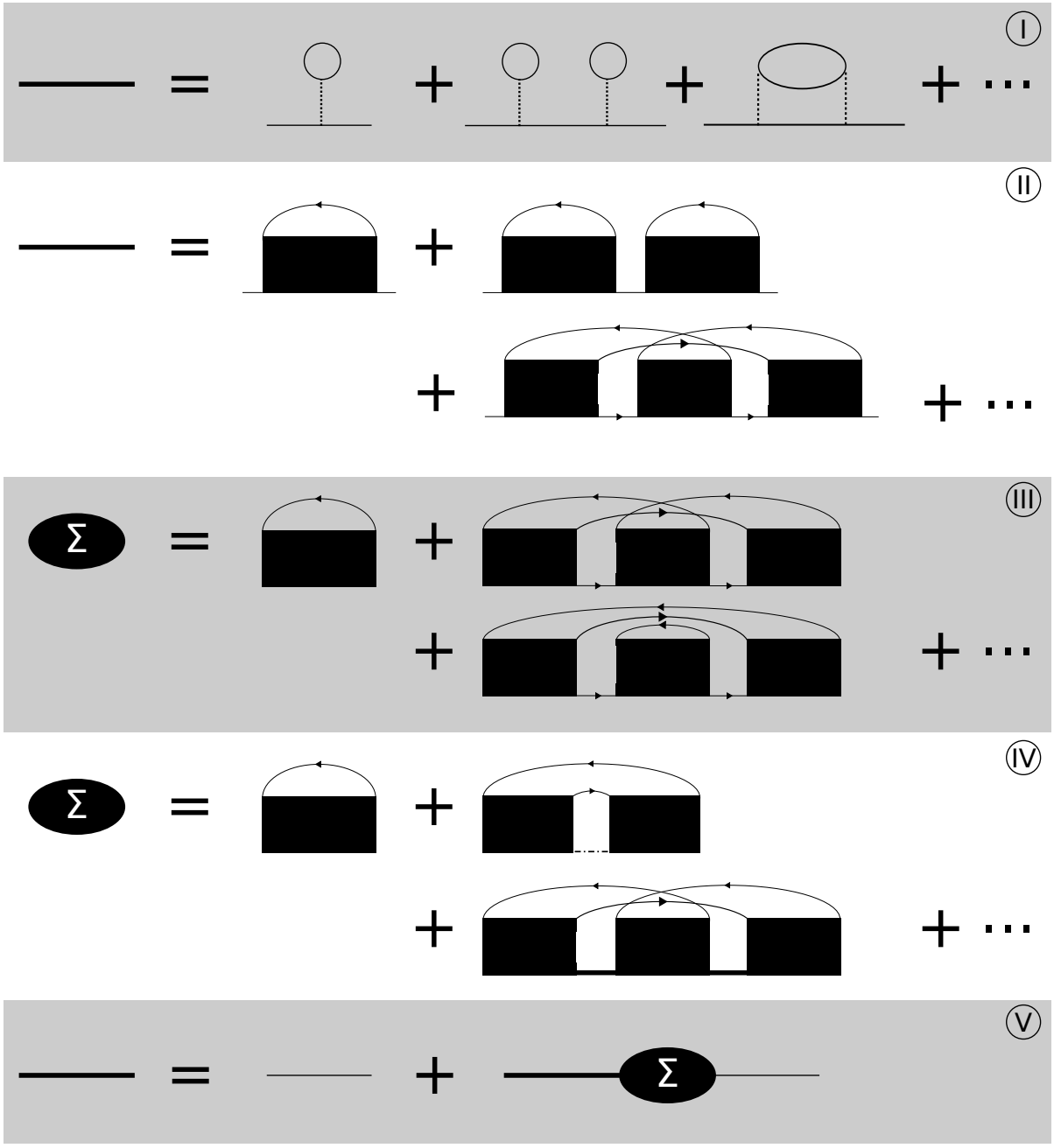

Figure 3.2.: Illustration of five diagrammatic relations of the Fermi polaron. Bare interaction lines are depicted by dotted lines, fermion propagators by horizontal full lines and T matrices by filled rectangles. The impurity propagator line $G^0_\downarrow$ is the lowest of the fermion lines. The full Green's function is given by a bold line, the self-energy is labeled by Σ and the dashed-dotted line stands for $G_\downarrow - G^0_\downarrow$.

Fig. 3.2/II shows the rewriting of this series in terms of T matrices. It is important to note that adjacent T matrices may not be linked since this would result in a double-counting of diagrams. In this representation, all terms in the series of $G_\downarrow$ are finite. In many cases, it is beneficial to go one step further and identify the main diagrammatic building blocks by means of Dyson's equation [68]

$$G_\downarrow(\omega, \boldsymbol{p}) = G^0_\downarrow(\omega, \boldsymbol{p}) + G_\downarrow(\omega, \boldsymbol{p})\Sigma(\omega, \boldsymbol{p})G^0_\downarrow(\omega, \boldsymbol{p}), \tag{3.48}$$

where the self-energy Σ was introduced. Dyson's equation is shown in Fig. 3.2/V. If $\Sigma(\tau, \boldsymbol{p})$ is known, a Fourier transform gives $\Sigma(i\omega, \boldsymbol{p})$, which can be used to solve Dyson's equation for $G_\downarrow(i\omega, \boldsymbol{p})$. This means that we can restrict ourselves to finding Σ. A diagrammatic representation of the self-energy is given in Fig. 3.2/III. All diagrams up to third order are shown. We define the order of a polaron diagram by the number of T matrices.

As a last representation, Fig. 3.2/IV shows another series for the self-energy. The crucial difference with the former series is that Σ is defined in terms of full Green's functions which introduces self-consistency via Dyson's equation. Note the special diagrammatic weight $G_\downarrow - G^0_\downarrow$ on impurity propagators linking neighboring T matrices which ensures that no double counting occurs. For further information on this series, consult Ref. [10].

3.7. Diagrammatic representation of molecules

This chapter is concluded by introducing the series for molecular states. The quantity corresponding to the full Green's function of a polaron is the two-particle Green's function K [10, 72], which is diagrammatically expanded in a way that is very similar to the one-particle Green's function G. In Fig. 3.3/I, some diagrams of low order are shown. Inspired by the structure of these diagrams, a classification of diagrams on basis of the number of uncovered T matrices comes to mind. Fig. 3.3/II defines a quantity K^0 as the sum of all diagrams that do not recombine into a T matrix. With this, a rewriting

$$K = K^0 + K^0\ \Gamma\ K^0 + K^0\ \Gamma\ \tilde{K}\ \Gamma\ K^0 + K^0\ \Gamma\ \tilde{K}\ \Gamma\ \tilde{K}\ \Gamma\ K^0 + \dots \tag{3.49}$$

is possible, as shown in Fig. 3.3/III. Note that the splitting of K^0 into a first-order contribution and a quantity that is denoted $\tilde{K}$ is necessary to exclude the direct linking of T matrices which would result in double counting (Fig. 3.3/IV). Now it is possible to extract an expression for the pair propagator that is similar to Dyson's equation (Fig. 3.3/V and Fig. 3.3/VI), where a quantity Q is introduced as

$$Q = \Gamma + \Gamma\ \tilde{K}\ \Gamma + \Gamma\ \tilde{K}\ \Gamma\ \tilde{K}\ \Gamma + \dots = \Gamma + \Gamma\ \tilde{K}\ Q. \tag{3.50}$$

$\tilde{K}$ has properties that are very similar to the full pair propagator [10]. This makes it possible to restrict ourselves to this series instead of K which reduces the diagrammatic space considerably. We define the order of a molecule diagram by the number of impurity propagators. For illustration, some diagrammatic contributions to $\tilde{K}$ are shown in Fig. 3.4.

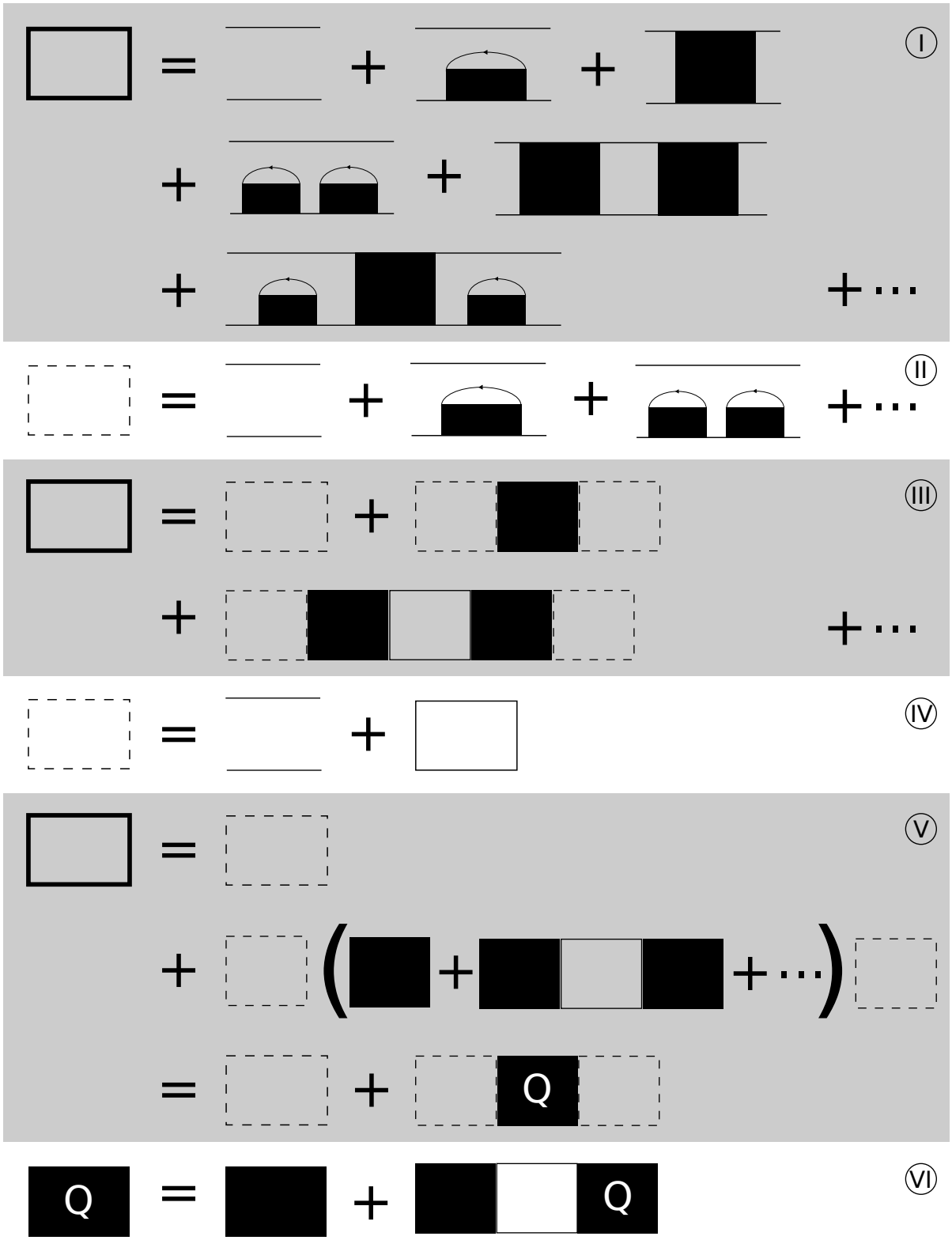

Figure 3.3.: Illustration of diagrammatic relations for the molecular series. The full molecular pair propagator K is symbolized by rectangles with bold borders, K^0 by rectangles with dashed borders and $\tilde{K}$ by rectangles with single (bare) borders.

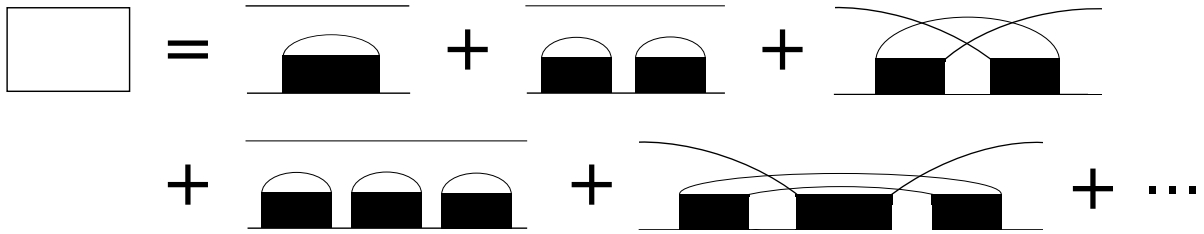

Figure 3.4.: Illustration of the first contributions to $\tilde{K}$.

4 Diagrammatic Monte Carlo

The diagrammatic Monte Carlo method (diagMC) is based on a sampling of high-dimensional Feynman diagram integrals allowing extrapolation to infinite expansion order if the sign problem is not too severe. It can stochastically evaluate the integrals and the different topologies occurring in higher-order perturbation theory and thus provide access to the full Green's function of the system. DiagMC aims at finding a simple set of updates that ensures linking of distinct diagrams in an ergodic way. Generally, the technique is applied to expressions of the form [73]

$$Q\left(\{y\}\right) = \sum_{m=0}^{\infty} \sum_{\xi_m} \int \mathrm{d}x_1 \ldots \mathrm{d}x_m \mathcal{D}_M\left(\xi_m, \{y\}, x_1, \ldots, x_m\right), \tag{4.1}$$

where $\{y\}$ labels a set of external variables and ξ_m distinguishes different terms of the same order. The zeroth order term is seen as a function of the external parameters. Each internal variable can be either continuous or discrete, where the integrations are understood as summations in the discrete case. Note that Eq. (4.1) does not necessarily refer to diagrams and is thus much more general. Standard Monte Carlo sampling is applied to individual terms of this expression, updating internal and external variables. The essential part of diagrammatic Monte Carlo consists of special updates that link orders by a seeding of new variables [73].

DiagMC was introduced by Prokof'ev and Svistunov for the Fröhlich polaron problem [74], a model that approximates the properties of an electron interacting with lattice phonons of a crystal. Since phonons are bosonic, the Dyson series is sign-positive for the Fröhlich Hamiltonian, i.e., the sign problem [7] is no issue and the diagrammatic series could be evaluated up to a maximum expansion order that was sufficiently high to give an answer that was in good agreement with Feynman's path-integral approach. In a subsequent paper [73], several techniques that enhance the diagrammatic sampling were presented, including additional updates, improved estimators and a cyclical representation of diagrams. The latter is a crucial step towards the sampling of two-point and four-point correlation functions in the same simulation.

As a further extension, Ref. [75] made the sampling self-consistent by solving the T matrix equation

$$\begin{aligned}\Gamma\left(\tau, \boldsymbol{p}\right) = \Gamma^0\left(\tau, \boldsymbol{p}\right) \\ + \int_0^\tau \mathrm{d}s \int_s^\tau \mathrm{d}s' \, \Gamma\left(s, \boldsymbol{p}\right) \, \Gamma\left(\tau - s', \boldsymbol{p}\right) \int_{q<p_F} \frac{\mathrm{d}\boldsymbol{q}}{(2\pi)^3} G^0_\downarrow\left(s' - s, \boldsymbol{p} - \boldsymbol{q}\right) G^0_\uparrow\left(s' - s, \boldsymbol{q}\right)\end{aligned} \tag{4.2}$$

by a technique called bold diagrammatic Monte Carlo. In this algorithm, an initial guess for the unknown Γ is used in a first iteration on the right hand side of the equation. After performing a sufficient number of updates, the result is plugged in as a new estimation of Γ. The procedure is repeated until convergence. The solution of the T matrix equation can be used to tabulate the 3D T matrix in imaginary time and momentum which gives accurate access to Γ with some appropriate interpolation. With this input, Prokof'ev and Svistunov advanced on to Dyson

series with alternating sign and solved the Fermi-polaron problem in 3D with balanced masses of impurity and bath atoms [9, 10]. This works if sufficiently high expansion orders can be evaluated before the sign problem makes it unfeasible to proceed in the expansion. A crucial ingredient for the successful application of diagMC to the Fermi-polaron problem was the reduction of diagrammatic space by means of self-energy sampling, allowing to extract energies and effective masses in very good agreement with other techniques.

After this first application of diagMC to a fermionic problem, several authors utilized the technique in typical many-body contexts such as the Hubbard model in the Fermi-liquid regime [76], Anderson localization [77], the unitary Fermi gas [78], and frustrated-spin systems [79, 80]. For the unitary Fermi gas and the three-dimensional Fermi-polaron problem it was found that the full many-body answer is very close to the first-order result given by a hole line on top of a T matrix. For the problem of Anderson localization, it was found that the dynamical mean-field approach (exploiting the locality of the self-energy) was an excellent starting point. In all successful studies performed thus far, an underlying analytical understanding of the main physics allowed for an initial resummation which contained the dominant contributions, whereas the remaining fluctuations were rather small. One would hence expect that the success of diagMC for the Fermi-polaron can also be understood by identifying a (possibly emergent) small parameter. It remains an open question if the method can be successful when there are competing instabilities such as in the repulsive Hubbard model for low doping.

In this chapter, we specify update rules for the Fermi-polaron problem in Sec. 4.1, before the Monte Carlo observables are shown in Sec. 4.2. Next, the algorithmic differences of a partially bold code are stressed in Sec. 4.3. Last, the main data analysis tools of diagMC are discussed, resummation (Sec. 4.4) and extrapolation (Sec. 4.5).

4.1. Update structure

The set of updates we use is different from the approach of Prokof'ev-Svistunov [10]. The latter framework introduces a large quantity of auxiliary diagrams (denoted worm diagrams) which are used for the transition between adjacent diagram orders. We prefer to implement these transitions by direct updates. Furthermore, our approach does not use the cyclical representation so that separate codes are necessary for the sampling of polaron and molecule series. Our set of updates is given by the following pairs:

- *First-to-fake* and *Fake-to-first*,
- *Change-fake* (self-inverse),
- *Insert-mushroom* and *Remove-mushroom*,
- *Insert-Γ* and *Remove-Γ*,
- *Reconnect* (self-inverse).

A *fake diagram* is used for normalization purposes and is graphically identical to the first-order diagram (shown in the left panel of Fig. 4.1), but with analytically easy weights. Its internal variables are updated by the update *Change-fake*. The updates *First-to-fake* and *Fake-to-first* connect this *fake diagram* with the lowest-order diagram we sample, presented in the right panel of Fig. 4.1. Note that this diagram is unphysical if no self-consistent bold scheme [10] is used. The first-order diagram is not included in our simulation because it forces the program to spend a lot of time on small times because of the diverging behavior of Γ for $\tau \to 0$ regardless of dimension. It is straightforward to include the first-order self-energy by a numerical tabulation in ω space [19, 66].

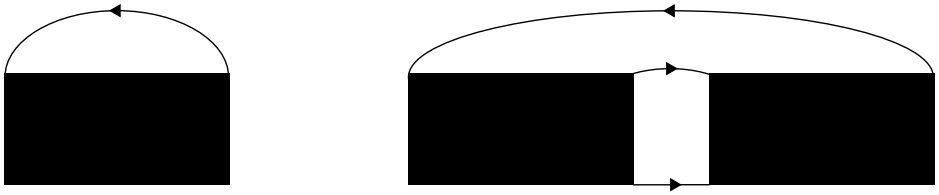

Figure 4.1.: *Left:* The first-order diagram is used for normalization purposes. The (local) appearance of this diagram topology as part of the whole diagram will be used to identify reducible diagrams in partially bold diagMC in Sec. 4.3. *Right:* This (unphysical) second-order diagram connects the first-order *fake diagram* with higher-order diagrams.

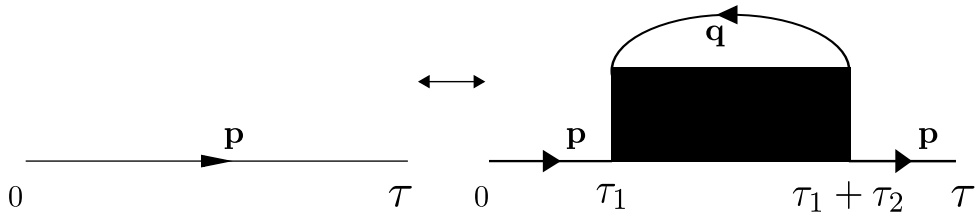

Figure 4.2.: Illustration of inverse updates *Insert-mushroom* and *Remove-mushroom*.

There are four updates linking different orders: *Insert-mushroom*, *Insert-Γ* and their inverse updates *Remove-mushroom* and *Remove-Γ*. *Insert-Γ* chooses any T matrix of the current diagram and splits it into two linked T matrices. The resulting (unphysical) diagram has good overlap with the previous configuration if $G^1_\downarrow - G^0_\downarrow$ is artificially attributed as weight of the underlying impurity propagator. Here, $G^1_\downarrow$ denotes the impurity Green's function evaluated by plugging the first-order self-energy contribution into Dyson's equation.

Last, an update called *Reconnect* ensures that all different topologies of a certain order are sampled.

This set of updates is ergodic and avoids sampling of first-order contributions. The last remaining unphysical diagrams connect two adjacent T matrices – however, this is important for partially bold sampling (cf. Sec. 4.3). If no self-consistent bold scheme is used, sampling of relevant diagrams can be enforced by assigning an additional penalty weight to those diagrams. In the following, we will present the updates *Insert-mushroom*, *Remove-mushroom* and *Reconnect*. The other updates were designed in the same spirit.

Insert-mushroom This update is available for impurity propagator lines. It attempts to insert the diagrammatic structure of the left panel of Fig. 4.1 (called mushroom) on one of these lines. If the current diagram order is denoted by N, there are $N-1$ propagators available for insertion. Having selected one of those with imaginary time τ and momentum $\boldsymbol{p}$, internal time slices τ_1 and τ_2 are uniformly seeded (probabilities: $\mathrm{d}\tau_1/\tau$ and $\mathrm{d}\tau_2/(\tau-\tau_1)$), as well as a bath propagator momentum $\boldsymbol{q}$ with $|\boldsymbol{q}| < p_F$ (probability: $\mathrm{d}\boldsymbol{q}/(2p_F)^d$). This fixes the time variable of the last piece to $\tau_3 = \tau - \tau_1 - \tau_2$. The whole process is illustrated in Fig. 4.2. The Metropolis acceptance ratio P_{IM} is

$$\min\left(1, \frac{p_{\mathrm{RM}}}{p_{\mathrm{IM}}} \frac{G^0_\downarrow(\tau_1,\boldsymbol{p})\Gamma(\tau_2,\boldsymbol{p}+\boldsymbol{q})G^0_\downarrow(\tau_3,\boldsymbol{p})G^0_\uparrow(\tau_2,\boldsymbol{q})}{(2\pi)^d G^0_\downarrow(\tau,\boldsymbol{p}) \cdot \frac{1}{\tau}\frac{1}{\tau-\tau_1}\frac{1}{(2p_F)^d}}\right). \tag{4.3}$$

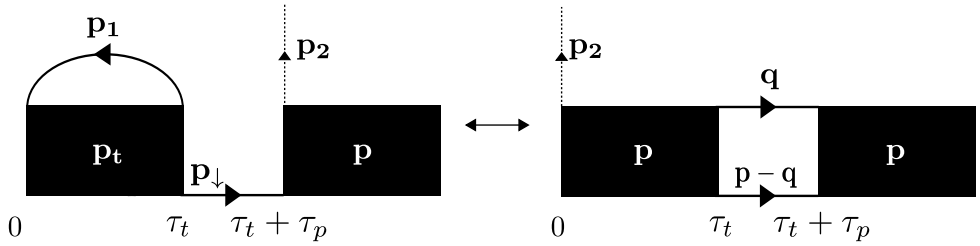

Figure 4.3.: Illustration of the first and second case of update *Reconnect*. The dotted vertical bath propagator line is connected to an arbitrary T matrix in the diagram.

The factor $(2\pi)^d$ in the denominator is part of the diagrammatic weight of the new configuration. p_{IM} and p_{RM} are the probabilities of selecting the updates *Insert-mushroom* or *Remove-mushroom*, respectively.

Remove-mushroom *Remove-mushroom* is the inverse update for *Insert-mushroom*. If the current diagram order is denoted by N, there are N T matrices which could be removed together with the corresponding impurity propagator. However, the first T matrix can not be removed, because it is never constructed by Insert-Mushroom. The same is true for the last T matrix. That leaves $N-2$ possible T matrices and balances the selection factors in the Metropolis algorithm. Being the inverse update of Insert-Mushroom, the acceptance ratio of Remove-Mushroom is given by

$$\min\left(1, \frac{p_{\mathrm{IM}}}{p_{\mathrm{RM}}} \frac{(2\pi)^d G^0_\downarrow(\tau, \boldsymbol{p}) \cdot \frac{1}{\tau} \frac{1}{\tau - \tau_1} \frac{1}{(2p_F)^d}}{G^0_\downarrow(\tau_1, \boldsymbol{p}) \Gamma(\tau_2, \boldsymbol{p}+\boldsymbol{q}) G^0_\downarrow(\tau_3, \boldsymbol{p}) G^0_\uparrow(\tau_2, \boldsymbol{q})}\right). \tag{4.4}$$

Reconnect *Reconnect* is the key update of our procedure. It randomly selects one of the T matrices, except the last one. In diagram order N, there are $N-1$ possible choices. Suppose that a T matrix with parameters $(\tau_t, \boldsymbol{p}_t)$ and an impurity neighbor adjacent to the right with parameters $(\tau_p, \boldsymbol{p}_\downarrow)$ is selected. The update then proposes to swap the incoming bath propagator with the incoming bath propagator of its right neighbor. There is a unique way of swapping as we are not working in cyclical representation. Accordingly, the former bath propagator times τ_1 and τ_2 are exactly mapped on new times τ_1' and τ_2'. Index 1 labels the bath propagator linked to the selected T matrix. Note that the mapping of the bath propagator momenta to the corresponding new momenta is not clear at this instant, as the shape of the current topology has to be reflected. In the moment of linking the new propagator configuration, the underlying momenta have to be adjusted in a manner described below. Last, the resulting diagram has to be checked for one-particle-irreducibility – the update has to be rejected if any impurity propagator line turns out uncovered. Subsequent application of *Reconnect* updates allows to reach every bath propagator configuration and guarantees ergodicity.

More precisely, the update separates into three different cases depending on the current diagram configuration. The first diagram topology (cf. Fig. 4.3) is identified by having a mushroom-structure on the selected T matrix – its incoming bath line is connected with its outgoing bath line. Since swapping will transfer a hole into a bath particle, it is necessary to create its new particle momentum $\boldsymbol{q}$. This is done by uniform seeding on the interval $[-k_{\max}, k_{\max}]$ for each component of $\boldsymbol{q}$, where $k_{\max}$ introduces the momentum cutoff of our procedure. The update is rejected if $|\boldsymbol{q}| > k_{\max}$ or if $|\boldsymbol{q}| < p_F$. Concerning underlying momenta, the selected T matrix is assigned the momentum $\boldsymbol{p}$ of the right neighboring T matrix, while its right impurity neighbor

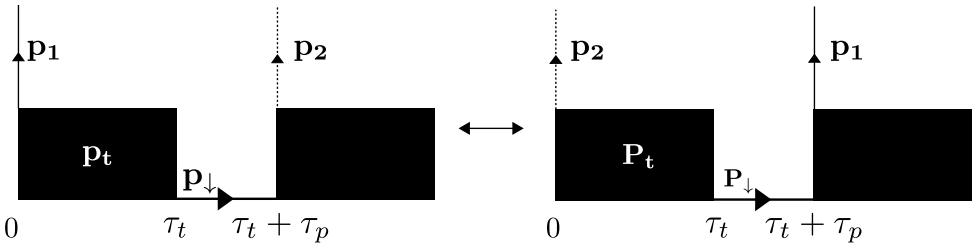

Figure 4.4.: Illustration of the third case of update *Reconnect*. The dotted and full vertical bath propagator lines are connected to arbitrary T matrices in the diagram (as long as neither the full line of the left figure nor the dotted line of the right figure is connected to itself).

obtains $\boldsymbol{p} - \boldsymbol{q}$. It is easy to compute final times

$$\begin{aligned} \tau_1' &= \tau_2 - \tau_t - \tau_p \\ \tau_2' &= \tau_p. \end{aligned} \tag{4.5}$$

The acceptance ratio is

$$\min\left(1, \frac{\Gamma(\tau_t, \boldsymbol{p}) G_\downarrow^0(\tau_p, \boldsymbol{p}-\boldsymbol{q}) G_\uparrow^0(\tau_1', \boldsymbol{p}_2) G_\uparrow^0(\tau_2', \boldsymbol{q}) k_{\max}^d}{\Gamma(\tau_t, \boldsymbol{p}_t) G_\downarrow^0(\tau_p, \boldsymbol{p}_\downarrow) G_\uparrow^0(\tau_1, \boldsymbol{p}_1) G_\uparrow^0(\tau_2, \boldsymbol{p}_2) p_F^d}\right). \tag{4.6}$$

The second topology is identified by a link between the outgoing end of the selected T matrix and its right neighbor. Being the inverse of the latter update, only one more step is necessary. Instead of seeding new particle momentum, now the hole momentum has to be created on the selected T matrix, thus explaining the factor of p_F in Eq. (4.6). The acceptance ratio for the second topology is

$$\min\left(1, \frac{\Gamma(\tau_t, \boldsymbol{p}_t) G_\downarrow^0(\tau_p, \boldsymbol{p}_\downarrow) G_\uparrow^0(\tau_1, \boldsymbol{p}_1) G_\uparrow^0(\tau_2, \boldsymbol{p}_2) p_F^d}{\Gamma(\tau_t, \boldsymbol{p}) G_\downarrow^0(\tau_p, \boldsymbol{p}-\boldsymbol{q}) G_\uparrow^0(\tau_1', \boldsymbol{p}_2) G_\uparrow^0(\tau_2', \boldsymbol{q}) k_{\max}^d}\right). \tag{4.7}$$

All other cases are included in the third topology (cf. Fig. 4.4), defined by neither connecting the selected T matrix with its right neighbor nor with itself. Such cases are self-inverse. No seeding is necessary, all bath momenta are purely swapped or added. Determining final times is straightforward

$$\begin{aligned} \tau_1' &= \tau_2 - \tau_t - \tau_p \\ \tau_2' &= \tau_1 + \tau_t + \tau_p. \end{aligned} \tag{4.8}$$

Note that holes are defined to have negative times. Concerning momenta, only the selected T matrix and its right impurity neighbor have to be considered, yielding new momenta $\boldsymbol{P}_t$ for T matrix and $\boldsymbol{P}_\downarrow$ for impurity line:

$$\begin{aligned} \boldsymbol{P}_t &= \boldsymbol{p}_t + \boldsymbol{p}_2 - \boldsymbol{p}_1 \\ \boldsymbol{P}_\downarrow &= \boldsymbol{p}_\downarrow + \boldsymbol{p}_2 - \boldsymbol{p}_1 \\ \boldsymbol{p}_1' &= \boldsymbol{p}_2 \\ \boldsymbol{p}_2' &= \boldsymbol{p}_1. \end{aligned} \tag{4.9}$$

This results in the acceptance ratio

$$\min\left(1, \frac{\Gamma(\tau_t, \boldsymbol{P}_t) G^0_\downarrow(\tau_p, \boldsymbol{P}_\downarrow) G^0_\uparrow(\tau_1', \boldsymbol{p}_2) G^0_\uparrow(\tau_2', \boldsymbol{p}_1)}{\Gamma(\tau_t, \boldsymbol{p}_t) G^0_\downarrow(\tau_p, \boldsymbol{p}_\downarrow) G^0_\uparrow(\tau_1, \boldsymbol{p}_1) G^0_\uparrow(\tau_2, \boldsymbol{p}_2)}\right). \tag{4.10}$$

As a remark, we note that these basic updates apply to the molecule series as well. In fact, the differences between polaronic and molecular codes are so small that it is even possible to combine both into the same code [10]. Two things are worth mentioning: First, a check has to be incorporated into the code that ensures that each T matrix is covered by a propagator line. Second, the first order diagram is divergent if no cutoff is used – this might result in errors if the normalization references this diagrammatic structure. All other adjustments are straightforward.

4.2. Observables

After introducing the basic Monte Carlo sampling of our scheme, we turn to the measurement of observables.

For the determination of ground states, it is necessary to get access to polaron and molecule energies. The full Green's function $G_\downarrow(\omega, \boldsymbol{p})$ experiences a pole at the exact quasiparticle polaron energy E_{pol} [72]. At the same time, solving Dyson's equation for $G_\downarrow$ gives

$$G_\downarrow(\omega, \boldsymbol{p})^{-1} = G^0_\downarrow(\omega, \boldsymbol{p})^{-1} - \Sigma(\omega, \boldsymbol{p}). \tag{4.11}$$

Since $G_\downarrow(\omega = E_{\mathrm{pol}}, \boldsymbol{p})^{-1} = 0$, this yields

$$E_{\mathrm{pol}} = \epsilon_{p,\downarrow} + \Sigma(E_{\mathrm{pol}}, \boldsymbol{p}), \tag{4.12}$$

where $G^0_\downarrow(\omega, \boldsymbol{p})^{-1} = \omega - \epsilon_{p,\downarrow}$ was used. Note that there is no reference to $\mu^0_\downarrow$ in this expression. All dependence on $\mu^0_\downarrow$ has to be corrected along the transformation from imaginary time to real frequencies by

$$\Sigma(\omega, \boldsymbol{p}) = \int_0^\infty \mathrm{d}\tau e^{(\omega - \mu^0_\downarrow)\tau} \Sigma(\tau, \boldsymbol{p}). \tag{4.13}$$

As our Monte Carlo routine is sampling diagrams according to $\Sigma(\tau, \boldsymbol{p})$, all that has to be done to estimate this quantity is a binning of the total diagram time as a standard Monte Carlo vector observable. With this, $\Sigma(\omega, \boldsymbol{p})$ is accessed by Eq. (4.13). Now, the roots of

$$\omega - \epsilon_{p,\downarrow} - \Sigma(\omega, \boldsymbol{p}) \tag{4.14}$$

can be estimated numerically so that a solution to Eq. (4.12) is found.

In complete analogy to the polaron case [10], the molecule energy E_{mol} is marked by a pole of Q, giving $Q(\omega = E_{\mathrm{mol}}, \boldsymbol{p})^{-1} = 0$. As

$$Q(\omega, \boldsymbol{p})^{-1} = \Gamma(\omega, \boldsymbol{p})^{-1} + \tilde{K}(\omega, \boldsymbol{p}), \tag{4.15}$$

the molecular energy can be estimated by

$$\tilde{K}(E_{\mathrm{mol}}, \boldsymbol{p}) = \Gamma(E_{\mathrm{mol}}, \boldsymbol{p})^{-1}. \tag{4.16}$$

The transformation from imaginary time to real frequencies is

$$\tilde{K}(\omega, \boldsymbol{p}) = \int_0^\infty \mathrm{d}\tau e^{(\omega - \mu^0_\downarrow)\tau} \tilde{K}(\tau, \boldsymbol{p}). \tag{4.17}$$

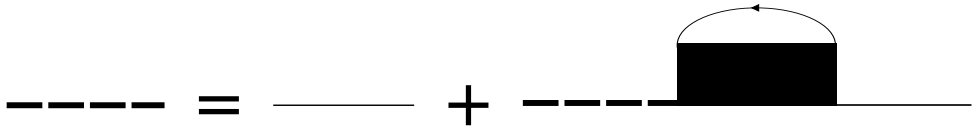

Figure 4.5.: Dyson's equation for partially bold propagators. $G^1_\downarrow$ is depicted by a bold dashed line.

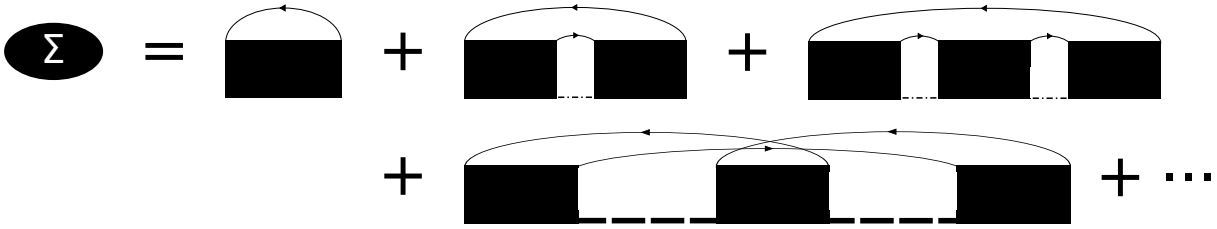

Figure 4.6.: The first contributions to a partially bold series are shown. $G^1_\downarrow$ is depicted by a bold dashed line and $G^1_\downarrow - G^0_\downarrow$ by a dashed-dotted line.

Another important observable is the quasiparticle residue Z. It can be extracted from the asymptotic decay of the full propagator $G_\downarrow(\tau, 0) \underset{\tau\to\infty}{\longrightarrow} -Ze^{-(E_{\mathrm{pol}}-\mu^0_\downarrow)\tau}$ [10]. This form implies that a suitable Monte Carlo estimator for the residue is $Z = (1 + A(E, 0))^{-1}$ with

$$A(E_{\mathrm{pol}}, 0) = -\int_0^\infty \mathrm{d}\tau e^{(E_{\mathrm{pol}}-\mu^0_\downarrow)\tau}\tau\Sigma(\tau, 0). \tag{4.18}$$

As a last observable, the polaronic spectral function

$$\mathcal{A}(\omega, \boldsymbol{p}) = -2\,\Im\Big(\omega - \epsilon_{\boldsymbol{p}} + \mu^0_\downarrow - \Sigma(\omega, \boldsymbol{p}) + i0\Big)^{-1} \tag{4.19}$$

is introduced. It can be estimated by analytic continuation of $G(\tau, \boldsymbol{p})$ to real frequencies [44, 81]. We access the full Green's function in imaginary time by a Fourier transform of $\Sigma(\tau, \boldsymbol{p})$ to $\Sigma(i\omega, \boldsymbol{p})$, subsequent application of Dyson's equation to get $G(i\omega, \boldsymbol{p})$ and another Fourier transform back to imaginary time.

4.3. Partially bold diagrammatic Monte Carlo

The original paper of Prokof'ev and Svistunov [10] introduced two versions of diagMC for the Fermi polaron, a bare approach that is similar to the algorithm explained above, and a self-consistent bold approach that writes the full Green's function G in terms of itself and approximates the correct answer iteratively in the spirit of Ref. [75].

However, using full Green's functions as self-consistent input has the disadvantage of increasing sampling space drastically by forcing the tabulation of G in both imaginary time and momentum. It is therefore beneficial to use the fact that first-order contributions dominate the fully bold propagator and construct a partially bold diagrammatic series out of quantities that are easily tabulated. It is possible to put the analytically known first-order self-energy into Dyson's equation in Matsubara frequency space to obtain the first-order Green's function, as shown in Fig. 4.5. A Fourier transform yields the basic propagator $G^1_\downarrow(\tau, \boldsymbol{p})$ without stochastic errors. Only a few modifications are necessary to adjust the Monte Carlo routine: First, every diagram containing at least one first-order self-energy diagram (shown in the left panel of Fig. 4.1) has to be excluded from measurements. Second, it is no longer forbidden to connect adjacent T matrices, just as in

a fully bold code [10] – the only difference is that the associated impurity weight is now $G^1_\downarrow - G^0_\downarrow$. The first diagrams contributing to the partially bold series are shown in Fig. 4.6.

We also extended the molecule code to include partially bold propagators. This extension is almost identical to the bold polaron code. Linking T matrices is readmitted with the same (now non-artificial) weight $G^1_\downarrow - G^0_\downarrow$ for impurity propagators. The only new feature concerns the first-order molecule diagram that is now sampled and has to be calculated with impurity weight $G^1_\downarrow - G^0_\downarrow$. By this means, the ultraviolet divergence is cured and a second, independent molecule series is constructed which helps confirming robustness and reproducibility of the results. Resummation [10] is still needed for this new series.

As a last comment on bold sampling, we would like to draw attention to the flaws of bold diagMC. First, if the Dyson series is not absolutely convergent, the rearrangement of this series into the fully or partially bold series is potentially harmful, as it constitutes a (though physically motivated) regrouping of terms which can yield any result for non-convergent series [82]. Second, many series in quantum field theory are asymptotic expansions, implying that results begin to get better and better with increasing expansion order until some maximum expansion order $N_{\max}$ is reached, after which the factorial growth of the number of diagrams leads to huge oscillations. In such a case, using a bare series is a common procedure, whereas the bold approach captures diagrams of higher order from the start. Summarizing this line of argument, a bold diagrammatic approach seems only reasonable if the underlying series is convergent.

4.4. Diagram regrouping and resummation

As diagrammatic expansions are in general not absolutely convergent, an important tool to study the underlying series is resummation [10]. This resummation procedure requires a discussion in more detail. Typically we find the molecular energies to be stable, but the polaron energies in the Bose-Einstein-condensate limit are harder. Sharp resummations are potentially dangerous if the maximum sampling order is not high enough as can be seen as follows: With a strong resummation method, the produced curve is almost flat for low expansion orders and then bends down sharply for higher orders. Weak resummation methods on the other hand have more curvature for low expansion orders and flatten off if the order of divergence of the series is weak enough. There is thus a risk with strong resummation methods if only low expansion orders can be reached in the sense that a possibly strong curvature is missed, resulting in an apparently converging but wrongly extrapolated result in close vicinity to the first-order result. This effect is demonstrated in the left panel of Fig. 4.7 at unitarity. Note that the bare series is monotonously decreasing which makes a high maximum resummation order necessary to extract the correct answer. Summing it up: the more sign-alternating the bare series is, the better resummation works.

A typical resummation method is the Riesz resummation method. These resummations will act upon self-energy series which can be written as $\mathcal{S} = \sum_N \mathcal{S}_{(N)}$, where $\mathcal{S}_{(N)}$ contains all contributions of diagrams of order N. The order of a self-energy diagram is defined as the number of interaction T matrices. The resummed self-energy series $\mathcal{S}'$ for some given maximum order L is defined [10] as

$$\mathcal{S}'(L) = \sum_{N=1}^{L} \mathcal{S}_{(N)} F_N^{(L)}, \tag{4.20}$$

where F is given by the Riesz coefficients

$$F_N^{(L)} = \left(\frac{L-N+1}{L}\right)^\delta. \tag{4.21}$$

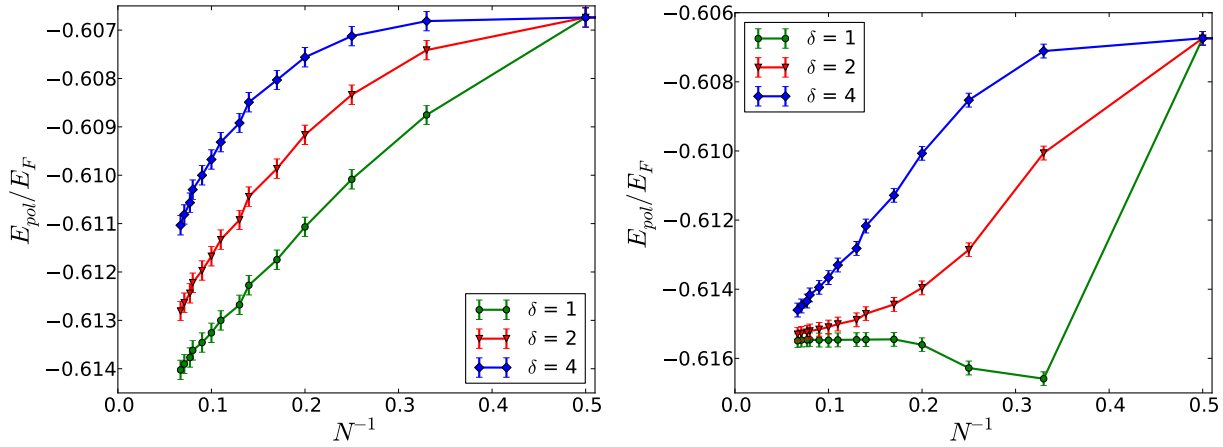

Figure 4.7.: *Left:* Resummation methods of type Riesz with different exponents δ are compared for unitarity in a three-dimensional setup. The plot shows polaron energies depending on maximum sampling order. *Right:* Resummation methods of type Riesz with different exponents δ applied to the modified bare series (see Eq. (4.23)) are compared at unitarity in a three-dimensional setup. The plot shows polaron energies depending on maximum sampling order.

δ fixes the strength of the resummation: For $\delta = 0$, no resummation is performed at all, while only the first-order contribution is maintained in the limit $\delta \to +\infty$. If this method is used on molecular series, it might be beneficial to set $F_2^{(L)} = 1$ as this ensures that the first contributing diagram (which is of second order for molecules) always contributes with full weight.

We introduce a regrouping technique which seems to saturate much faster. Provided the series is absolutely convergent, this is always allowed. It is based on a regrouping of terms in the bare series in such a way that sign-alternation is maximized. The technique consists in splitting $\mathcal{S}_{(N)}$, the self-energy contributions of order N, into two parts:

$$\mathcal{S}_{(N)} = \mathcal{S}^r_{(N)} + \mathcal{S}^{ir}_{(N)}, \tag{4.22}$$

where $\mathcal{S}^r_{(N)}$ collects all diagrams containing at least one T matrix linked by a hole to itself, as in the left hand side of Fig. 4.1, and $\mathcal{S}^{ir}_{(N)}$ gathers the rest. We propose a new series $\mathcal{S}' = \sum_N \mathcal{S}'_{(N)}$ which aims to maximize sign-alternation in $\mathcal{S}'_{(N)}$. The coefficients in the resummation procedure depend on the expansion order for $k \in \mathbb{N}$ as

$$\begin{aligned}
\mathcal{S}'_{(1)} &= \mathcal{S}_{(1)}, \\
\mathcal{S}'_{(N=2k+1)} &= \mathcal{S}^{ir}_{(N)} + \frac{1}{2}\mathcal{S}^{ir}_{(N-1)} + \frac{1}{2}\mathcal{S}^{r}_{(N)}, \\
\mathcal{S}'_{(N=2k)} &= \mathcal{S}^{r}_{(N)} + \frac{1}{2}\mathcal{S}^{r}_{(N-1)} + \frac{1}{2}\mathcal{S}^{ir}_{(N)}.
\end{aligned} \tag{4.23}$$

These coefficients are in principle arbitrary – our choice was designed to show fast saturation as can be seen in the right panel of Fig. 4.7 for the case of the Fermi-polaron at unitarity: The application of conventional Riesz resummations on the reordered series illustrates that the manually implemented oscillations make it possible to read off polaron energies reliably and allow for a clear statement whether the expansion order is high enough or not. When reverting the roles of reducible and irreducible in Eq. (4.23), the same answer can be found but only after a stronger resummation. Note that although the sum of diagrams of a specific order of the unitary

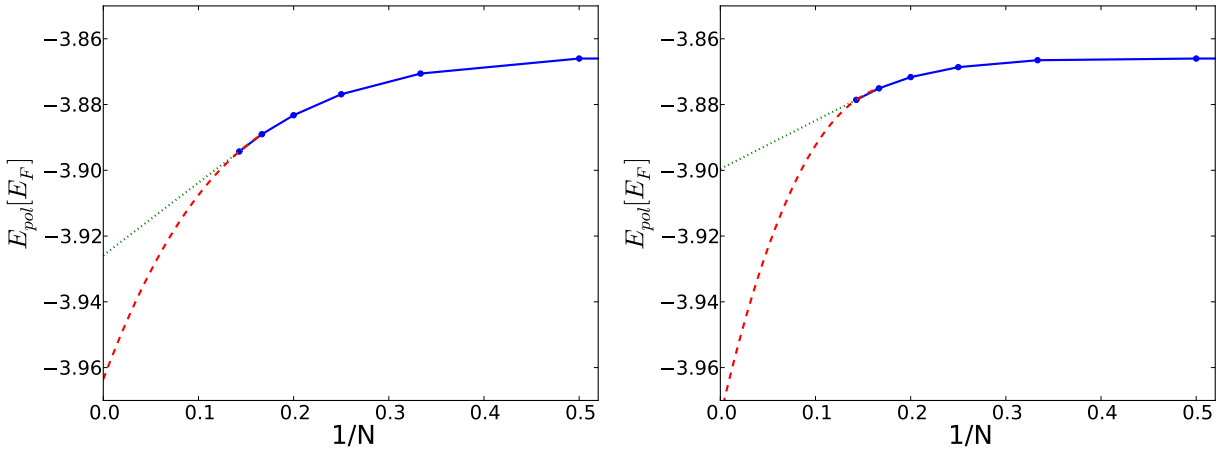

Figure 4.8.: *Left:* The extrapolation procedure on resummed data is demonstrated for $\eta = -0.248$ and $\delta = 2$. The dotted curve shows the linear part, whereas the dashed line is a fit with f. *Right:* The extrapolation procedure on resummed data is demonstrated for $\eta = -0.248$ and $\delta = 4$. The dotted curve shows the linear part, whereas the dashed line is a fit with f. Note that the resulting error bar exceeds the corresponding $\delta = 2$ error bar.

polaron series is vanishing within error bars, the different terms are not small.

As the regrouped series agrees with the results of the standard bare series, this might indicate that the polaron Dyson series is convergent or that the maximum expansion order $N_{\max}$ of its asymptotic expansion is essentially infinity at unitarity. Nevertheless, Fig. 7 of Ref. [67] suggests that the series might be asymptotic in fact, as a doubly bold regrouping shows clear signs of growing fluctuations for increasing expansion order after an initial improvement of results.

4.5. Extrapolation of resummed data

We conclude this chapter by explaining the details of our extrapolation procedure. Its use is most delicate for cases where the maximum diagram order is small. Therefore, it is illustrative to use a quasi-two-dimensional Fermi-polaron series (characterized by the dimensionless parameter $\eta = \ln(p_F a_{2D})$) to explain this technique, since the maximum expansion order is approximately 8. For these systems, it is additionally necessary to deal with large binding energies, hence aggressive resummation has to be applied to the bare series in order to be able to extrapolate to infinite expansion order. However, this tends to conceal the curvature of the series in the first points, leading to an initially flat curve.

Our extrapolation procedure is the following: For the upper value of the error bar, we apply linear extrapolation on the Riesz-resummed data with Riesz exponent δ. In this linear extrapolation, only the two points corresponding to highest and second highest expansion order are taken into account. For the lower value of the error bar, we *assume* a worst-case scenario with large curvature of the extrapolated curve, according to the following fit function f of parameters a and b:

$$f(N^{-1}, a, b) = 4\ \delta \left(\frac{1}{3} N^{-3} - \frac{3}{10} N^{-2} \right) + a N^{-1} + b. \tag{4.24}$$

N denotes the maximum expansion order. We emphasize that the curvature of this function is empirically set by us. This curve includes only the highest and second highest expansion points. An important feature of f is the dependence on the Riesz exponent. This ensures that a stronger

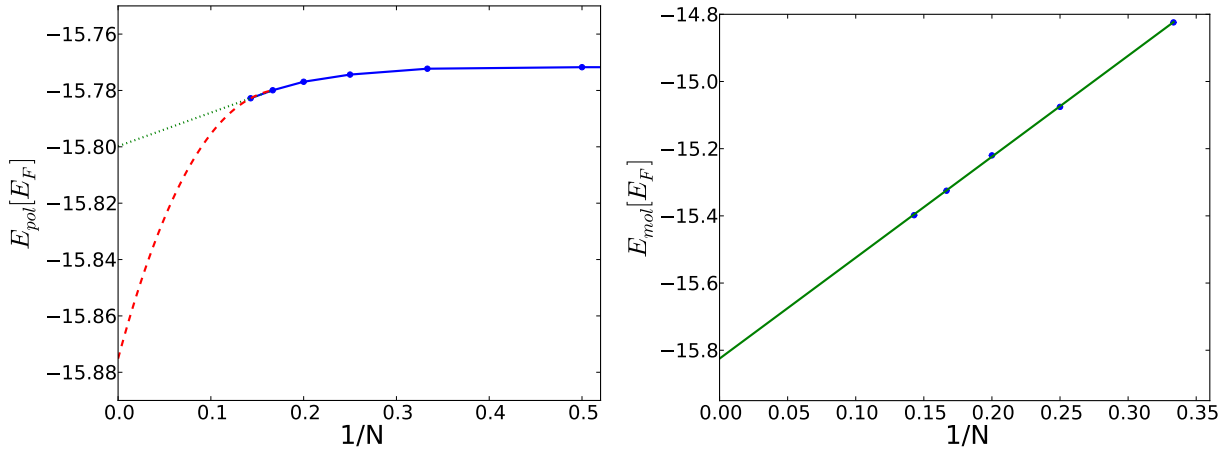

Figure 4.9.: *Left:* The extrapolation procedure on resummed data is demonstrated for $\eta = -1.02$ and $\delta = 4$. The dotted curve shows the linear part, whereas the dashed line is a fit with f. *Right:* The extrapolation procedure on resummed data is demonstrated for a molecule with $\eta = -1.02$ and $\delta = 6$.

resummation results in a bigger error bar due to extrapolation errors. The fit f can also be used for bare data ($\delta = 0$). In this case, we replace δ by -1 in Eq. (4.24). Note that the error bars represent a variability of results due to systematic origins corresponding to the one-σ-interval. The result of this technique is shown in the left panel of Fig. 4.8. For a maximum expansion order of 7, the two ways of extrapolating are shown in comparison. If the maximum expansion order was 6, then this error bar would increase, just as one would expect regarding the loss of information. The right hand side of Fig. 4.8 uses a sharper resummation on the same data, demonstrating that the error bar increases with δ.

Therefore, it becomes clear that the weakest possible resummation procedure (among the ones resulting in a monotonously decaying series) should be applied. As a final example, we show our resummation for a polaron point inside the quasi-two-dimensional transition region in the left panel of Fig. 4.9. Here, resummation with $\delta = 2$ is too weak, so $\delta = 4$ has to be used, resulting in a stronger curvature. It is important to stress that these two extrapolations represent assumed worst-case scenarios. Finally, as always for diagMC, the extrapolation result has to be checked with available experimental or theoretical results, thus justifying its application in retrospect. In our case, these results would be variational two-particle-hole results which we expect to be exact[1]. As an example for a system in which extrapolated error bars were underestimated for a similar system, consult Fig. 22 of Ref. [83].

For molecular energies, resummation is more straightforward. As this series is typically alternating, resummed curves can often be extrapolated linearly. This is demonstrated in the right panel of Fig. 4.9: The last four points are well fit by a straight line. However, as this resummation involves the same dangers as described above, we try to vary both the fitting (e.g., fitting three of the four last points) and the resummation technique to test the variability of this result.

[1]Chapter 5 discusses this statement in detail.

5

The Fermi-polaron problem in a quasi-two-dimensional geometry

In Ref. [20], it was shown that a variational expansion in terms of particle-hole excitations quickly converges to the full many-body answer for the case of a 3D Fermi-polaron problem at unitarity. Later, Vlietinck et al. simulated the Fermi polaron in the theoretical limit of pure 2D geometries in a diagMC study [84]. For strong-enough interactions, they noticed growing fluctuations with expansion order that were claimed to be resummable and to result in a final answer close to the single-particle-hole (1-ph) variational result. This raises the question whether particle-hole ansätze always provide a simple and accurate description of the Fermi polaron. Also, the growing fluctuations in the 2D case should be investigated further in order to understand if they are a consequence of the diagrammatic expansion technique not being aligned with a particle-hole picture.

In realistic experiments, the 2D limit always has to be accessed by a harmonic confinement in z direction. With ultracold atoms [48] a quasi-two-dimensional (quasi-2D) geometry can be made by confining the dilute gas strongly in a plane by an external laser, which was done successfully in the experiment in Ref. [31] for fermionic atoms. The quantum simulation of a 2D Fermi system may provide new insight in, e.g., high-T_c superconductors. In order to keep an independent check on these experimental results, it is thus of prime importance to have better theoretical control over interacting 2D fermionic systems, including the 2D Fermi-polaron problem.

Furthermore, although it was initially believed that no polaron to molecule transition is possible in a pure 2D Fermi-polaron problem [32] (due to an incorrect description of the Bose-Einstein-condensate (BEC) limit in lowest-order perturbation theory), it was shown that a transition can occur provided the molecules are dressed by ph fluctuations [33]. Also trimers can be found for mass imbalance [14]. Given this initial controversy, a numerical calculation going beyond the lowest-order perturbation theory or the simplest variational ansatz is warranted in order to evaluate the smallness (or absence) of the fluctuations beyond the first-order results, thus allowing definite statements about the molecular state in two dimensions.

This motivates to apply diagMC to quasi-two-dimensional geometries for the Fermi-polaron problem with equal masses. Just as in Ref. [84] we will see that the ground-state energy remains close to the 1-ph result and that the 2-ph result is almost exact, with the remaining fluctuations being *very small* in ph-order. The small parameter that can be exploited in the diagrammatic approach is the restricted phase space for the holes [20]. Extending diagMC to the case of a quasi-two-dimensional geometry is done straightforwardly by restricting the momentum integrals to two dimensions and by using the relevant quasi-two-dimensional T matrix from Sec. 3.5. We define the dimensionless interaction parameter $\eta = \ln(p_F a_{2D})$.

The rest of this chapter proceeds as follows: After presenting an alternative diagrammatic expansion technique in Sec. 5.1 that connects with the variational approach, the polaron-molecule transition is presented in Sec. 5.2. Last, the validity of the quasi-two-dimensional approach is discussed in Sec. 5.3.

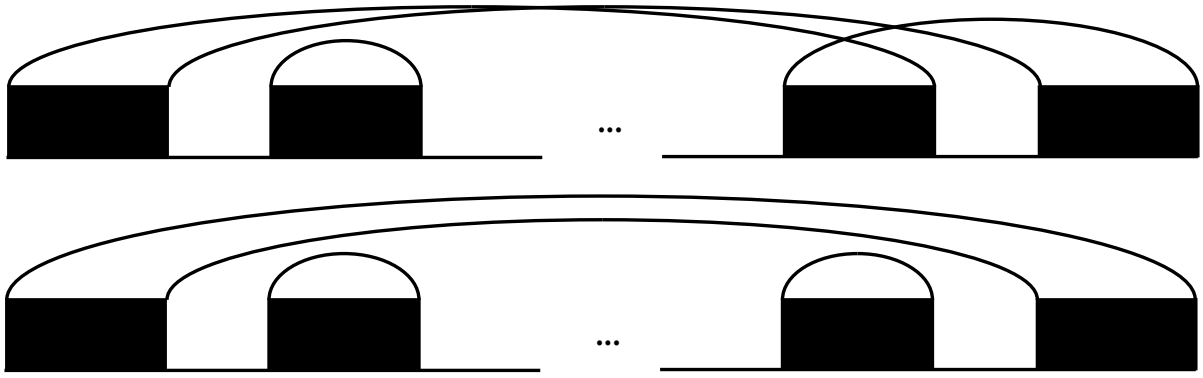

Figure 5.1.: Examples of (top) "exchange-hole" and (bottom) "direct-hole" contributions to the 2-ph diagrams are shown. This demonstrates that every order $N > 2$ has at least two diagrams counting as 2-ph.

5.1. Expansion technique

Arguably, the main bottlenecks in diagrammatic Monte Carlo are series convergence and the sign problem. There is no guarantee that the perturbative expansion in Feynman diagrams is a convergent series; in fact, some of the most famous theories in physics, such as quantum electrodynamics, are asymptotic [85]. Although the Dyson series for the Fermi-polaron in 3D at unitarity experiences diminishing fluctuations with increasing expansion order [9, 10], such behavior cannot be assumed for fermionic many-body problems in general. The series is often nonmonotonous, showing increasing fluctuations [67, 84], and given the low expansion orders that can be reached (of the order of 12 in 3D [67] and 8 in 2D [84] for the Fermi-polaron problem), it is impossible to know the fate of the series convergence by inspecting order-by-order results. In such cases the best one can do is resort to resummation techniques provided the series is resummable. All resummation techniques that are strong enough to overcome the divergence of the series must then necessarily give the same result for infinite extrapolation order. Typically, Abelian resummation techniques were used in Refs. [78], [84] and [67], characterized by a very strong suppression of higher-order self-energy contributions, whereas weaker resummation methods did not yield a unique answer. Although the extrapolated results seemed to agree within the (small) error bars, this is at best a hint, and ultimately, only "nature can provide the proof" [78].

For a divergent series, regrouping terms is problematic and can result in any (unphysical) result. The standard approach groups the terms according to the number of T matrices and sums these diagrams with the same coefficients. We now discuss a second, physically motivated way of regrouping based on the arguments presented by Combescot and Giraud [20]. These authors explained a remarkable cancellation of higher-order terms first seen in Refs. [9] and [10] for the 3D Fermi-polaron at unitarity. They argued that the subspace of $(n+1)$ ph pairs (and higher) can be decoupled from the subspace of n ph pairs to a very good approximation because the summation over the particle lines dominates over the summation over the hole lines. The ground-state in the 1-ph space is the *Chevy ansatz* and is already a very good approximation, whereas the ground state in the 2-ph space provides a small correction and so on. This provides a cascade of better, *variational* approximations. Diagrammatically, all contributions from the 1-ph space are contained in our lowest-order diagram. The 2-ph contributions can be identified [84] by taking all diagrams that have at most two particle and two hole lines at any moment in imaginary time. There are, in principle, an infinite number of them: although the two holes have only a direct contribution and an exchange contribution, the two particles can scatter arbitrarily. This is illustrated in Fig. 5.1. The sum of all these diagrams must yield the ground-state energy in the 2-ph subspace and agree with the wave-function ansatz, resulting in an upper bound to

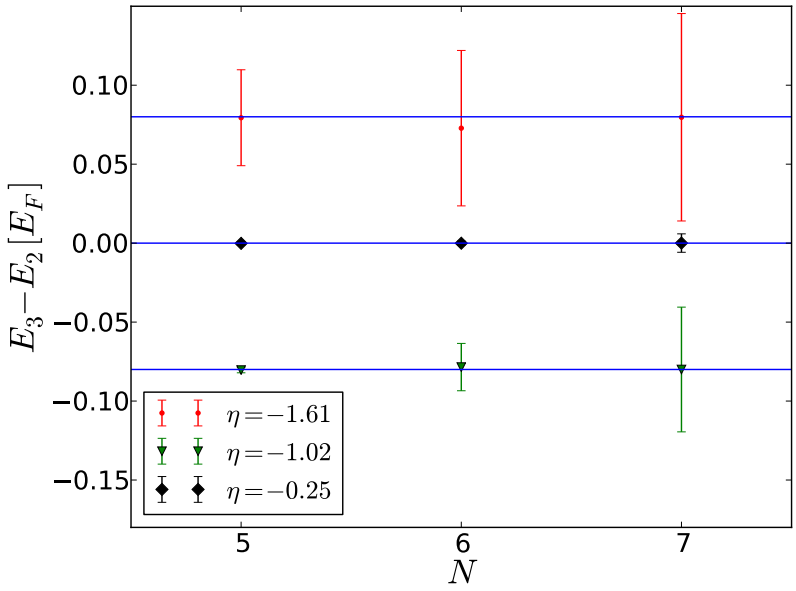

Figure 5.2.: Difference in energy between the 2-ph and 3-ph contributions as a function of the number of T-matrices N in the Feynman diagrams. Since this difference is essentially vanishing within the error bars, rapid convergence in the ph expansion order is seen. Note that two of the data sets have been offset by $\pm 0.08 E_F$ for clarity. η is defined as $\eta = \ln(p_F a_{2D})$.

the true ground-state energy. This scheme suggests that one can regroup the diagrams in the number of ph lines and extrapolate the result. Within this subspace the diagrammatic expansion may still diverge, but if the resummation is inadequate, one may resort to other techniques (such as a brute force evaluation or variational Monte Carlo) to obtain the answer in this restricted subspace.

In the molecular sector, the 1-ph sector is already accurate, as was demonstrated in Ref. [22] for a 3D polaron problem.

The regrouping works very well not only deep in the BCS phase but also in the vicinity of the polaron to molecule transition. As shown in Fig. 5.2, the difference between 2-ph and 3-ph contributions is vanishing on the order of the error bars, indicating that the 2-ph channel is already sufficient for precise calculations. This holds for all accessible expansion orders, labeled by the number of T matrices. We note that the 2-ph result itself has not converged up to the maximum expansion order, and its series is almost surely asymptotic. Nevertheless, resummation of the 2-ph series yields the same result as the wave-function technique, at least as long as the polaron is the true ground state. For nonzero momentum, this is no longer the case, and the polaron can decay. In the field theory this is signaled by a nonzero complex part of the particle self-energy (or finite width of the polaron peak in the spectral function). In such cases, the wave function is no longer variational, but the grouping in terms of the number of ph lines in diagMC is still a rapidly converging series (not shown). We do not show results for 4-ph because the first contribution occurs for T matrix expansion order 7, which gives us only a single point to this subspace. In three dimensions, we observed vanishing contributions of 4-ph and 5-ph diagrams.

The above arguments show that using a bold code (with respect to the number of T-matrices as expansion order) is a questionable strategy: it mixes up the different contributions from different ph channels.

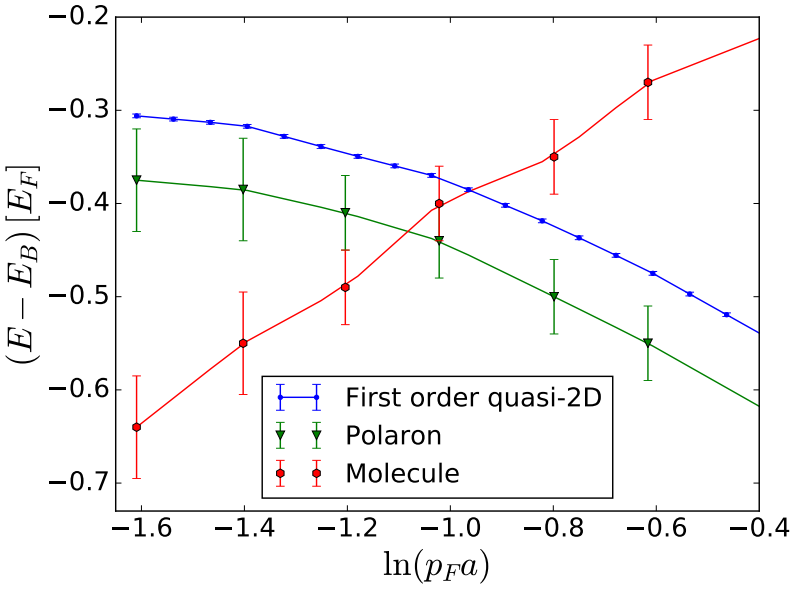

Figure 5.3.: Polaron and molecule energies as obtained by the diagrammatic Monte Carlo method. For low values of the interaction parameter $\ln(p_F a)$, the molecule is the stable ground state, while the polaron (green triangles) dominates in the weak-coupling regime $\ln(p_F a) \gtrsim -1$. The first-order quasi-two-dimensional energy is also shown for comparison, from which we see that the many-body modification is nearly independent of the interaction strength. These data were produced for a trapping frequency of $\omega_z = 5000 E_F$.

5.2. Polaron-Molecule transition

Our results for the polaron and molecule energies E in the quasi-two-dimensional geometry are shown in Fig. 5.3. For weak two-body coupling $\ln(p_F a) \gtrsim -1$ the polaron state is the stable ground state, thus identifying the BCS regime in the limit $\ln(p_F a) \to +\infty$; for $\ln(p_F a) \lesssim -1$, the molecule becomes energetically favorable and is referred to as the BEC regime in the limit $\ln(p_F a) \to -\infty$. These curves were sampled at a trapping frequency of $\omega_z = 5000 E_F$, which is high enough to justify the assumption of only populating the lowest oscillator mode: The binding energy E_B is at most $\omega_z/70$. The plot also shows the first-order contribution to the series, which is normally very close to the final result [84]. We used the standard approach with the number of T matrices as the expansion parameter to perform the resummation, but the resummation method we used depends on the size of the binding energy E_B: For large E_B, it becomes necessary to use sharper Riesz resummations [10] on the reordered series. The error bars in Fig. 5.3 appear to increase when one goes deeper into the BEC phase. This is, to a large extent, the result of the rapid increase in E_B, which is subtracted in the plot, whereas the calculations produce error bars on E instead of $E - E_B$. The pure two-dimensional first-order contribution $(E - E_B)$ curve agrees with the quasi-two-dimensional one within the error bars.

We find the crossing point at $\ln(p_F a) = -1.1 \pm 0.2$, which is in good agreement with previous studies [84] and experiment [31] and indistinguishable from the 2-ph result within our error bars, as could have been expected from the previous discussion.

For molecular energies, the series is alternating and can be well resummed with Riesz techniques. On the BCS side of the transition, the molecule is not stable any longer, which leads to a breakdown of the Monte Carlo estimators for energies above $-E_F$.

In principle, our scheme could be used to calculate the effective mass and contact coefficient of the system. However, as the error bar is on the scale of the difference between the first-

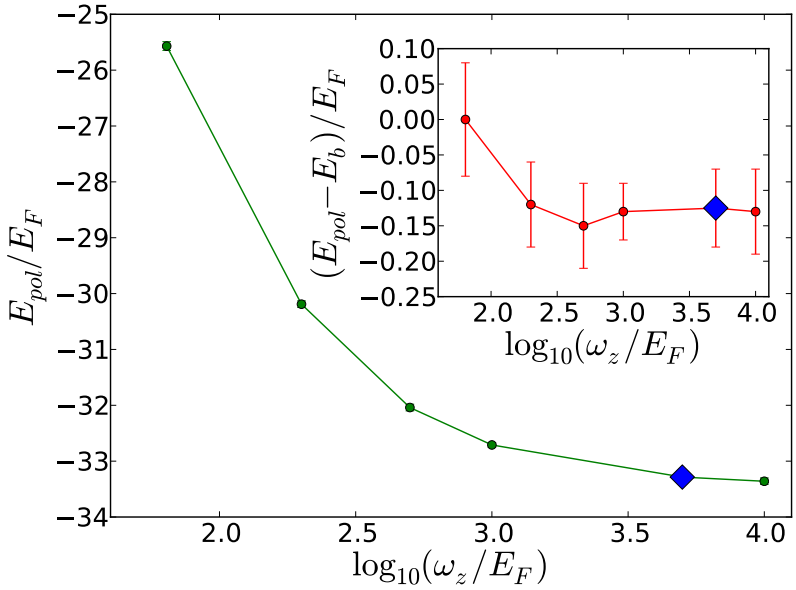

Figure 5.4.: The influence of ω_z on both polaron energy and binding energy is demonstrated. Using $\omega_z = 5000E_F$, the results are well saturated, justifying the assumption of neglecting transitions between the lowest and higher harmonic oscillator levels. The data in the plot were measured at $\ln(p_F a) = -1.4$. Blue diamonds mark the value of ω_z we use in our simulations. Riesz resummation was applied to the bare data.

order result and the extrapolated result, it is not reasonable to extract quantities depending on derivatives from our data. However, given the accurateness of the 2-ph result, precise estimates of ground-state quantities (such as the contact) can be obtained within the 2-ph subspace.

5.3. Validity of the quasi-two-dimensional approach

The approach to the 2D limit used in this work consists of using a strong harmonic confinement in the z direction and assuming that only the lowest harmonic oscillator is populated; that is, we neglect transitions between different harmonic oscillator levels. For strong enough confinement this approach is physically justified, and the 2D limit can be found by extrapolating results obtained for different ω_z. In order to check the validity of this quasi-2D approach and the corresponding quasi-2D T matrices, we compare polaron energies for several values of the confinement frequency ω_z in Fig. 5.4. It is remarkable that even the loosest confinement (which clearly violates the condition of populating only one mode of the oscillator in the z direction) shows good agreement for $E_{\mathrm{pol}} - E_B$. One would expect that high values of ω_z are necessary to reproduce the pure 2D limit because of the logarithmic dependence of the energy scale. Indeed, we see that $\omega_z = 5000E_F$ is high enough to observe the polaron-molecule crossover in this limit (it will be insufficient deep in the BEC phase for the polaron energy, however, because it has to be kept in relation to the binding energy to ensure exclusive population of the lowest mode). Lower values of ω_z may be acceptable too if $E - E_B$ is calculated. In the polaron experiment of Ref. [31], a confinement frequency of $\omega_z \approx 7.9E_F$ was used.

6 The Fermi-polaron problem for mass imbalance

Up to now, diagMC has only been applied to the special case of a Fermi polaron with equal masses of impurity and bath atoms. This is important as such a system can be created by different spin states of a homogeneous atomic gas. However, also mixtures like ^{6}Li–^{40}K are experimentally realizable in ultracold atom systems.

In this chapter, we present the results of our extension of diagMC to the case of arbitrary mass imbalance. The dependence of polaron energy and residue on the imbalance ratio is shown in Sec. 6.1. We demonstrate that two-particle-hole wave functions remain essentially exact in three dimensions (Sec. 6.2) and explain the implications for the mass-imbalanced phase diagram in Sec. 6.3. Determining the polaronic spectral function for mass imbalance helps understanding the stability of quasiparticles close to the limit of a heavy impurity. It features the repulsive polaron [86], an excited state with finite lifetime. This is shown in Sec. 6.4 together with results for Tan's contact parameter for a mass-balanced polaron system.

6.1. Polaron energy and residue

Fig. 6.1 plots the polaron energy at unitarity for different mass ratios $r = m_\downarrow/m_\uparrow$. While the variational *Chevy ansatz*, here labeled as first order, captures the whole curve qualitatively, its accuracy gets less precise for low r, i.e., a light polaron. Note that this energy curve reproduces the correct infinite mass limit [19] $E_{\mathrm{pol}} = -0.5$ for an imbalance ratio as low as $r = 2$. For the case of an immobile impurity, the polaron is subject to Anderson's orthogonality catastrophe [87] and the quasiparticle description is no longer appropriate. For a light impurity, the polaron energy decreases rapidly as the effective interaction is stronger for smaller reduced mass (as can be seen from the concrete form of the T matrix) at unitarity. The next subsection will show that this effect is weakened for finite scattering length. Eventually, a very light impurity will be subject to relativistic effects so that our description will no longer be appropriate. The extraction of error bars was based on conservative extrapolations of light Riesz resummation with $\delta = 1$. For details, consult Sec. 4.5.

Our results for the quasiparticle residue Z are depicted in Fig. 6.2. In this case, the first-order ansatz is qualitatively different, predicting a different position of the mass-imbalance ratio of maximum residue. This might indicate that the variational wave-function description works particularly well for energy based quantities, while it might take further particle-hole terms to capture the residue equally well. Therefore the quasiparticle with maximum residue can be found at higher r than estimated by first order. At low r, higher orders affect Z stronger and stronger, down to a ratio as low as $r = 0.125$ which is sufficient for most mixtures, e.g., ^{6}Li–^{40}K. In this regime, the differences between the diagrammatic answer and the first order result are most pronounced. For high r, the diagMC solution yields a roughly constant shift to the first order

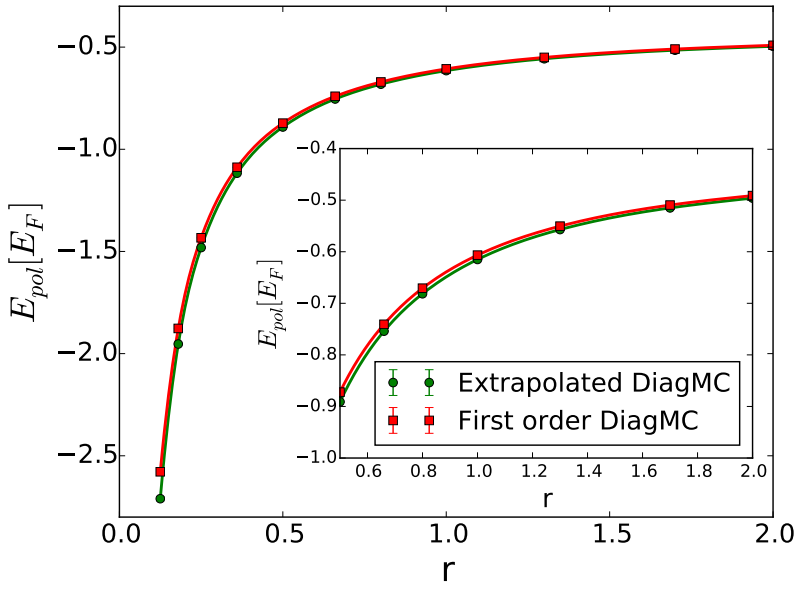

Figure 6.1.: Polaron energy at unitarity for different mass ratios r. The inset shows the flat part of the figure. Many-body effects get more pronounced for a lighter polaron.

answer.

As a trimer state acquires more and more strength with respect to the polaron state for decreasing r and as the molecular state is strengthened for increasing [17] r, it seems natural that the polaron residue takes on a maximum value in between – once it is no longer the ground state, its residue will decay quickly (although it will not be zero because there is no simple decay channel [27]). The measured residue is strictly lower than the first order variational result. This is remarkable as the Functional Renormalization Group analysis of Ref. [27] predicts a higher residue for unitarity at $r = 1$. Further investigation is needed to understand this discrepancy.

No resummation was used to extract the quasiparticle residues. For $r \gtrsim 0.5$, the series seemed to saturate within our maximum expansion order. The extrapolation error was approximated to be twice the fluctuation of the saturating points. For $r \lesssim 0.5$, the series changed and the saturation was not visible anymore. These points are therefore only valid if a linear extrapolation to infinite expansion order is appropriate. This extrapolation error was approximated by the method explained in Sec. 4.5.

Fig. 6.3 shows polaron energies at varying coupling strength in the BEC-regime for two different mass-imbalance ratios r. Both curves experience a peak of maximum dressing around $(p_F a)^{-1} = 0.4$. Decreasing the coupling further, this relative energy is decreased for both masses, although the light impurity is affected more strongly. Eventually, the heavy impurity has a higher effective dressing (relative to the binding energy) than the light impurity. This is a consequence of the $m_r/(2\pi a)$ term in the denominator of the T matrix that strengthens the effective interaction between impurity and bath atoms for increasing r at a given interaction strength. Note that these curves extend into the molecular sector [17] where the polaron ceases to be the ground state. Concerning the residue, no qualitative difference could be seen between the $r = 0.5$ and $r = 2$ curves.

6.2. Two-particle-hole channel

In Sec. 5.1, a remarkable precision of two-particle-hole wave-functions was found for polaron energies in quasi-two-dimensional geometries. A natural question is whether this approach

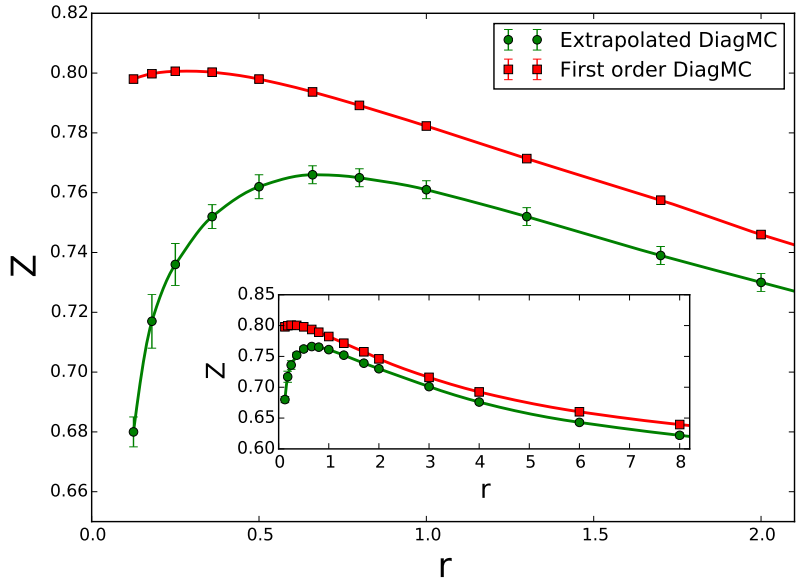

Figure 6.2.: Polaron residue at unitarity for different mass ratios r. The whole range of masses shows a clear difference between the first order result and the full diagrammatic answer. The inset shows the curve for additional values of r.

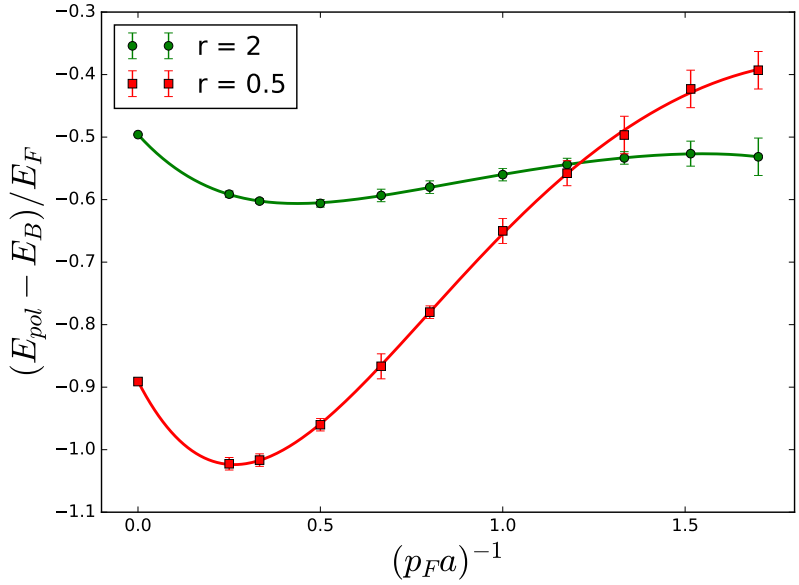

Figure 6.3.: The polaron energy of two values of r is plotted for various interaction parameters $p_F a$. Note that the binding energy $E_B = (2m_r a_{3D}^2)^{-1}$ is subtracted, where m_r is the reduced mass. For strong interactions, the light impurity acquires a higher effective dressing relative to the binding energy than the heavy impurity. This is eventually reversed in the BEC-regime.

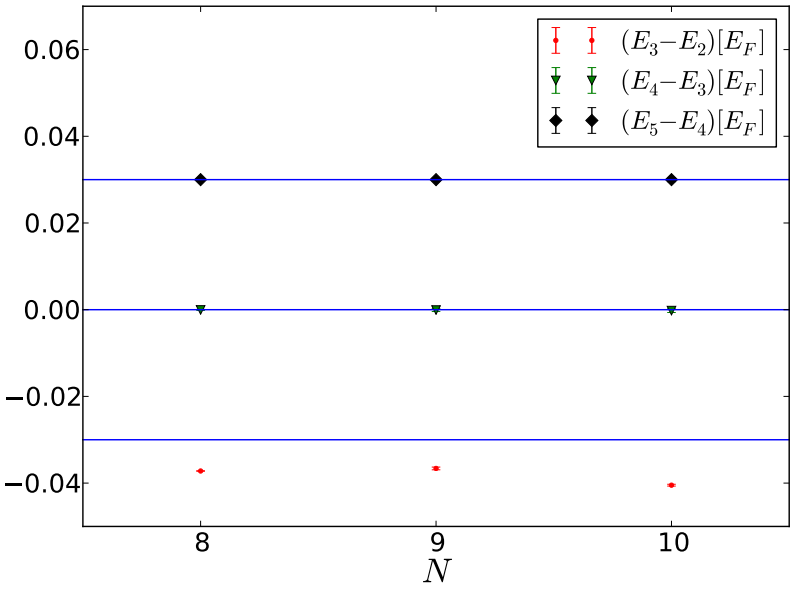

Figure 6.4.: Different contributions to the full polaron energy are compared for three maximum expansion orders N. E_n denotes contributions including up to n-particle-hole diagrams. Two of the curves have been offset by $\pm 0.03 E_F$ for clarity. The points were measured for a mass-imbalance ratio $r = 0.125$ at unitarity.

remains valid in three dimensions. Fig. 6.4 compares different particle-hole channels for three maximum expansion orders. For the selected measurement point (unitarity with imbalance $r = 0.125$), the three-particle-hole channel contributes slightly (i.e., $E_3 - E_2 \neq 0$), whereas four-particle-hole and five-particle-hole diagrams vanish within error bars. This confirms the observation that the two-particle-hole result is a very good approximation. The classification of diagrams into particle-hole classes breaks down for the fully bold approach, because each bold diagram captures bare diagrams of different particle-hole order. For the partially bold scheme, this does not apply since the diagrammatic structure of the partially bold Green's functions ensures that the propagation will start with zero holes and is guaranteed to switch to the 1-ph sector at least once.

6.3. Quantitative exactness of variational energies

In this section, the extraction of polaron and molecule energies by resummation is compared to variational one-particle-hole wave-functions. We choose the point $p_F a = 0.5$ and $r = 0.25$ of the mass-imbalanced phase diagram [17] as it stays away from the peculiarities of unitarity and the trimer threshold. Molecular energies (shown on the left hand side of Fig. 6.5) yield perfect agreement with the variational ansatz and motivate the quantitative correctness of variational wave functions for the Fermi-polaron problem. For the polaron (right part of Fig. 6.5), using a one-particle-hole wave function underestimates its energy slightly. Hence, it would be beneficial to use at least two-particle-hole precision for the polaron sector for a precise mapping of the phase diagram. Altogether, the phase diagram of Ref. [17] can be expected to be nearly exact. Nevertheless, as the polaron phase is underestimated, it will be shifted into the molecular sector. As this will reduce the small size of the nonzero-momentum molecular phase (labeled as Fulde-Ferrell-Larkin-Ovchinnikov phase, FFLO) further, it remains open whether this phase

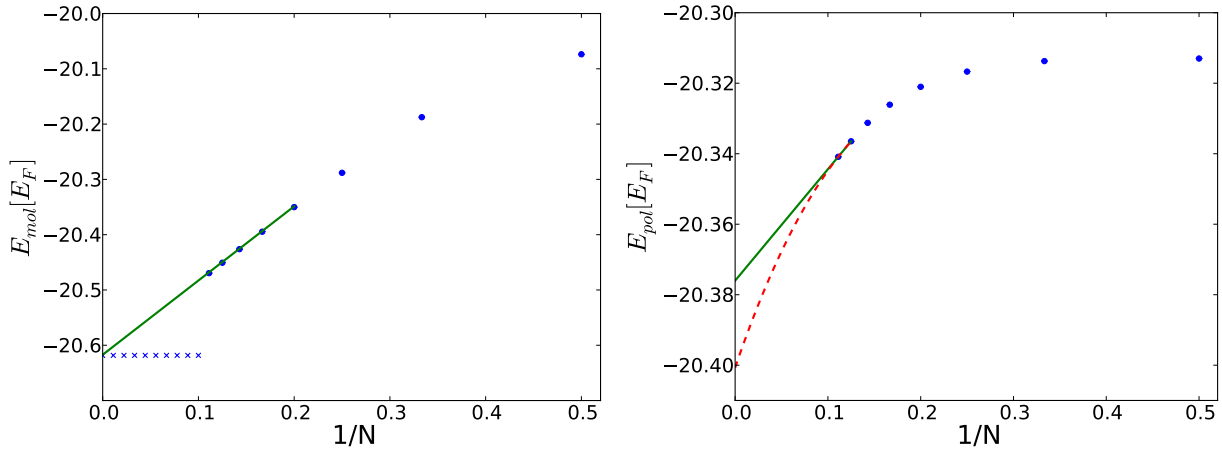

Figure 6.5.: *Left:* Molecule energy extrapolation for $p_F a = 0.5$ and $r = 0.25$. The maximum expansion order is denoted by N. The solid line corresponds to a linear fit of the last five points. The crosses mark the one-particle-hole result of Ref. [17]. Riesz resummation with exponent $\delta = 6$ was used. *Right:* Polaron energy extrapolation for $p_F a = 0.5$ and $r = 0.25$. The maximum expansion order is denoted by N. The solid line corresponds to a linear extrapolation of the last two points, the dashed line is a special fitting function explained in Sec. 4.5. The one-particle-hole result of Ref. [17] is identically with the point $N = 2$. Riesz resummation with exponent $\delta = 4$ was used.

really exists. We suggest to compute the phase boundary with high precision within a variational 2-ph polaron approach.

6.4. Spectral function and Tan's contact coefficent

Fig. 6.6 presents the spectral function for a mass-imbalance ratio $r = 2$. Although the energy corresponds to the infinite mass limit [19], the polaron remains a stable quasiparticle. The dispersion follows a parabola with positive effective mass, whereas at higher energies, the repulsive polaron (a metastable eigenstate of the Hamiltonian) can clearly be seen [24, 27].

As a last result, Tan's contact coefficient [22] $\mathcal{C}$ is measured. For a strongly population-imbalanced Fermi gas, it is linked to the dimensionless contact coefficient s by

$$\mathcal{C} = s \cdot k_{F,\downarrow}^3 k_{F,\uparrow}. \tag{6.1}$$

Here, $k_{F,\downarrow}$ is the Fermi momentum of the minority species which is finite for the strongly imbalanced Fermi gas. The dimensionless contact coefficient s can be accessed easily by calculating the derivative of the polaron energy with respect to the dimensionless coupling [22] $(k_{F,\uparrow} a_{3\mathrm{D}})^{-1}$. The resulting contact curve (which is not shown) agrees with first order calculations within error bars.

This concludes the fermionic many-body part. All notation introduced up to here will be dropped in the following.

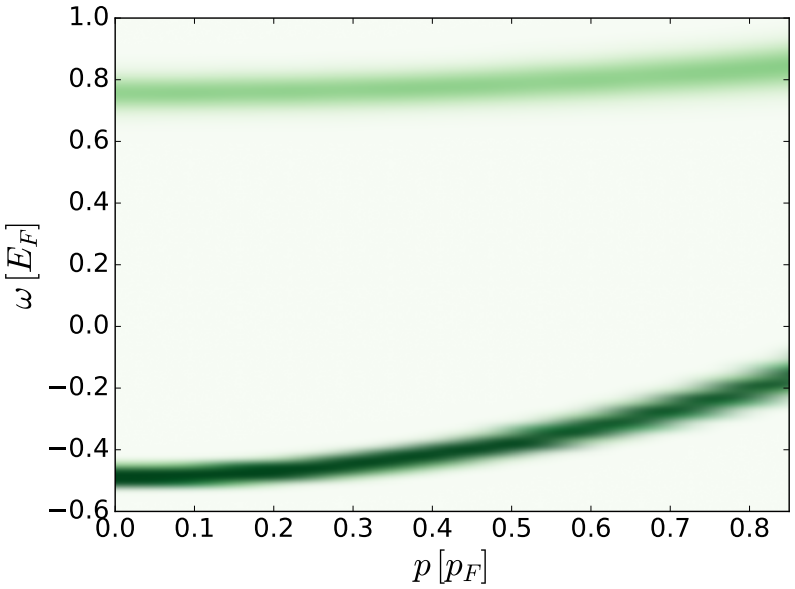

Figure 6.6.: The polaron spectral function is plotted for a mass-imbalance $r = 2$ at unitarity. Note the quadratic dispersion and the repulsive polaron at positive energies.

Part II.

Bosonic many-body physics: path integral Monte Carlo

7 Path integral Monte Carlo

This chapter gives a detailed derivation of the path integral Monte Carlo (PIMC) algorithm. PIMC allows to compute thermodynamic properties of Bose systems at finite temperature. In particular, energetic, structural, and superfluid properties can be computed without approximations.

Starting from Ceperley's original version, the worm algorithm with its crucial improvements for superfluid states is introduced. As program options, the fourth-order approximation and grand-canonical sampling are presented, as well as a cell scheme that reduces evaluations of the potential. The chapter is concluded by sections about observables and appropriate numerical tests.

For further details about PIMC, suggested references are a review by D. Ceperley [88], the original worm algorithm paper of Boninsegni, Prokof'ev and Svistunov [89] and the PhD thesis of S. Pilati [90]. Also consult the tutorial by A. del Maestro [91].

7.1. Original version of the path integral Monte Carlo algorithm

7.1.1. Periodic boundary conditions

As a preliminary step, the quantum mechanics of a one-dimensional particle of mass m in a box of length L with periodic boundary conditions are reviewed. This explains our conventions and is a crucial ingredient for the estimation of superfluid densities. The eigenstates $|p\rangle$ of the system are eigenstates of the momentum operator as there is no potential energy. This means that the wave function ψ of the system is a plane wave $\psi(x) = \mathcal{N}\langle x|p\rangle = \mathcal{N}e^{ipx}$ with wave number p and a normalization constant $\mathcal{N}$. The periodic boundary conditions demand that $\psi(x + L) = \psi(x)$. This restricts the possible values of p to $p = 2\pi n/L$ with integer n. Furthermore, by $\int_0^L \mathrm{d}x\ \psi(x)\psi^*(x) = 1$, we find $\mathcal{N} = \sqrt{1/L}$.

Next, we introduce a technical identity that will be used later (ϵ can be treated as a dummy parameter here):

$$\frac{1}{L}\sum_p e^{-ip(x-x')}e^{-\frac{\epsilon}{2m}p^2} = \frac{1}{L}\sum_{n=-\infty}^{\infty} e^{-i\frac{2\pi n}{L}(x-x')}e^{-\frac{\epsilon}{2m}\left(\frac{2\pi n}{L}\right)^2} \equiv \frac{1}{L}\sum_{n=-\infty}^{\infty} g(n). \tag{7.1}$$

Now we make use of the Poisson summation formula [4] which states that

$$\sum_{n=-\infty}^{\infty} g(n) = \sum_{w=-\infty}^{\infty}\left(\int \mathrm{d}\phi\ g(\phi)e^{i2\pi w\phi}\right). \tag{7.2}$$

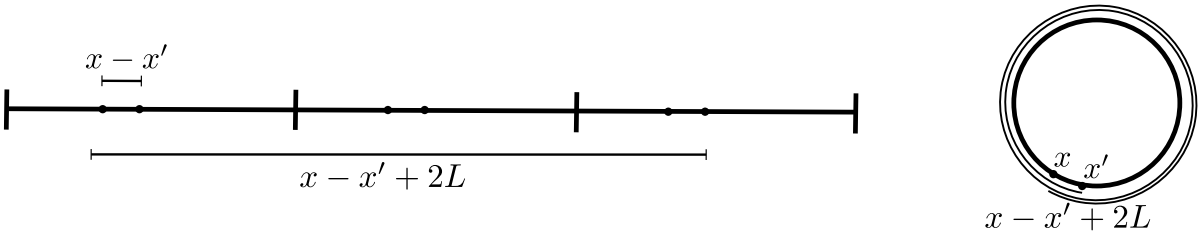

Figure 7.1.: In the left panel, a representation of periodic boundary conditions with repeated images is shown. The right panel shows the same system represented as a ring geometry.

This yields

$$\begin{aligned}\frac{1}{L}\sum_p e^{-ip(x-x')}e^{-\frac{\epsilon}{2m}p^2} &= \frac{1}{L}\sum_{w=-\infty}^{\infty}\left(\int \mathrm{d}\phi\; e^{-\frac{\epsilon}{2m}\left(\frac{2\pi\phi}{L}\right)^2} e^{-i\frac{2\pi\phi}{L}(x-x')} e^{i2\pi w\phi}\right) \\ &= \frac{1}{L}\sum_{w=-\infty}^{\infty}\left(\int \mathrm{d}\phi\; e^{-\frac{2\epsilon\pi^2}{mL^2}\phi^2} e^{i2\pi\left(w-\frac{x-x'}{L}\right)\phi}\right) \\ &= \sqrt{\frac{m}{2\epsilon\pi}}\sum_{w=-\infty}^{\infty} e^{-\frac{m}{2\epsilon}(x-x'+wL)^2}.\end{aligned} \tag{7.3}$$

These results can be easily translated to higher dimensions as the exponential functions factorize. In the context of PIMC, w is usually denoted winding number. This can be understood by looking at the terms of the sum: Their only difference is that the distance between x and x' is measured with respect to different periodic images, yielding integer multiples of the system length L. If these distance measurements are viewed from a representation of the periodic system as a two-dimensional circle, the name winding number becomes clear. This is illustrated in Fig. 7.1.

7.1.2. Basic decomposition of the partition function

Suppose that N distinguishable bosons of mass m are confined to a simulation box of volume V with periodic boundary conditions in d dimensions. This system is described by a Hamiltonian of the form

$$\hat{H} = \hat{T} + \hat{V}, \tag{7.4}$$

where we assume that the kinetic energy $\hat{T}$ and the potential energy $\hat{V}$ are diagonal in momentum and position space, respectively. The standard kinetic energy $\hat{T} = \sum_{i=1}^{N} \frac{\hat{\boldsymbol{p}}_i^2}{2m}$ is used and the system is at finite temperature T. This defines an inverse temperature $\beta = 1/k_B T$, where k_B is the Boltzmann constant which is set to 1. The canonical partition function Z of a many-body system of N distinguishable particles is given by

$$Z = \mathrm{tr}(e^{-\beta\hat{H}}) = \int \mathrm{d}\boldsymbol{R}\langle\boldsymbol{R}|e^{-\beta\hat{H}}|\boldsymbol{R}\rangle, \tag{7.5}$$

where $|\boldsymbol{R}\rangle$ is the normalized position basis $|\boldsymbol{r}_1\boldsymbol{r}_2...\boldsymbol{r}_N\rangle$ of the N-particle system with particle 1 being in single-particle position state $|\boldsymbol{r}_1\rangle$, particle 2 being in single-particle position state $|\boldsymbol{r}_2\rangle$ and so on. $\int \mathrm{d}\boldsymbol{R}$ is a shorthand notation for $\int \mathrm{d}\boldsymbol{r}_1\, \mathrm{d}\boldsymbol{r}_2 \ldots \mathrm{d}\boldsymbol{r}_N$. In a general quantum system, it is not possible to diagonalize $\hat{T}$ and $\hat{V}$ simultaneously, since $[\hat{T}, \hat{V}] \neq 0$. Therefore, it would be beneficial to split the exponential $e^{-\beta\hat{H}} = e^{-\beta(\hat{T}+\hat{V})}$ into two exponentials. With the help of the

Baker-Campbell-Hausdorff formula, the order of the error of a naive splitting can be shown to be $\mathcal{O}(\beta^2)$ for this case. This is plausible: For high temperatures, quantum effects are negligible and the exponential splitting is exact. A high-temperature expression can therefore be constructed by a trivial rewriting $e^{-\beta\hat{H}} = e^{-\frac{\beta}{2}\hat{H}} e^{-\frac{\beta}{2}\hat{H}}$ as the Hamiltonian commutes with itself. Repeating this step M times yields $e^{-\beta\hat{H}} = \prod_{t=0}^{M-1} e^{-\frac{\beta}{M}\hat{H}}$. If M is sufficiently large, one can hope to split the remaining exponential functions (which have an effective inverse temperature β/M) naively without suffering from a big systematic error. As this partition of the interval $[0, \beta]$ into M slices of length $\epsilon = \beta/M$ resembles the finite-temperature Green's functions technique [68], M is called number of timeslices, with reference to imaginary time (which we will denote by τ).

In the following, a complete basis of many-body states is inserted between these timeslices:

$$Z = \int \mathrm{d}\boldsymbol{R}\, \mathrm{d}\boldsymbol{R}_1\, \mathrm{d}\boldsymbol{R}_2 \ldots \mathrm{d}\boldsymbol{R}_{M-1} \langle \boldsymbol{R}|e^{-\epsilon\hat{H}}|\boldsymbol{R}_1\rangle\langle \boldsymbol{R}_1|e^{-\epsilon\hat{H}}|\boldsymbol{R}_2\rangle \ldots \langle \boldsymbol{R}_{M-1}|e^{-\epsilon\hat{H}}|\boldsymbol{R}\rangle. \tag{7.6}$$

Taking a single matrix element yields

$$\begin{aligned} \langle \boldsymbol{R}_{i-1}|e^{-\epsilon(\hat{T}+\hat{V})}|\boldsymbol{R}_i\rangle &= \langle \boldsymbol{R}_{i-1}|e^{-\epsilon\hat{T}} e^{-\epsilon\hat{V}}|\boldsymbol{R}_i\rangle + \mathcal{O}(\epsilon^2) = \\ &= \langle \boldsymbol{R}_{i-1}|e^{-\epsilon\hat{T}}|\boldsymbol{R}_i\rangle e^{-\epsilon V(\boldsymbol{R}_i)} + \mathcal{O}(\epsilon^2). \end{aligned} \tag{7.7}$$

Now we tackle the remaining matrix element by inserting a momentum basis $|\boldsymbol{P}\rangle$ of N distinguishable particles:

$$\begin{aligned} \rho(\boldsymbol{R}_{i-1}, \boldsymbol{R}_i, \epsilon) \equiv \langle \boldsymbol{R}_{i-1}|e^{-\epsilon\hat{T}}|\boldsymbol{R}_i\rangle &= \\ &= \frac{1}{V^{2N}} \sum_{\boldsymbol{P}_1, \boldsymbol{P}_2} \langle \boldsymbol{R}_{i-1}|\boldsymbol{P}_1\rangle\langle \boldsymbol{P}_1|e^{-\epsilon\hat{T}}|\boldsymbol{P}_2\rangle\langle \boldsymbol{P}_2|\boldsymbol{R}_i\rangle \\ &= \frac{1}{V^{2N}} \sum_{\boldsymbol{P}_1, \boldsymbol{P}_2} e^{i\boldsymbol{R}_{i-1}\boldsymbol{P}_1} \langle \boldsymbol{P}_1|e^{-\epsilon\hat{T}}|\boldsymbol{P}_2\rangle e^{-i\boldsymbol{P}_2\boldsymbol{R}_i} \\ &= \frac{1}{V^{2N}} \sum_{\boldsymbol{P}_1, \boldsymbol{P}_2} e^{i\boldsymbol{R}_{i-1}\boldsymbol{P}_1} V \delta_{\boldsymbol{P}_1, \boldsymbol{P}_2} e^{-\epsilon T(\boldsymbol{P}_1)} e^{-i\boldsymbol{P}_2\boldsymbol{R}_i} \\ &= \frac{1}{V^N} \sum_{\boldsymbol{P}} e^{-i\boldsymbol{P}(\boldsymbol{R}_i - \boldsymbol{R}_{i-1})} e^{-\epsilon\frac{\boldsymbol{P}^2}{2m}} \\ &= \left(\frac{m}{2\pi\epsilon}\right)^{\frac{Nd}{2}} \sum_{\boldsymbol{W}} \exp\left(-\frac{m(\boldsymbol{R}_i - \boldsymbol{R}_{i-1} + \boldsymbol{W})^2}{2\epsilon}\right), \end{aligned} \tag{7.8}$$

where in the last step, we used a generalized form of Eq. (7.3) and $\boldsymbol{R}$ and $\boldsymbol{P}$ are the (Nd)-dimensional composite vectors of all N particles. $\sum_{\boldsymbol{W}}$ is an abbreviation for $\sum_{w_1^1, w_1^2, \ldots, w_N^d = -\infty}^{\infty}$, where w_i^j labels the winding number of particle i in direction j. Here, W is the (Nd)-dimensional composite winding vector $(w_1^1 L_1, w_1^2 L_2, \ldots, w_N^d L_d)$ and L_j is the linear dimension of the simulation box in direction j. To simplify notation, we will omit the winding number from now on. Each matrix element $\rho(\boldsymbol{R}_{i-1}, \boldsymbol{R}_i, \epsilon)$ is implicitly understood to link the positions $\boldsymbol{R}_{i-1}$ and $\boldsymbol{R}_i$ either directly or by using the periodic boundary conditions arbitrarily often, generating a winding around the box.

Plugging this result back into the expression for the partition function yields

$$\begin{aligned} Z = &\int \mathrm{d}\boldsymbol{R}\, \mathrm{d}\boldsymbol{R}_1\, \mathrm{d}\boldsymbol{R}_2 \ldots \mathrm{d}\boldsymbol{R}_{M-1}\ \rho(\boldsymbol{R}, \boldsymbol{R}_1, \epsilon) e^{-\epsilon V(\boldsymbol{R}_1)} \rho(\boldsymbol{R}_1, \boldsymbol{R}_2, \epsilon) e^{-\epsilon V(\boldsymbol{R}_2)} \\ &\ldots \rho(\boldsymbol{R}_{M-2}, \boldsymbol{R}_{M-1}, \epsilon) e^{-\epsilon V(\boldsymbol{R}_{M-1})} \rho(\boldsymbol{R}_{M-1}, \boldsymbol{R}, \epsilon) e^{-\epsilon V(\boldsymbol{R})} + \mathcal{O}(\epsilon) \\ = &\int \mathrm{d}\boldsymbol{R}_0\, \mathrm{d}\boldsymbol{R}_1\, \mathrm{d}\boldsymbol{R}_2 \ldots \mathrm{d}\boldsymbol{R}_{M-1}\ \rho(\boldsymbol{R}_0, \boldsymbol{R}_1, \epsilon) e^{-\epsilon V(\boldsymbol{R}_1)} \rho(\boldsymbol{R}_1, \boldsymbol{R}_2, \epsilon) e^{-\epsilon V(\boldsymbol{R}_2)} \end{aligned} \tag{7.9}$$

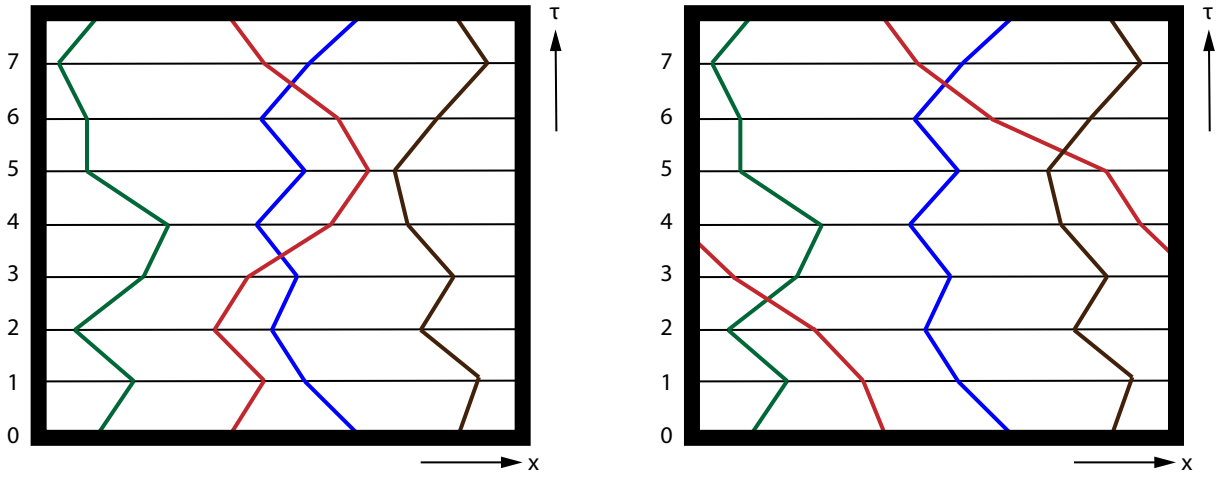

Figure 7.2.: Typical worldline configurations for $M = 8$ and $N = 4$. For simplicity, only one spatial dimension is shown. Note that all particle worldlines close on their initial position at $\tau = M$. In the right panel, the red particle worldline uses the periodic boundary conditions between timeslices three and four.

$$\begin{aligned} &\dots \rho(\boldsymbol{R}_{M-2}, \boldsymbol{R}_{M-1}, \epsilon) e^{-\epsilon V(\boldsymbol{R}_{M-1})} \rho(\boldsymbol{R}_{M-1}, \boldsymbol{R}_0, \epsilon) e^{-\epsilon V(\boldsymbol{R}_0)} + \mathcal{O}(\epsilon) \\ &= \left(\prod_{t=0}^{M-1} \int \mathrm{d}\boldsymbol{R}_t \right) \left(\prod_{t=0}^{M-1} \rho(\boldsymbol{R}_t, \boldsymbol{R}_{t+1}, \epsilon) e^{-\epsilon V(\boldsymbol{R}_t)} \right) + \mathcal{O}(\epsilon). \end{aligned}$$

In the last steps, $\boldsymbol{R}$ was relabeled to $\boldsymbol{R}_0$ to make the symmetry of this expression obvious and the identification $\boldsymbol{R}_M = \boldsymbol{R}_0$ was used. Note that the total error of the partition function is of order ϵ because the approximation error is made once per timeslice[1].

If the partition function is rewritten according to Eq. (7.9), it is accessible by numerical evaluation: The Monte Carlo method is ideal for multi-dimensional integrals. Note that this mapping is exact for $M \to \infty$ or $\epsilon \to 0$. In summary, a (Nd)-dimensional quantum problem is mapped onto a $(Nd+1)$-dimensional classical problem: The extra dimension is given by the additional imaginary time axis. It is useful to visualize the configurations as particle worldlines, shown in Fig. 7.2. This representation is straightforward by attributing all integration variables to x-τ points. In this picture, the intersections of the worldlines with the timeslices are denominated 'beads'. By analyzing the dependence of the kinetic term on temperature, it becomes clear that low temperatures allow bigger position displacements between adjacent beads, while high temperatures render the worldlines essentially straight, suppressing quantum fluctuations. As the imaginary time axis is trivial in this limit, it drops out of the sampling and the connection to a classical Markov-chain Monte Carlo simulation of particles in a box is found.

7.1.3. Indistinguishable particles

In the next step, the bosonic particle statistics have to be incorporated into the algorithm. This can be done by symmetrizing the many-particle basis $\boldsymbol{\mathcal{R}}$ under particle exchanges:

$$|\boldsymbol{\mathcal{R}}\rangle = \frac{1}{N!} \sum_{\mathcal{P}} |\boldsymbol{r}_{\mathcal{P}(1)} \boldsymbol{r}_{\mathcal{P}(2)} \dots \boldsymbol{r}_{\mathcal{P}(N)}\rangle, \tag{7.10}$$

where the sum runs over all particle permutations $\mathcal{P}$.

[1] Briefly speaking, a consequence of the Binomial theorem is that $[1 + \mathcal{O}(\epsilon^2)]^M = 1 + \mathcal{O}(\epsilon)$.

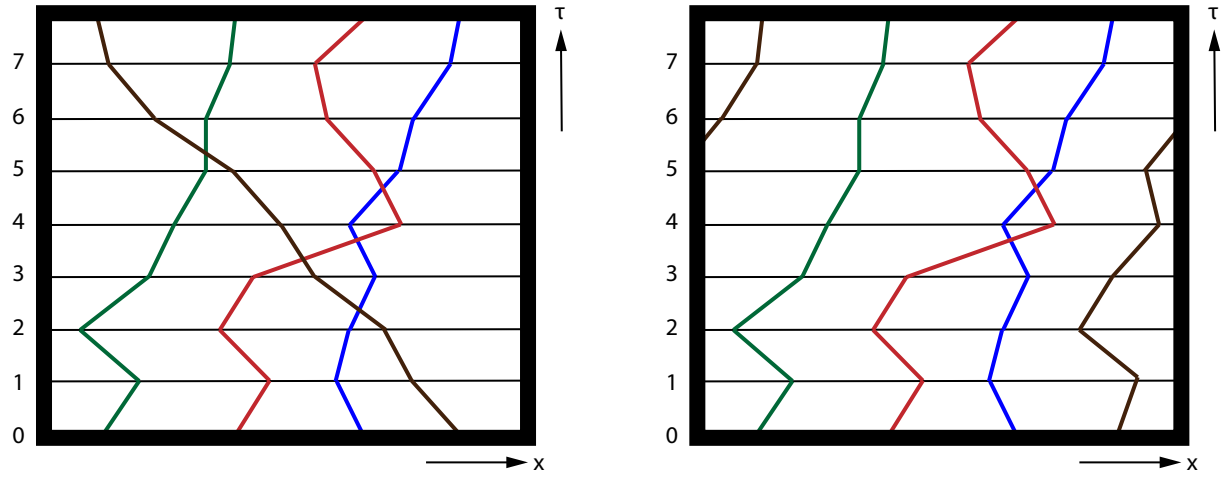

Figure 7.3.: Typical worldline configurations with particle exchanges are illustrated for $M = 8$ and $N = 4$. In the right configuration, the brown particle worldline uses the periodic boundary conditions between timeslices five and six.

Introducing these states into the decomposition of the partition function has the effect of admitting new configurations: Restricting our analysis to the many-particle states $\boldsymbol{\mathcal{R}}_0$ in $Z = \int \mathrm{d}\boldsymbol{R}_0 \langle \boldsymbol{\mathcal{R}}_0 | e^{-\beta \hat{H}} | \boldsymbol{\mathcal{R}}_0 \rangle$ and expanding both $\boldsymbol{\mathcal{R}}_0$ by Eq. (7.10) has the effect of splitting this single term into $(N!)^2$ terms:

$$Z = \frac{1}{(N!)^2} \int \mathrm{d}\boldsymbol{r}_1 \, \mathrm{d}\boldsymbol{r}_2 \ldots \boldsymbol{r}_N \sum_{\mathcal{P}_1, \mathcal{P}_2} \langle \boldsymbol{r}_{\mathcal{P}_1(1)} \boldsymbol{r}_{\mathcal{P}_1(2)} \ldots \boldsymbol{r}_{\mathcal{P}_1(N)} | e^{-\beta \hat{H}} | \boldsymbol{r}_{\mathcal{P}_2(1)} \boldsymbol{r}_{\mathcal{P}_2(2)} \ldots \boldsymbol{r}_{\mathcal{P}_2(N)} \rangle. \quad (7.11)$$

In the worldline picture, this means that worldlines are now permitted to close on one another. An example for these states is shown in Fig. 7.3.

Permutating on both sides of this expression is not strictly necessary because the system is invariant upon a relabeling of all particles in the integral:

$$\begin{aligned} \sum_{\mathcal{P}_1} \int \mathrm{d}\boldsymbol{r}_1 \, \mathrm{d}\boldsymbol{r}_2 \ldots \boldsymbol{r}_N \langle \boldsymbol{r}_{\mathcal{P}_1(1)} \boldsymbol{r}_{\mathcal{P}_1(2)} \ldots \boldsymbol{r}_{\mathcal{P}_1(N)} | &= \sum_{\mathcal{P}_1} \int \mathrm{d}\boldsymbol{r}'_1 \, \mathrm{d}\boldsymbol{r}'_2 \ldots \boldsymbol{r}'_N \langle \boldsymbol{r}'_1 \boldsymbol{r}'_2 \ldots \boldsymbol{r}'_N | \quad (7.12) \\ &= N! \int \mathrm{d}\boldsymbol{r}_1 \, \mathrm{d}\boldsymbol{r}_2 \ldots \boldsymbol{r}_N \langle \boldsymbol{r}_1 \boldsymbol{r}_2 \ldots \boldsymbol{r}_N |. \end{aligned}$$

Therefore, the partition function is

$$\frac{1}{N!} \int \mathrm{d}\boldsymbol{r}_1 \, \mathrm{d}\boldsymbol{r}_2 \ldots \boldsymbol{r}_N \sum_{\mathcal{P}} \langle \boldsymbol{r}_1 \boldsymbol{r}_2 \ldots \boldsymbol{r}_N | e^{-\beta \hat{H}} | \boldsymbol{r}_{\mathcal{P}(1)} \boldsymbol{r}_{\mathcal{P}(2)} \ldots \boldsymbol{r}_{\mathcal{P}(N)} \rangle. \quad (7.13)$$

Note that $\mathcal{P} \neq \mathcal{P}_2$ as the relabeling also affected the permutation on the right.

A very similar argument is valid for intermediate states that are inserted as a many-body basis. Again, the identity $\int \mathrm{d}\boldsymbol{R} |\boldsymbol{\mathcal{R}}\rangle\langle\boldsymbol{\mathcal{R}}|$ splits into $(N!)^2$ terms:

$$\frac{1}{(N!)^2} \int \mathrm{d}\boldsymbol{r}_1 \, \mathrm{d}\boldsymbol{r}_2 \ldots \boldsymbol{r}_N \sum_{\mathcal{P}_1, \mathcal{P}_2} |\boldsymbol{r}_{\mathcal{P}_1(1)} \boldsymbol{r}_{\mathcal{P}_1(2)} \ldots \boldsymbol{r}_{\mathcal{P}_1(N)} \rangle\langle \boldsymbol{r}_{\mathcal{P}_2(1)} \boldsymbol{r}_{\mathcal{P}_2(2)} \ldots \boldsymbol{r}_{\mathcal{P}_2(N)}|. \quad (7.14)$$

The permutation sum $\mathcal{P}_1$ can be eliminated by relabeling all particles in the integral. This cancels

one of the $\frac{1}{N!}$ factors, such that the identity becomes

$$\frac{1}{N!}\int \mathrm{d}\boldsymbol{r}_1\,\mathrm{d}\boldsymbol{r}_2\ldots\boldsymbol{r}_N\sum_{\mathcal{P}_2}|\boldsymbol{r}_{\mathcal{Q}(1)}\boldsymbol{r}_{\mathcal{Q}(2)}\ldots\boldsymbol{r}_{\mathcal{Q}(N)}\rangle\langle\boldsymbol{r}_{\mathcal{P}_2(1)}\boldsymbol{r}_{\mathcal{P}_2(2)}\ldots\boldsymbol{r}_{\mathcal{P}_2(N)}|, \tag{7.15}$$

where $\mathcal{Q}$ is an arbitrary permutation. If this is used for all intermediate states, the partition function can be expanded as

$$\begin{aligned}Z =&\frac{1}{N!}\int \mathrm{d}\boldsymbol{R}\,\mathrm{d}\boldsymbol{R}_1\,\mathrm{d}\boldsymbol{R}_2\ldots\mathrm{d}\boldsymbol{R}_{M-1}\sum_{\mathcal{P}}\frac{1}{(N!)^{M-1}}\sum_{\mathcal{P}_1,\mathcal{P}_2,\ldots,\mathcal{P}_{M-1}} \\ &\langle\boldsymbol{R}|e^{-\epsilon\hat{H}}|\boldsymbol{R}_1\rangle\langle\mathcal{P}_1\boldsymbol{R}_1|e^{-\epsilon\hat{H}}|\mathcal{P}_1\boldsymbol{R}_2\rangle\langle\mathcal{P}_2\boldsymbol{R}_2|e^{-\epsilon\hat{H}}|\mathcal{P}_2\boldsymbol{R}_3\rangle\ldots\langle\mathcal{P}_{M-1}\boldsymbol{R}_{M-1}|e^{-\epsilon\hat{H}}|\mathcal{P}\boldsymbol{R}\rangle,\end{aligned} \tag{7.16}$$

where $|\mathcal{P}\boldsymbol{R}\rangle \equiv |\boldsymbol{r}_{\mathcal{P}(1)}\boldsymbol{r}_{\mathcal{P}(2)}\ldots\boldsymbol{r}_{\mathcal{P}(N)}\rangle$. The derivation of the matrix elements of distinguishable particles showed that $\langle\mathcal{Q}\boldsymbol{R}_1|e^{-\epsilon\hat{H}}|\mathcal{Q}\boldsymbol{R}_2\rangle$ does not depend on the particular permutation $\mathcal{Q}$. This means that the identity permutation can be selected for each matrix element, which renders the permutation sums trivial:

$$\begin{aligned}Z =&\frac{1}{N!}\int \mathrm{d}\boldsymbol{R}\,\mathrm{d}\boldsymbol{R}_1\,\mathrm{d}\boldsymbol{R}_2\ldots\mathrm{d}\boldsymbol{R}_{M-1}\sum_{\mathcal{P}} \\ &\langle\boldsymbol{R}|e^{-\epsilon\hat{H}}|\boldsymbol{R}_1\rangle\langle\boldsymbol{R}_1|e^{-\epsilon\hat{H}}|\boldsymbol{R}_2\rangle\langle\boldsymbol{R}_2|e^{-\epsilon\hat{H}}|\boldsymbol{R}_3\rangle\ldots\langle\boldsymbol{R}_{M-1}|e^{-\epsilon\hat{H}}|\mathcal{P}\boldsymbol{R}\rangle.\end{aligned} \tag{7.17}$$

Note that it is not possible to eliminate the last permutation sum.

In summary, the expansion of the partition function now is

$$Z = \frac{1}{N!}\sum_{\mathcal{P}}\left(\prod_{t=0}^{M-1}\int \mathrm{d}\boldsymbol{R}_t\right)\left(\prod_{t=0}^{M-1}\rho(\boldsymbol{R}_t,\boldsymbol{R}_{t+1},\epsilon)e^{-\epsilon V(\boldsymbol{R}_t)}\right)+\mathcal{O}(\epsilon), \tag{7.18}$$

with $\boldsymbol{R}_M = \mathcal{P}(\boldsymbol{\mathcal{R}}_0)$ and $\mathcal{P}(\boldsymbol{R}) \equiv \mathcal{P}(\boldsymbol{r}_1,\boldsymbol{r}_2,\ldots,\boldsymbol{r}_N) \equiv (\boldsymbol{r}_{\mathcal{P}(1)},\boldsymbol{r}_{\mathcal{P}(2)},\ldots,\boldsymbol{r}_{\mathcal{P}(N)})$. This reformulation of the original problem holds for arbitrary inter-bosonic and external potentials and allows to compute observables with arbitrary precision by adjusting the number of timeslices.

Before the Monte Carlo updates for this configuration space are explained in detail, we establish the standard nomenclature of PIMC:

- **Timeslice**: One instant in imaginary time. Possible values: $\tau = 0,\epsilon,\ldots,(M-1)\epsilon$.
- **Worldline**: The collection of particles that are linked by kinetic matrix elements. No periodicity is taken into account, only the connection from timeslice 0 to timeslice $M-1$ matters.
- **Particle exchange**: If a worldline does not close on itself in imaginary time, the resulting configuration includes a particle exchange.
- **Bead**: One instant of a worldline in imaginary time.

7.1.4. Updates for distinguishable particles

An ergodic set of updates for PIMC consists of two types of updates: first, there are updates that modify the positions of the beads; second, there are updates which alter the topology of the configuration in order to include the correct bosonic particle permutations.

Conventionally, the latter was implemented by a *Swap* update that took two particle worldlines and exchanged parts of their trajectory so that crossed configurations were formed. The problem of this approach lies in the selection of the number of beads that are exchanged: one has to find

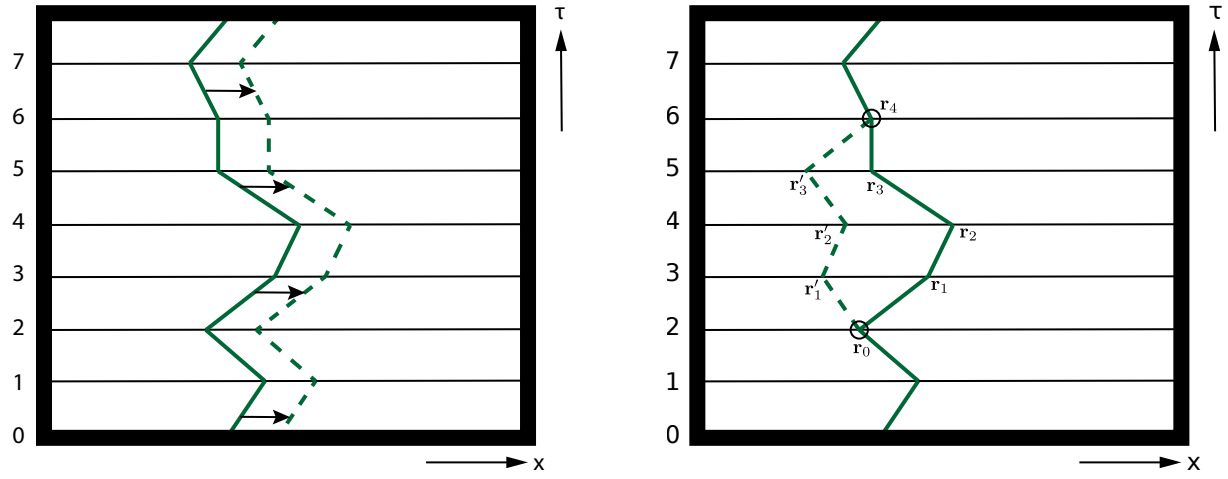

Figure 7.4.: Illustration of the updates *Rigid* (left) and *Diagonal* (right). For the *Diagonal* move, a value of $\bar{M} = 3$ was selected. The end points of the *Lévy construction* are marked by circles.

a compromise between swapping only two beads (which results in big kinks in the worldlines and has therefore low acceptance ratio) and swapping a large part of the trajectory (which results in a smoother path but suffers in acceptance because intermediate positions might be occupied by other particles which usually form a potential energy barrier).

As this problem can be overcome by the worm algorithm described in Sec. 7.2, the *Swap* update is not explained here. We restrict ourselves to the two diagonal updates that modify the bead positions: *Rigid* and *Diagonal*.

A word about all updates described in this text: To keep the notation clean, the update descriptions do not include special cases concerning the periodicity of the worldlines in imaginary time or real space. This means that we assume that an update that accesses the worldlines $\tau = (M\epsilon, M\epsilon + \epsilon, \dots)$ is silently translating this to $\tau = (0, \epsilon, \dots)$.

Rigid This update selects a single worldline (which is not part of a bosonic particle exchange) and generates a displacement vector $\boldsymbol{\delta}$ uniformly in some interval $[-\delta_{\max}, \delta_{\max}]^d$ where $\delta_{\max}$ is a parameter of the simulation that can be used to tune the acceptance ratio of *Rigid*. Optimally, it produces neither vanishing acceptance nor artificially tiny displacements. After seeding $\boldsymbol{\delta}$, the Metropolis ratio P_{RI} is formed by proposing to displace the whole particle worldline by $\boldsymbol{\delta}$. As this does not change the kinetic energy, only the new potential energy has to be taken into account:

$$P_{\mathrm{RI}} = \min\left(1, \prod_{t=0}^{M-1} \frac{e^{-\epsilon V(\boldsymbol{r}_1^t \boldsymbol{r}_2^t \dots (\boldsymbol{r}_i^t + \boldsymbol{\delta}) \dots \boldsymbol{r}_N^t)}}{e^{-\epsilon V(\boldsymbol{r}_1^t \boldsymbol{r}_2^t \dots \boldsymbol{r}_i^t \dots \boldsymbol{r}_N^t)}}\right). \tag{7.19}$$

In this expression, the particle worldlines are named according to some arbitrary convention to numbers between 1 and N. The worldline i is assumed to be selected by *Rigid*. $\boldsymbol{r}_{i'}^j$ labels the position of worldline i' at timeslice j. The whole process is illustrated in Fig. 7.4.

The *Rigid* update is essentially a classical Monte Carlo update as it does not make any reference to imaginary time. Another update is needed to be ergodic with respect to particle positions.

Diagonal The *Diagonal* update takes a part of a particle worldline and resamples it by a technique called *Lévy construction* [92]. Suppose that a random bead of worldline i is selected at timeslice j. Next, an integer $\bar{M}$ is drawn uniformly from an interval $[1, \bar{M}_{\mathrm{diag}}]$. Here, $\bar{M}_{\mathrm{diag}}$ is a simulation parameter which should be reasonably smaller than M. Advancing from the selected

bead in positive imaginary time direction yields a path with coordinates $\boldsymbol{r}_1, \boldsymbol{r}_2, \ldots, \boldsymbol{r}_{\bar{M}}$ – those coordinates will be modified. Here, $\boldsymbol{r}_1 = \boldsymbol{r}_i^j, \boldsymbol{r}_2 = \boldsymbol{r}_i^{j+1}, \ldots, \boldsymbol{r}_{\bar{M}} = \boldsymbol{r}_i^{j+\bar{M}}$. If the (fixed) beads that enclose this path are called $\boldsymbol{r}_0$ and $\boldsymbol{r}_{M+1}$, the complete information for the update is given by the list $\boldsymbol{r}_0, \boldsymbol{r}_1, \ldots \boldsymbol{r}_{\bar{M}}, \boldsymbol{r}_{\bar{M}+1}$.

In contrast to *Rigid*, the kinetic energy of the configuration will not stay the same for *Diagonal*. Therefore, it becomes necessary to include ρ-factors of the configurational weight into the calculation which present additional difficulties. For example, a naive version of the algorithm, consisting in a displacement of a single bead by some arbitrary vector, is not suitable for efficient sampling, because the kinetic factors usually attach the bead to its two neighbors on adjacent timeslices. Hence, the simulation tends to get stuck in a subset of configurational space.

The *Lévy construction* solves this problem. It uses the fact that ρ is of Gaussian shape in order to optimize the acceptance ratio. The construction works as follows:

1. Take the current starting point $\boldsymbol{r'}_t$ (initially: $\boldsymbol{r'}_{t=0} = \boldsymbol{r}_0$) and interpolate linearly on the shortest possible path between $\boldsymbol{r'}_t$ and $\boldsymbol{r}_{\bar{M}+1}$. For the timeslice $t+1$, this yields an intermediate point $\bar{\boldsymbol{r}}'_{t+1} = \boldsymbol{r'}_t + (\boldsymbol{r}_{\bar{M}+1} - \boldsymbol{r'}_t) \cdot (\bar{M} + 1 - t)^{-1}$.

2. Define $\sigma_t^2 = \frac{\epsilon(\bar{M}-t)}{m(\bar{M}-t+1)}$ and draw a random number $\boldsymbol{r'}_{t+1}$ from a normal distribution with $\mu = \bar{\boldsymbol{r}}'$ and variance σ_t^2.

3. Set $\boldsymbol{r'}_{t+1}$ as new starting point and start over. Repeat this procedure until a whole path $\boldsymbol{r'}_1 \ldots \boldsymbol{r'}_{\bar{M}}$ is generated.

4. Accept the new path with probability $\min\left(1, \prod_{t=j}^{j+\bar{M}} e^{-\epsilon[V(\boldsymbol{R'}_t) - V(\boldsymbol{R}_t)]}\right)$. $\boldsymbol{R}_t$ and $\boldsymbol{R'}_t$ are abbreviations for $(\boldsymbol{r}_1^t, \boldsymbol{r}_2^t, \ldots, \boldsymbol{r}_i^t, \ldots, \boldsymbol{r}_N^t)$ and $(\boldsymbol{r}_1^t, \boldsymbol{r}_2^t, \ldots, \boldsymbol{r'}_i^t, \ldots, \boldsymbol{r}_N^t)$

The reason why this works can be understood by analyzing the kinetic weight of the old and the new configuration. This kinetic weight of a configuration $\boldsymbol{r}_1 \ldots \boldsymbol{r}_{\bar{M}}$ is given by

$$\mathrm{d}\boldsymbol{r}_1 \ldots \mathrm{d}\boldsymbol{r}_{\bar{M}}\ \rho(\boldsymbol{r}_0, \boldsymbol{r}_1, \epsilon)\rho(\boldsymbol{r}_1, \boldsymbol{r}_2, \epsilon) \ldots \rho(\boldsymbol{r}_{\bar{M}}, \boldsymbol{r}_{\bar{M}+1}, \epsilon). \tag{7.20}$$

Ideally, this weight should be canceled by a suitable *a priori* probability $\mathcal{A}$. If the particle positions are drawn from Eq. (7.20), it has to be normalized accordingly, i.e.,

$$\mathcal{A}(\boldsymbol{r}_1 \ldots \boldsymbol{r}_{\bar{M}}) = \frac{\mathrm{d}\boldsymbol{r}_1 \ldots \mathrm{d}\boldsymbol{r}_{\bar{M}}\ \rho(\boldsymbol{r}_0, \boldsymbol{r}_1, \epsilon)\rho(\boldsymbol{r}_1, \boldsymbol{r}_2, \epsilon) \ldots \rho(\boldsymbol{r}_{\bar{M}}, \boldsymbol{r}_{\bar{M}+1}, \epsilon)}{\int \mathrm{d}\boldsymbol{x}_1 \ldots \mathrm{d}\boldsymbol{x}_{\bar{M}}\ \rho(\boldsymbol{r}_0, \boldsymbol{x}_1, \epsilon)\rho(\boldsymbol{x}_1, \boldsymbol{x}_2, \epsilon) \ldots \rho(\boldsymbol{x}_{\bar{M}}, \boldsymbol{r}_{\bar{M}+1}, \epsilon)}. \tag{7.21}$$

As can be easily proven, ρ is subject to the convolution property

$$\rho(\boldsymbol{r}_i, \boldsymbol{r}_j, 2\epsilon) = \int \mathrm{d}\boldsymbol{r}_k\ \rho(\boldsymbol{r}_i, \boldsymbol{r}_k, \epsilon)\rho(\boldsymbol{r}_k, \boldsymbol{r}_j, \epsilon). \tag{7.22}$$

If this expression is used repeatedly, the denominator of Eq. (7.21) can be rewritten:

$$\mathcal{A}(\boldsymbol{r}_1 \ldots \boldsymbol{r}_{\bar{M}}) = \frac{\mathrm{d}\boldsymbol{r}_1 \ldots \mathrm{d}\boldsymbol{r}_{\bar{M}}\ \rho(\boldsymbol{r}_0, \boldsymbol{r}_1, \epsilon)\rho(\boldsymbol{r}_1, \boldsymbol{r}_2, \epsilon) \ldots \rho(\boldsymbol{r}_{\bar{M}}, \boldsymbol{r}_{\bar{M}+1}, \epsilon)}{\rho(\boldsymbol{r}_0, \boldsymbol{r}_{\bar{M}+1}, \bar{M}\epsilon + \epsilon)}. \tag{7.23}$$

Now, several identities are inserted in the form $\rho(\boldsymbol{r}_1, \boldsymbol{r}_{\bar{M}+1}, \bar{M}\epsilon)/\rho(\boldsymbol{r}_1, \boldsymbol{r}_{\bar{M}+1}, \bar{M}\epsilon) = 1$:

$$\begin{aligned} \mathcal{A}(\boldsymbol{r}_1 \ldots \boldsymbol{r}_{\bar{M}}) = & \frac{\mathrm{d}\boldsymbol{r}_1\ \rho(\boldsymbol{r}_0, \boldsymbol{r}_1, \epsilon)\rho(\boldsymbol{r}_1, \boldsymbol{r}_{\bar{M}+1}, \bar{M}\epsilon)}{\rho(\boldsymbol{r}_0, \boldsymbol{r}_{\bar{M}+1}, \bar{M}\epsilon + \epsilon)} \\ & \times \frac{\mathrm{d}\boldsymbol{r}_2\ \rho(\boldsymbol{r}_1, \boldsymbol{r}_2, \epsilon)\rho(\boldsymbol{r}_2, \boldsymbol{r}_{\bar{M}+1}, \bar{M}\epsilon - \epsilon)}{\rho(\boldsymbol{r}_1, \boldsymbol{r}_{\bar{M}+1}, \bar{M}\epsilon)} \times \ldots \end{aligned} \tag{7.24}$$

$$\times \frac{\mathrm{d}\boldsymbol{r}_{\bar{M}}\ \rho(\boldsymbol{r}_{\bar{M}-1}, \boldsymbol{r}_{\bar{M}}, \epsilon)\rho(\boldsymbol{r}_{\bar{M}}, \boldsymbol{r}_{\bar{M}+1}, \epsilon)}{\rho(\boldsymbol{r}_{\bar{M}-1}, \boldsymbol{r}_{\bar{M}+1}, 2\epsilon)}.$$

In this expression, the first term does not depend on $\boldsymbol{r}_2 \dots \boldsymbol{r}_{\bar{M}}$, the second term does not depend on $\boldsymbol{r}_3 \dots \boldsymbol{r}_{\bar{M}}$ and so on. This allows the seeding of $\boldsymbol{r}_1$ according to the first term; afterwards, $\boldsymbol{r}_2$ can be seeded from the second term with the help of the already fixed $\boldsymbol{r}_1$. In this way, a whole set of intermediate particle positions is subsequently generated. Looking at the first term more closely and remembering the convolution identity of Eq. (7.22), one notices that the denominator is just the normalization of the numerator. Finally, this numerator is examined:

$$\begin{aligned} \rho(\boldsymbol{r}_0, \boldsymbol{r}_1, \epsilon)\rho(\boldsymbol{r}_1, \boldsymbol{r}_{\bar{M}+1}, \bar{M}\epsilon) &\propto e^{-\frac{m}{2\epsilon}(\boldsymbol{r}_0 - \boldsymbol{r}_1)^2} e^{-\frac{m}{2\bar{M}\epsilon}(\boldsymbol{r}_1 - \boldsymbol{r}_{\bar{M}+1})^2} \\ &\propto e^{-\frac{m}{2\epsilon}[(1+\frac{1}{\bar{M}})\boldsymbol{r}_1^2 + 2(\boldsymbol{r}_0 + \frac{1}{\bar{M}}\boldsymbol{r}_{\bar{M}+1})\boldsymbol{r}_1]} \\ &\propto e^{-(\boldsymbol{r}_1 - \bar{\boldsymbol{r}}'_1)^2/2\sigma_1^2}. \end{aligned} \tag{7.25}$$

In the first step, the normalization factors of the exponentials were dropped. In the second step, all multiplicative terms which did not depend on $\boldsymbol{r}_1$ were omitted (remember that the denominator takes care of the norm, so these terms do not matter for the functional dependence on $\boldsymbol{r}_1$). In the last step, the completing of the square changed the expression once again by a constant factor. As before, $\sigma_1^2 = \frac{\epsilon\bar{M}}{m(\bar{M}+1)}$ and $\bar{\boldsymbol{r}}'_1 = \boldsymbol{r}'_0 + (\boldsymbol{r}_{\bar{M}+1} - \boldsymbol{r}'_0)/\bar{M}$.

In summary, if $\boldsymbol{r}'_1$ is seeded according to a normal distribution with mean $\bar{\boldsymbol{r}}'_1$ and variance σ_1^2, one generates particle positions according to the distribution (7.23). The numerator of this *a priori* probability exactly cancels the corresponding weight factor of the Metropolis ratio. As the denominator only depends on the endpoints, it is the same for the *a priori* probabilities of forward and backward updates and drops out.

This means that direct sampling is established for the kinetic energy of the intermediate positions. Regarding the potential terms, a simple comparison between the weights of new and old configuration is inserted into the Metropolis ratio.

We elaborate on this ratio by giving the detailed weights and *a priori* probabilities; if the original configuration is denoted by x and the new one by x', the relevant configuration weights are given by

$$\begin{aligned} W(x) &= \mathrm{d}\boldsymbol{r}_1 \dots \mathrm{d}\boldsymbol{r}_{\bar{M}}\ \rho(\boldsymbol{r}_0, \boldsymbol{r}_1, \epsilon)\rho(\boldsymbol{r}_1, \boldsymbol{r}_2, \epsilon) \dots \rho(\boldsymbol{r}_{\bar{M}}, \boldsymbol{r}_{\bar{M}+1}, \epsilon) \prod_{t=j}^{j+\bar{M}} e^{-\epsilon V(\boldsymbol{R}_t)} \\ W(x') &= \mathrm{d}\boldsymbol{r}'_1 \dots \mathrm{d}\boldsymbol{r}'_{\bar{M}}\ \rho(\boldsymbol{r}_0, \boldsymbol{r}'_1, \epsilon)\rho(\boldsymbol{r}'_1, \boldsymbol{r}'_2, \epsilon) \dots \rho(\boldsymbol{r}'_{\bar{M}}, \boldsymbol{r}_{\bar{M}+1}, \epsilon) \prod_{t=j}^{j+\bar{M}} e^{-\epsilon V(\boldsymbol{R}'_t)}. \end{aligned} \tag{7.26}$$

The corresponding *a priori* probabilities are

$$\begin{aligned} \mathcal{A}(x \to x') = \mathcal{A}(\boldsymbol{r}'_1 \dots \boldsymbol{r}'_{\bar{M}}) &= \frac{\mathrm{d}\boldsymbol{r}'_1 \dots \mathrm{d}\boldsymbol{r}'_{\bar{M}}\ \rho(\boldsymbol{r}_0, \boldsymbol{r}'_1, \epsilon)\rho(\boldsymbol{r}'_1, \boldsymbol{r}'_2, \epsilon) \dots \rho(\boldsymbol{r}'_{\bar{M}}, \boldsymbol{r}_{\bar{M}+1}, \epsilon)}{\int \mathrm{d}\boldsymbol{x}_1 \dots \mathrm{d}\boldsymbol{x}_{\bar{M}}\ \rho(\boldsymbol{r}_0, \boldsymbol{x}_1, \epsilon)\rho(\boldsymbol{x}_1, \boldsymbol{x}_2, \epsilon) \dots \rho(\boldsymbol{x}_{\bar{M}}, \boldsymbol{r}_{\bar{M}+1}, \epsilon)} \\ \mathcal{A}(x' \to x) = \mathcal{A}(\boldsymbol{r}_1 \dots \boldsymbol{r}_{\bar{M}}) &= \frac{\mathrm{d}\boldsymbol{r}_1 \dots \mathrm{d}\boldsymbol{r}_{\bar{M}}\ \rho(\boldsymbol{r}_0, \boldsymbol{r}_1, \epsilon)\rho(\boldsymbol{r}_1, \boldsymbol{r}_2, \epsilon) \dots \rho(\boldsymbol{r}_{\bar{M}}, \boldsymbol{r}_{\bar{M}+1}, \epsilon)}{\int \mathrm{d}\boldsymbol{x}_1 \dots \mathrm{d}\boldsymbol{x}_{\bar{M}}\ \rho(\boldsymbol{r}_0, \boldsymbol{x}_1, \epsilon)\rho(\boldsymbol{x}_1, \boldsymbol{x}_2, \epsilon) \dots \rho(\boldsymbol{x}_{\bar{M}}, \boldsymbol{r}_{\bar{M}+1}, \epsilon)}. \end{aligned} \tag{7.27}$$

When periodic boundary conditions are used, several subtleties arise:

- Suppose that our system is in a cubic box with linear dimensions $[L_1, \dots, L_d]$. When the *Lévy construction* is used to resample parts of a worldline, there is a nonzero probability of generating new positions that are displaced from the preceding bead by distances longer than half of the corresponding linear dimension (as shown on the left hand side of

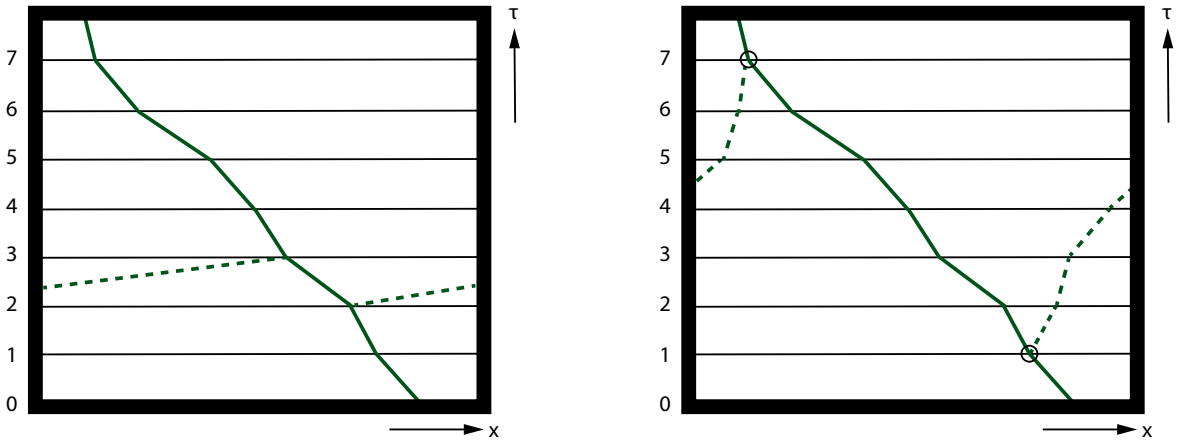

Figure 7.5.: Illustration of common sampling problems. The left picture shows a rare sampling event (dashed line). On the right, two paths are shown that belong to the same endpoints. As the dashed line is the shorter connection, the diagonal move is only possible for this path.

Fig. 7.5). As it is algorithmically beneficial to store particle positions and omit the saving of displacement vectors, this is a problem as the minimal distance between those beads would then point to a configuration different from the sampled one. The solution is to keep track of how often this issue occurs. If it is a rare event, the results will be correct despite detailed balance being broken from time to time. If the issue is happening more often, then the volume or the number of timeslices has to be adjusted. Increasing these quantities has the effect of decreasing the probability of large jumps.

- The *Lévy construction* only depends on the given endpoints and assumes that the sampled path follows the shortest connection between those points. However, configurations that follow longer trajectories between these points are part of the partition space and have to be sampled. If detailed balance shall not be broken, it is therefore necessary to include a check before every update using the *Lévy construction* if the current path is linking the endpoints in a direct manner. If this check fails, the update has to be rejected. Likewise, if a final configuration fails the test, it may not be accepted either. As an illustration, the right hand side of Fig. 7.5 shows two paths that belong to the same endpoints.

7.2. The worm algorithm

After establishing efficient sampling for the individual worldlines, the remaining part of the algorithm deals with changing the overall topology. This is achieved by an algorithmic enhancement called worm algorithm.

2006, Boninsegni *et al.* presented this advanced PIMC algorithm that was able to simulate particle numbers that were roughly one order of magnitude higher than previous versions [89, 93]. This speedup is due to an extension of configurational space which makes it easy to incorporate bosonic particle exchanges. The approach was used for the lattice version of path integral Monte Carlo in a previous work [94].

Looking at PIMC configurations in the worldline picture, it is clear that every bead has some particular part of the total weight attributed to itself: two ρ-factors link the bead with its neighbors on the same worldline and several potential terms quantify the interaction with beads of the same timeslice. This invites to think about these configurations in a local way: If beads are added to or removed from the system, the resulting configuration still has a well-defined weight.

In more detail, if one worldline is selected and beads are removed from this worldline in chronological order, an update scheme emerges that consists of shifting the last open end of a worldline forward and backward. As the resulting worldline configurations (which no longer close on themselves in imaginary time) resemble worms, this algorithm is called worm algorithm. The update scheme ensures that the worm is able to maneuver efficiently around global and local potential barriers and similar restrictions. Also, creating paths that use the periodic boundary conditions to close on themselves by winding around the system becomes a local move – this is important for the estimation of the superfluid density. If the current configuration has open worldline ends, it belongs to the worm sector (also called nondiagonal or G-sector). If the configuration is closed, it forms part of the partition sector (or diagonal or Z-sector, respectively). The extension of configurational space with worm configurations is not a purely numerical trick; the G-sector is closely linked with the single-particle Green's function as shown in Sec. 7.4.

If a worm configuration is created, two dangling ends are introduced. Convention is that the end that is connected to a bead with lower imaginary time (or to timeslice $\bar{M}-1$ with the use of the periodicity in imaginary time) is called $\mathcal{I}$, while the other one is denoted by $\mathcal{M}$. Introducing the worm formalism, the question arises how the potential energy of the worm timeslices should be treated. If the basic matrix element of Eq. (7.7) is examined again, it follows that the potential energy between $\mathcal{M}$ and all other beads of the timeslice should be fully counted, while $\mathcal{I}$ does not give any contribution. However, note that our use of the Baker-Campbell-Hausdorff formula in Eq. (7.7) gives the freedom to reorder $\hat{T}$ and $\hat{V}$ arbitrarily, e.g., $e^{-\epsilon(\hat{T}+\hat{V})} = e^{-\epsilon(0.8\hat{V}+\hat{T}+0.2\hat{V})}$. This means that there is a freedom to distribute a total weight of 1 between the potential energy of $\mathcal{I}$ and $\mathcal{M}$. For example, it would be possible to assign 0.2 of the potential energy to $\mathcal{M}$ and 0.8 to $\mathcal{I}$.

In the following, the specific worm updates are presented. The basic movements are implemented in four updates: *Cut*, *Glue*, *Advance* and *Recede*. To incorporate bosonic exchanges, another update called *Reconnect* is required. It takes one closed worldline and proposes to interchange it with the worm worldline. For performance reasons, an update *Diagonal-Worm* is added as well.

Diagonal-Worm The update *Diagonal-Worm* is an exact copy of the update Diagonal of the partition sector: A worldline is randomly selected, together with a stepsize $\bar{M}$. If $\mathcal{I}$ or $\mathcal{M}$ is lying on one of the beads which are proposed for modification, the update has to be rejected. If this is not the case, a normal Diagonal update is performed on the selected imaginary time interval.

Selection probabilities The connection between worm and partition sector is made by the update pair *Cut*/*Glue*. *Cut* attempts to open a diagonal configuration along an existing worldline, while *Glue* tries to extend the path from $\mathcal{I}$ to $\mathcal{M}$ by an appropriate *Lévy construction*.

As *Cut*/*Glue* are not self-inverse like *Diagonal* or *Rigid*, the update selection probabilities become important. We employed the following scheme: All updates operating in the diagonal sector (*Diagonal*, *Cut*, *Rigid*) are only called if the configuration is diagonal, while all nondiagonal updates (*Glue*, *Advance*, *Recede*, *Reconnect*) are only called if the configuration belongs to the worm sector. The probabilities for selecting *Cut*/*Glue* in their respective sectors are denoted by p_{Cut} and p_{Glue}.

Cut The *Cut* update selects a random worldline i (with probability $1/N$, where N is the current number of worldlines) and a random timeslice j (with probability $1/M$). Furthermore, a cutting length $\bar{M}$ is uniformly generated in an interval $[1, \bar{M}_{\text{non-diag}}]$, where $\bar{M}_{\text{non-diag}}$ is a simulation parameter reasonably smaller than M. Now, the proposed move is to remove the selected bead and the $\bar{M}$ ones preceding it. $\mathcal{M}$ is inserted on the selected bead and $\mathcal{I}$ is put on the bead that precedes $\mathcal{M}$ by $\bar{M}$ timeslices. The coordinate list of the removed beads is labeled by $(\boldsymbol{r}_i^{j-\bar{M}}, \ldots, \boldsymbol{r}_i^j)$.

An artificial weight $\mathcal{C}$ can be attributed to the worm sector for tuning purposes. If one of the sectors is dominant, this makes it easy to perform a Monte Carlo reweighting. As the acceptance ratio for this update depends on the *a priori* probability of *Glue*, the full explanation is given in the corresponding update description of *Glue*. *Cut* has to be accepted with probability

$$\min\left(1, \frac{p_{\text{Glue}}}{p_{\text{Cut}}} \frac{NM\mathcal{C}\bar{M}_{\text{non-diag}} \prod_{t=j-\bar{M}}^{j} e^{-\epsilon(V(\boldsymbol{R'}_t)-V(\boldsymbol{R}_t))}}{\rho(\boldsymbol{r}_{\mathcal{I}}, \boldsymbol{r}_{\mathcal{M}}, \bar{M}\epsilon)}\right). \tag{7.28}$$

$\boldsymbol{R'}$ and $\boldsymbol{R}$ do not have the same dimension – they are given by $\boldsymbol{R}_t = (\boldsymbol{r}_1^t, \boldsymbol{r}_2^t, \ldots, \boldsymbol{r}_i^t, \ldots, \boldsymbol{r}_N^t)$ and $\boldsymbol{R'}_t = (\boldsymbol{r}_1^t, \boldsymbol{r}_2^t, \ldots, \cancel{\boldsymbol{r}_i^t}, \ldots, \boldsymbol{r}_N^t)$. The method for the calculation of the potential energies of the worm ends has to follow one of the generally established conventions described above.

Glue The update *Glue* takes a worm configuration and checks the imaginary time distance between $\mathcal{I}$ and $\mathcal{M}$. If this distance is longer than $\bar{M}_{\text{non-diag}}$, the update is rejected. We label the bead coordinates of $\mathcal{M}$ by i and j, where i is the worldline name and j denotes the imaginary time instant. A *Lévy construction* is started between the endpoints marked by $\mathcal{I}$ and $\mathcal{M}$. The periodicity issues that were seen in *Diagonal* also have to be taken into account here. This gives a trajectory $(\boldsymbol{r}_i^{j-\bar{M}} = \boldsymbol{r}_{\mathcal{I}}, \ldots, \boldsymbol{r}_i^j = \boldsymbol{r}_{\mathcal{M}})$. As the *Lévy construction* is only used in one direction of the update pair, the $\rho(\boldsymbol{r}_{\mathcal{I}}, \boldsymbol{r}_{\mathcal{M}}, \bar{M}\epsilon)$-factor of the endpoints no longer drops out, cf. Eq. (7.27). In total, the acceptance ratio of *Glue* is

$$\min\left(1, \frac{p_{\text{Cut}}}{p_{\text{Glue}}} \frac{\rho(\boldsymbol{r}_{\mathcal{I}}, \boldsymbol{r}_{\mathcal{M}}, \bar{M}\epsilon) \prod_{t=j-\bar{M}}^{j} e^{-\epsilon(V(\boldsymbol{R'}_t)-V(\boldsymbol{R}_t))}}{NM\mathcal{C}\bar{M}_{\text{non-diag}}}\right). \tag{7.29}$$

Here, $\boldsymbol{R'}_t = (\boldsymbol{r}_1^t, \boldsymbol{r}_2^t, \ldots, \boldsymbol{r}_i^t, \ldots, \boldsymbol{r}_N^t)$ and $\boldsymbol{R}_t = (\boldsymbol{r}_1^t, \boldsymbol{r}_2^t, \ldots, \cancel{\boldsymbol{r}_i^t}, \ldots, \boldsymbol{r}_N^t)$. The update pair *Glue*/*Cut* is illustrated in Fig. 7.6.

Advance/Recede The update pair *Advance*/*Recede* complements *Cut*/*Glue* by moving the worm without the need of switching sectors. *Advance* progresses the worm worldline $\mathcal{I}$ further, while *Recede* takes it back to a configuration with fewer beads. We label the bead coordinates of $\mathcal{I}$ by i and j, where i is the worldline name and j denotes the imaginary time instant. These updates look like a less complicated version of *Cut*/*Glue*:

For the *Advance* step, there is only one fixed point of seeding, the real-space coordinate of $\mathcal{I}$. The new particle position $\boldsymbol{r}$ can be directly drawn from an exponential distribution $P(\boldsymbol{r}) = \rho(\boldsymbol{r}_{\mathcal{I}}, \boldsymbol{r}, \epsilon)$. Then, $\boldsymbol{r}$ is used to seed the next position $\boldsymbol{r'}$ from $P(\boldsymbol{r'}) = \rho(\boldsymbol{r}, \boldsymbol{r'}, \epsilon)$. In total, this procedure is repeated $\bar{M}$ times, where the integer $\bar{M}$ is uniformly chosen from $[1, \bar{M}_{\text{non-diag}}]$. This generates $\bar{M}$ new beads with coordinates $(\boldsymbol{r}_i^{j+1}, \ldots, \boldsymbol{r}_i^{j+\bar{M}})$. Defining the update selection probabilities of *Advance*/*Recede* as p_{Adv} and p_{Rec}, the acceptance ratio of *Advance* is given by

$$\min\left(1, \frac{p_{\text{Rec}}}{p_{\text{Adv}}} \prod_{t=j+1}^{j+\bar{M}} e^{-\epsilon(V(\boldsymbol{R'}_t)-V(\boldsymbol{R}_t))}\right), \tag{7.30}$$

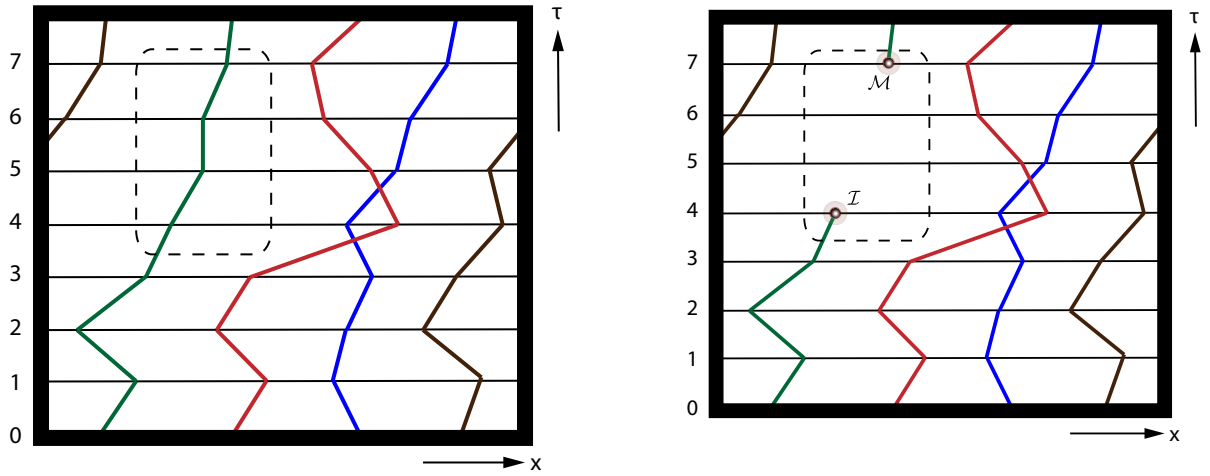

Figure 7.6.: The configurations linked by *Glue* and *Cut* are illustrated. The left configuration is available for *Cut*, the right configuration for *Glue*. In this case, $\bar{M} = 3$.

where $\boldsymbol{R}'_t = (\boldsymbol{r}_1^t, \boldsymbol{r}_2^t, \ldots, \boldsymbol{r}_i^t, \ldots, \boldsymbol{r}_N^t)$ and $\boldsymbol{R}_t = (\boldsymbol{r}_1^t, \boldsymbol{r}_2^t, \ldots, \cancel{\boldsymbol{r}_i^t}, \ldots, \boldsymbol{r}_N^t)$. The updates are illustrated in Fig. 7.7.

Remove also chooses a window $\bar{M}$ from $[1, \bar{M}_{\text{non-diag}}]$. It attempts to remove $\bar{M}$ beads starting from $\mathcal{I}$. If *Recede* tries to remove $\mathcal{M}$, it has to be rejected immediately. Its acceptance ratio is the inverse of *Advance*.

In principle, repeated use of *Recede* could remove all beads from the system. Therefore, it is convenient to define a minimum number of beads (usually on the order of $(N-1)M$) and reject *Recede* if the resulting number of beads would be below this threshold. Measurements should only be performed if the number of worldlines equals the desired number of particles. A similar issue arises if *Advance* is repeated several times: We advise to reject the update if $\mathcal{I}$ 'overtakes' $\mathcal{M}$. If $\mathcal{I}$ and $\mathcal{M}$ are at the same instant in imaginary time, this is admissible and will offer a way to measure the one-particle density matrix.

Reconnect The last – and crucial – update presented here takes care of different configuration space topologies. *Reconnect* takes a worm configuration and proposes to interchange the worm line with one of the diagonal worldlines. This ensures ergodicity and encodes the permutation problem into a local algorithm. *Reconnect* works as follows: First, an update window $\bar{M}$ is seeded uniformly from $[1, \bar{M}_{\text{non-diag}}]$. This defines a sequence of timeslices in which *Reconnect* is going to take place. We assume that $\mathcal{I}$ is on the j-th timeslice of the $i_{\mathcal{I}}$-th worldline. Next, a worldline has to be selected that will interchange its trajectory with the worm worldline. We employ a technique called *tower sampling* [4] to select this worldline in a weighted way:

- For all qualifying worldlines i', calculate $\rho_{i'} \equiv \rho(\boldsymbol{r}_{i_{\mathcal{I}}}^j, \boldsymbol{r}_{i'}^{j+\bar{M}}, \bar{M}\epsilon)$ (for the definition of qualifying, see below).
- Now create a distribution $p[i] = \sum_{i'=1}^{i} \rho_{i'} / \sum_{i'=1} \rho_{i'}$ and draw a random number r uniformly from $[0, 1]$.
- Determine the lowest i for which $p[i] > r$. The corresponding i is the selected worldline.

This way, a particle worldline i is selected with probability $\rho_i / \sum_{i'=1} \rho_{i'}$. The numerator of this expression will be canceled by the endpoint-term of a *Lévy construction*. Note that this *tower*

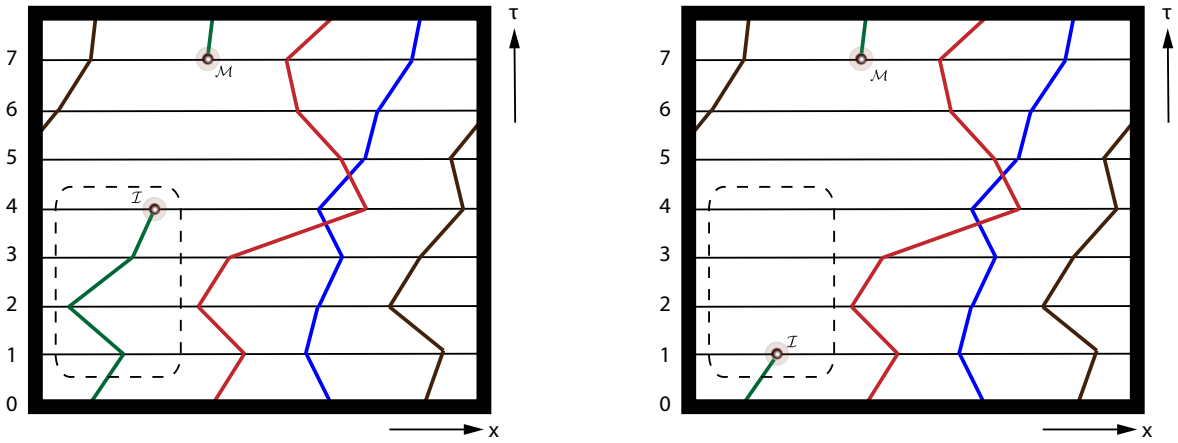

Figure 7.7.: The configurations linked by *Advance* and *Recede* are illustrated. The left configuration is receded, the right configuration is advanced. In this case, $\bar{M} = 3$.

sampling is potentially inefficient as it involves all particles of a given slice. However, there is no issue with restricting the number of worldlines that are included in the *tower sampling* to a subset of all qualifying configurations; e.g., only worldlines that are lying spatially close to $\mathcal{I}$ could be considered, as long as this is done in a controlled way. The cell scheme of the next section will give a natural classification of which particles to include. We still have to specify which worldlines qualify for *tower sampling*: The necessary criterion is that the worldline exists for $\tau = (j + \bar{M})\epsilon$. If $\mathcal{M}$ is lying on this timeslice or the $\bar{M}$ ones preceding it, the corresponding worldline has to be excluded.

Having selected a worldline i, a *Lévy construction*[2] is performed between $\boldsymbol{r}_{i_\mathcal{I}}^{j}$ and $\boldsymbol{r}_i^{j+\bar{M}}$. This yields a path $(\boldsymbol{r'}_i^{j} = \boldsymbol{r}_{i_\mathcal{I}}^{j}, \ldots, \boldsymbol{r'}_i^{j+\bar{M}} = \boldsymbol{r}_i^{j+\bar{M}})$. Now, the *Reconnect* update proposes to use this newly constructed path instead of the old path $(\boldsymbol{r}_i^{j}, \ldots, \boldsymbol{r}_i^{j+\bar{M}})$. If *Reconnect* is used in the version in which only a subset of qualifying configurations is considered, the update must be rejected if $\boldsymbol{r}_i^{j+\bar{M}}$ and $\boldsymbol{r}_i^{j}$ are not lying spatially close enough. The acceptance ratio is

$$\min\left(1, \frac{\sum_i \rho_i}{\sum_i \rho'_i} \prod_{t=j}^{j+\bar{M}-1} e^{-\epsilon(V(\boldsymbol{R'}_t) - V(\boldsymbol{R}_t))}\right), \tag{7.31}$$

where $\boldsymbol{R'}_t = (\boldsymbol{r}_1^t, \boldsymbol{r}_2^t, \ldots, \boldsymbol{r'}_i^t, \ldots, \boldsymbol{r}_N^t)$ and $\boldsymbol{R}_t = (\boldsymbol{r}_1^t, \boldsymbol{r}_2^t, \ldots, \boldsymbol{r}_i^t, \ldots, \boldsymbol{r}_N^t)$. The sum over ρ' includes all qualifying worldlines for the backward move. The *Reconnect* update is illustrated in Fig. 7.8.

7.3. Further algorithmic details

After discussing the basic worm algorithm for path integral Monte Carlo, this section presents three refinements that make this technique more versatile and powerful. While the first technique allows the simulation in a different statistical ensemble (the grand-canonical ensemble), both cell scheme and quartic action have the ability to enhance performance of the code noticeably.

[2]The periodicity issues of the *Lévy construction* also have to be taken into account for *Reconnect*.

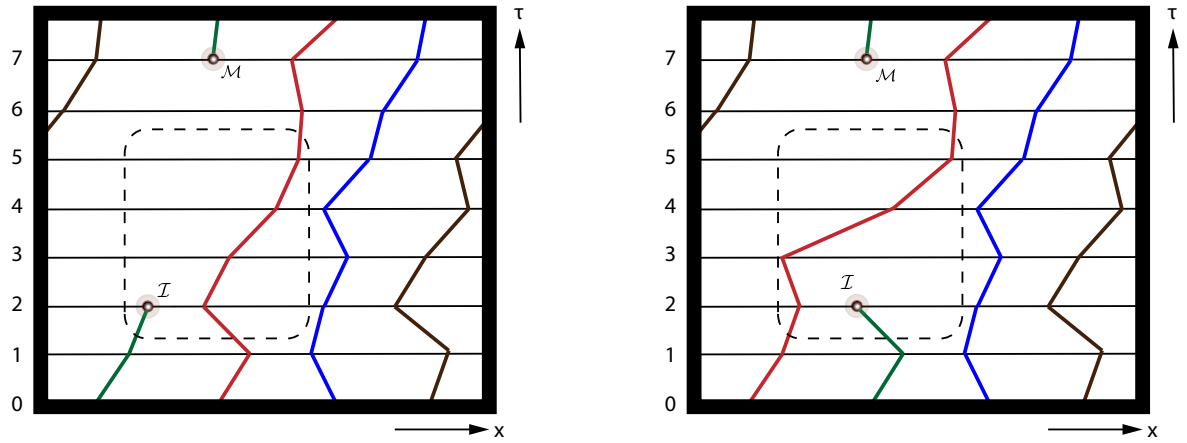

Figure 7.8.: The update *Reconnect* is illustrated. It takes the worm worldline and interchanges it with a normal particle worldline. The illustrative color change of the worldline sketches the performed particle exchange. In this case, $\bar{M} = 3$.

7.3.1. Grand-canonical sampling

Suppose that the current configuration of a PIMC simulation is given by the left part of Fig. 7.8. For now, the instant rejections arising because of the number of beads exceeding a certain threshold are ignored. If *Advance* is performed on this configuration several times in a row, configurations that correspond to any particle number can be reached. Therefore, loosening these bead number thresholds seems quite natural, and in fact omitting them is a straightforward way to achieve grand-canonical sampling. Here, the grand-canonical partition function $\mathcal{Z}$ is given by $\mathcal{Z} = \mathrm{tr}(e^{-\beta(\hat{H}-\mu\hat{N})})$. In this expression, the trace is over a complete basis of the system that includes an arbitrary number of particles. μ is the chemical potential. Expanding the trace gives

$$\begin{aligned} \mathcal{Z} &= \sum_{N=0}^{\infty} \int \mathrm{d}\boldsymbol{R}^{(N)} \langle \boldsymbol{\mathcal{R}}^{(N)} | e^{-\beta(\hat{H}-\mu\hat{N})} | \boldsymbol{\mathcal{R}}^{(N)} \rangle \\ &= \sum_{N=0}^{\infty} \int \mathrm{d}\boldsymbol{R}^{(N)} \langle \boldsymbol{\mathcal{R}}^{(N)} | e^{-\beta\hat{H}} | \boldsymbol{\mathcal{R}}^{(N)} \rangle e^{\beta\mu N} = \sum_{N=0}^{\infty} Z(N) e^{\beta\mu N}, \end{aligned} \tag{7.32}$$

where $Z(N)$ denotes the canonical partition function of N particles. Note the clear distinction between the symmetrized state $|\boldsymbol{\mathcal{R}}^{(N)}\rangle$ and the differential $\mathrm{d}\boldsymbol{R}^{(N)} = \mathrm{d}\boldsymbol{r}_1 \ldots \mathrm{d}\boldsymbol{r}_N$.

Eq. (7.32) shows that $\mathcal{Z}$ can be sampled by allowing the insertion and removal of complete worldlines (by *Cut*/*Glue* and two further updates which will be presented later), and by attributing a factor of $e^{\beta\mu}$ to each worldline. The latter factor can be locally distributed among the beads by giving each bead an additional weight factor of $e^{\mu\beta/M} = e^{\beta\epsilon}$.

As a direct consequence of grand-canonical sampling, the particle number is no longer fixed and fluctuates around a mean particle number $\langle N \rangle$. This value is determined by the chemical potential, i.e., N now is a standard observable. Note that measurements of standard observables in the grand-canonical and the canonical ensemble do not agree for small N and V; for these simulations, it is perfectly admissible to get different results for different ensembles.

In order to make the transition between particle numbers easier, another update pair is used in the grand-canonical sector, *Insert* and *Remove*. *Insert* takes a diagonal configuration and selects a random timeslice j together with a seeding length $\bar{M} \in [1, \bar{M}_{\text{non-diag}}]$. Next, it generates a first

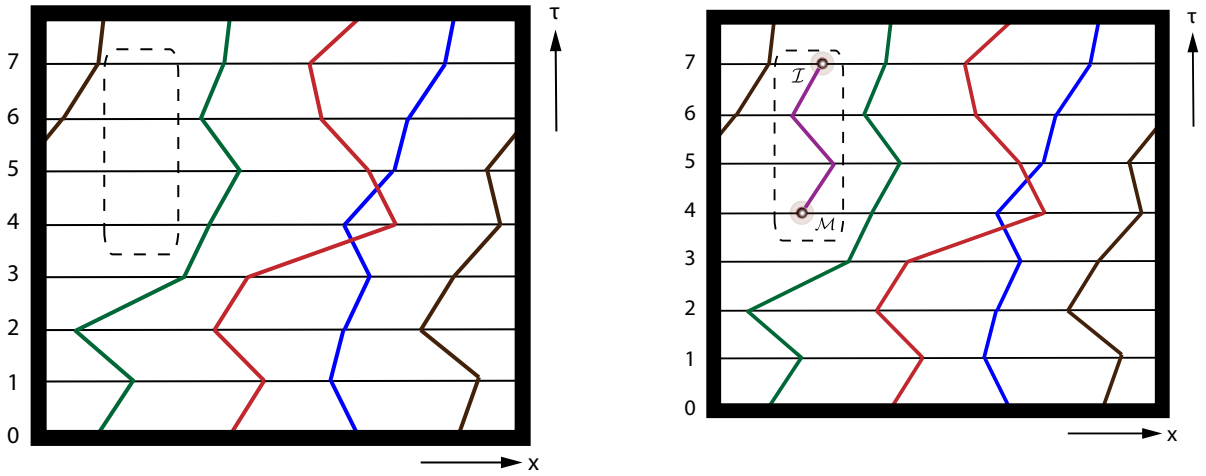

Figure 7.9.: The update pair *Insert*/*Remove* is illustrated. The left configuration allows an insertion, the right a removal. In this case, $\bar{M} = 3$.

coordinate $\boldsymbol{r}_1$ uniformly in the simulation box (with probability $\mathrm{d}\boldsymbol{r}_1/V$). Taking this point as a starting point, the steps for the *Advance* update are repeated and a particle worldline of $\bar{M}+1$ beads is created. In the reverse direction, *Remove* is only applicable to worm configurations. It selects the worm worldline and measures the distance in imaginary time between $\mathcal{I}$ and $\mathcal{M}$. If this distance is bigger than $\bar{M}_{\text{non-diag}}$, the update is rejected. Otherwise, the complete removal of all beads between worm head and tail is proposed. The acceptance probability of *Insert* is

$$\min\left(1, \frac{p_{\text{rem}}}{p_{\text{ins}}} V\mathcal{C}M\bar{M}_{\text{non-diag}} \prod_{t=j}^{j+\bar{M}} e^{-\epsilon(V(\boldsymbol{R'}_t)-V(\boldsymbol{R}_t))}\right), \tag{7.33}$$

where p_{ins} and p_{rem} are the update selection probabilities of *Insert* and *Remove*, respectively. If the generated trajectory is labeled by $(\boldsymbol{r}^j_{N+1}, \ldots, \boldsymbol{r}^{j+\bar{M}}_{N+1})$, $\boldsymbol{R'}_t$ and $\boldsymbol{R}_t$ are given by $\boldsymbol{R'}_t = (\boldsymbol{r}^t_1, \boldsymbol{r}^t_2, \ldots, \boldsymbol{r}^t_N, \boldsymbol{r}^t_{N+1})$ and $\boldsymbol{R}_t = (\boldsymbol{r}^t_1, \boldsymbol{r}^t_2, \ldots, \boldsymbol{r}^t_N)$. The acceptance ratio of *Remove* is the inverse of *Insert*. The whole process is illustrated in Fig. 7.9. In principle, it is necessary to include the $\frac{1}{N!}$ factor in the weight of $\mathcal{Z}$. A trick can help to avoid this: If the worldline produced by *Insert* always has the worldline label with the highest number and if *Remove* is allowed to operate on any worldline label, this factor is silently included in the algorithm. This implies that if *Remove* is successfully applied, the label of the removed line has to be given to the worldline with the highest particle label to stay consistent. In fact, following this trick breaks detailed balance. Nevertheless, this is no problem as it is done in a controlled and safe way – relabeling all worldlines still yields a valid configuration.

This completes our update scheme. Looking at the acceptance ratio of *Insert*, a straightforward way to tune $\mathcal{C}$ is to set it to $\mathcal{C} = C(VM\bar{M}_{\text{non-diag}})^{-1}$, where C is a constant on the order of 1. This eliminates large factors from the acceptance ratios and assures that the same acceptance ratio is reproduced for simulations of different V, M or $\bar{M}_{\text{non-diag}}$.

7.3.2. Cell scheme

The next enhancement that is presented in this section is not specific for PIMC. In fact, it is generic to all problems that involve N particles with pair-wise interactions of the form

$V(\boldsymbol{R}) = \sum_{i<j} U(|\boldsymbol{r}_i - \boldsymbol{r}_j|)$. If the position of one of the particles is changed, a recomputation of the potential energy of the remaining $N-1$ particles with the displaced particle has to be performed. This is a computationally expensive operation for two reasons: First, the evaluation of the potential might be a nontrivial operation. Secondly, the scaling of the problem with $\mathcal{O}(N^2)$ is disadvantageous.

In many cases, some natural cutoff r_Λ of the potential exists or can be established by identifying relevant length scales. This way, the computation of the potential energy can be simplified significantly by assigning potential energy 0 to all pairs of particles with mutual distance large than r_Λ.

Nevertheless, an iteration over all $N-1$ particles is still necessary. This can be cured by creating a cubic cell grid with width $r_\Lambda/2$ on top of the simulation box. For simplicity, we assume that a cubic simulation box is used with a basis length that is a multiple of $r_\Lambda/2$. As any cell width larger than $r_\Lambda/2$ can be used, the generalization of the cell scheme to an arbitrary simulation box is straightforward. Now, each particle position corresponds to exactly one cell (it does not matter if particles lying on the border of two cells are attributed to the one cell or the other). A data structure has to be introduced that saves the particles which lie in each cell. Then, if a recomputation of the potential energy is necessary, it is possible to neglect all particles which are more than one cell away from the original particle: Only the neighboring cells and the cell of the issuing particle have to be taken into account, while all other particles lie outside the cutoff length r_Λ. For a given density, this reduces the scaling $\mathcal{O}(N)$ to $\mathcal{O}(1)$ as the number of neighboring particles does not grow with the number of particles or system size. To be precise, we define neighboring cells as all cells that have at least one point in common with the original cell: there are 8 neighboring cells in two dimensions and 26 neighboring cells in three dimensions.

The cell scheme combines with *Reconnect* in a very natural way: If only particles in the cell of $\mathcal{I}$ or neighboring cells are considered for *tower sampling*, this part of *Reconnect* also gets constant scaling with the number of particles.

7.3.3. The quartic action

As a last algorithmic extension, the expansion of the partition function in terms of the worldline picture has to be reviewed. For systems with a smooth potential, the first-order result of the Baker-Campbell-Hausdorff formula is usually a good approximation (this will be quantified below). For more complicated potentials, this statement is no longer true: For a correct expansion of the partition function, it might be necessary to increase the number of timeslices to some impractical value.

Therefore, it is time to reconsider our use of the Baker-Campbell-Hausdorff formula and try to apply further analytical insight into the simulation. This expansion follows the original works of Suzuki and Chin [95, 96]. The form of the Baker-Campbell-Hausdorff formula which will be applied is the following:

$$e^{\epsilon\hat{X}} e^{\epsilon\hat{Y}} = e^{\epsilon\hat{X}+\epsilon\hat{Y}+\frac{1}{2}\epsilon^2[\hat{X},\hat{Y}]+\frac{1}{12}\epsilon^3[\hat{X},[\hat{X},\hat{Y}]]-\frac{1}{12}\epsilon^3[\hat{Y},[\hat{X},\hat{Y}]]-\frac{1}{24}\epsilon^4[\hat{Y},[\hat{X},[\hat{X},\hat{Y}]]]} + \mathcal{O}(\epsilon^5). \tag{7.34}$$

Now, we start by applying this expression to the product of kinetic and potential energy (whose coefficients will become clear in the end):

$$e^{\frac{1}{3}\epsilon\hat{V}} e^{\epsilon\hat{T}} = e^{\frac{1}{3}\epsilon\hat{V}+\epsilon\hat{T}+\frac{1}{6}\epsilon^2[\hat{V},\hat{T}]+\frac{1}{108}\epsilon^3[\hat{V},[\hat{V},\hat{T}]]-\frac{1}{36}\epsilon^3[\hat{T},[\hat{V},\hat{T}]]-\frac{1}{216}\epsilon^4[\hat{T},[\hat{V},[\hat{V},\hat{T}]]]} + \mathcal{O}(\epsilon^5). \tag{7.35}$$

Next, a factor $e^{\frac{4}{3}\epsilon(\hat{V}-\frac{1}{12}\epsilon^2[\hat{V},[\hat{V},\hat{T}]])}$ is multiplied to this expression from the right. We can ignore

all terms that are of order ϵ^5 or higher; for visual clarity, the logarithm of the expression is given:

$$\begin{aligned}\ln\left(e^{\frac{1}{3}\epsilon\hat{V}}e^{\epsilon\hat{T}}e^{\frac{4}{3}\epsilon(\hat{V}-\frac{1}{12}\epsilon^2[\hat{V},[\hat{V},\hat{T}]])}\right) &= \frac{5}{3}\epsilon\hat{V}+\epsilon\hat{T}-\frac{1}{2}\epsilon^2[\hat{V},\hat{T}] \\ &- \frac{11}{108}\epsilon^3[\hat{V},[\hat{V},\hat{T}]]-\frac{5}{36}\epsilon^3[\hat{T},[\hat{V},\hat{T}]] \\ &+ \frac{1}{54}\epsilon^4[\hat{V},[\hat{V},[\hat{V},\hat{T}]]]-\frac{17}{216}\epsilon^4[\hat{T},[\hat{V},[\hat{V},\hat{T}]]] \\ &+ \frac{5}{54}\epsilon^4[\hat{V},[\hat{T},[\hat{V},\hat{T}]]]+\mathcal{O}(\epsilon^5).\end{aligned} \tag{7.36}$$

Finally, a factor $e^{\epsilon\hat{T}}e^{\frac{1}{3}\epsilon\hat{V}}$ will be multiplied from the right; expanding this factor is very similar to Eq. (7.35):

$$e^{\epsilon\hat{T}}e^{\frac{1}{3}\epsilon\hat{V}} = e^{\epsilon\hat{T}+\frac{1}{3}\epsilon\hat{V}-\frac{1}{6}\epsilon^2[\hat{V},\hat{T}]+\frac{1}{108}\epsilon^3[\hat{V},[\hat{V},\hat{T}]]-\frac{1}{36}\epsilon^3[\hat{T},[\hat{V},\hat{T}]]+\frac{1}{216}\epsilon^4[\hat{V},[\hat{T},[\hat{V},\hat{T}]]]}+\mathcal{O}(\epsilon^5). \tag{7.37}$$

Appending on the right of Eq. (7.36) yields

$$e^{\frac{1}{3}\epsilon\hat{V}}e^{\epsilon\hat{T}}e^{\frac{4}{3}\epsilon(\hat{V}-\frac{1}{12}\epsilon^2[\hat{V},[\hat{V},\hat{T}]])}e^{\epsilon\hat{T}}e^{\frac{1}{3}\epsilon\hat{V}} = e^{2\epsilon\hat{V}+2\epsilon\hat{T}}+\mathcal{O}(\epsilon^5), \tag{7.38}$$

where we use the identity

$$[\hat{V},[\hat{T},[\hat{V},\hat{T}]]] = [\hat{T},[\hat{V},[\hat{V},\hat{T}]]]. \tag{7.39}$$

If this decomposition is used for every timeslice, a total error of order $\mathcal{O}(\epsilon^4)$ is accumulated.

A nontrivial part of this quartic scheme is the additional $[\hat{V},[\hat{V},\hat{T}]]$ term. Using the explicit expressions[3] $\hat{V}=\sum_{i<j}U(|\hat{\boldsymbol{x}}_i-\hat{\boldsymbol{x}}_j|)$ and $\hat{T}=\sum_i\frac{\hat{\boldsymbol{p}}_i^2}{2m}$, we evaluate

$$\begin{aligned}\left[\hat{V},[\hat{V},\hat{T}]\right] &= \left[\sum_{k<l}U(|\hat{\boldsymbol{x}}_k-\hat{\boldsymbol{x}}_l|),\left[\sum_{h<j}U(|\hat{\boldsymbol{x}}_h-\hat{\boldsymbol{x}}_j|),\sum_i\frac{\hat{\boldsymbol{p}}_i^2}{2m}\right]\right] \\ &= \frac{1}{2m}\sum_{i,j\neq i,k\neq i}\left[U(|\hat{\boldsymbol{x}}_i-\hat{\boldsymbol{x}}_k|),\left[U(|\hat{\boldsymbol{x}}_i-\hat{\boldsymbol{x}}_j|),\hat{\boldsymbol{p}}_i^2\right]\right]\end{aligned} \tag{7.40}$$

by noticing that momentum and position operators of different particles commute, i.e.,

$$\left[U(|\hat{\boldsymbol{x}}_h-\hat{\boldsymbol{x}}_j|),\hat{\boldsymbol{p}}_i^2\right]=0 \tag{7.41}$$

for $h\neq i$ and $j\neq i$. For simplicity, we will restrict ourselves to one dimension in the following statements. Generalizing to d dimensions is straightforward by noticing that

$$\left[\hat{\boldsymbol{O}}^{(a)},\hat{\boldsymbol{O}}^{(b)}\right]\propto\delta_{a,b} \tag{7.42}$$

where $\hat{\boldsymbol{O}}^{(a)}$ is the a-th component of an arbitrary quantum mechanical operator $\hat{\boldsymbol{O}}$. Defining $\hat{x}_{ij}=|\hat{x}_i-\hat{x}_j|$, the relevant one-dimensional commutator is

$$\left[U(\hat{x}_{ik}),\left[U(\hat{x}_{ij}),\hat{p}_i^2\right]\right] \tag{7.43}$$

If the potential can be written as a power series in $\hat{x}_i$, the commutator $[U(\hat{x}_{ij}),\hat{p}_i]$ can be evaluated with the help of the identity $[\hat{x}_i^n,\hat{p}_i]=ni\hat{x}_i^{n-1}$ for $n\in\mathbb{N}$ (which is a direct consequence

[3] Here, we assume that no external potential is used. Generalizing to this case is straightforward.

of the canonical commutation relation $[\hat{x}_i, \hat{p}_i] = i$):

$$\begin{aligned}[U(\hat{x}_{ij}), \hat{p}_i] &= U(\hat{x}_{ij})\hat{p}_i - \hat{p}_i U(\hat{x}_{ij}) = U(\hat{x}_{ij})\hat{p}_i - \hat{p}_i \sum_l u_l \hat{x}_i^l \\ &= U(\hat{x}_{ij})\hat{p}_i - \sum_l u_l \hat{x}_i^l \hat{p}_i + i \sum_l u_l l \hat{x}_i^{l-1} = i \frac{\mathrm{d}U(\hat{x}_{ij})}{\mathrm{d}\hat{x}_i}. \end{aligned} \tag{7.44}$$

In this expression, the power series coefficients u_l have been introduced. Using this, the final result can be derived:

$$\begin{aligned}\left[U(\hat{x}_{ik}), \left[U(\hat{x}_{ij}), \hat{p}_i^2\right]\right] &= \left[U(\hat{x}_{ik}), U(\hat{x}_{ij})\hat{p}_i^2 - \hat{p}_i^2 U(\hat{x}_{ij})\right] \\ &= [U(\hat{x}_{ik}), U(\hat{x}_{ij})\hat{p}_i\hat{p}_i - \hat{p}_i U(\hat{x}_{ij})\hat{p}_i + \hat{p}_i U(\hat{x}_{ij})\hat{p}_i - \hat{p}_i\hat{p}_i U(\hat{x}_{ij})] \\ &= [U(\hat{x}_{ik}), [U(\hat{x}_{ij}), \hat{p}_i]\,\hat{p}_i + \hat{p}_i\,[U(\hat{x}_{ij}), \hat{p}_i]] \\ &= i\left[U(\hat{x}_{ik}), \frac{\mathrm{d}U(\hat{x}_{ij})}{\mathrm{d}\hat{x}_i}\hat{p}_i + \hat{p}_i \frac{\mathrm{d}U(\hat{x}_{ij})}{\mathrm{d}\hat{x}_i}\right] \\ &= i\left[U(\hat{x}_{ik}), \frac{\mathrm{d}U(\hat{x}_{ij})}{\mathrm{d}\hat{x}_i}\hat{p}_i + \frac{\mathrm{d}U(\hat{x}_{ij})}{\mathrm{d}\hat{x}_i}\hat{p}_i - i\frac{\mathrm{d}^2U(\hat{x}_{ij})}{\mathrm{d}\hat{x}_i^2}\right] \\ &= i\left[U(\hat{x}_{ik}), 2\frac{\mathrm{d}U(\hat{x}_{ij})}{\mathrm{d}\hat{x}_i}\hat{p}_i\right] \\ &= 2i\frac{\mathrm{d}U(\hat{x}_{ij})}{\mathrm{d}\hat{x}_i}\,[U(\hat{x}_{ik}), \hat{p}_i] \\ &= -2\left(\frac{\mathrm{d}U(\hat{x}_{ij})}{\mathrm{d}\hat{x}_i}\right)\left(\frac{\mathrm{d}U(\hat{x}_{ik})}{\mathrm{d}\hat{x}_i}\right). \end{aligned} \tag{7.45}$$

The following facts have been used to derive this statement:

- $\left[\frac{\mathrm{d}U(\hat{x}_{ij})}{\mathrm{d}\hat{x}_i}, \hat{p}_i\right] = i\frac{\mathrm{d}^2U(\hat{x}_{ij})}{\mathrm{d}\hat{x}_i^2}$ can be shown by a slight modification of Eq. (7.44).
- $\frac{\mathrm{d}^2U(\hat{x}_{ij})}{\mathrm{d}\hat{x}_i^2}$ commutes with $U(\hat{x}_{ij})$, just as $\frac{\mathrm{d}U(\hat{x}_{ij})}{\mathrm{d}\hat{x}_i}$. This can be seen by considering the power series of U again.

Plugging Eq. (7.45) back into Eq. (7.40) and generalizing to d dimensions, the whole statement reads

$$\begin{aligned}\left[\hat{V}, [\hat{V}, \hat{T}]\right] &= \frac{1}{2m}\sum_{i,j\neq i,k\neq i}\left[U(|\hat{\boldsymbol{x}}_i - \hat{\boldsymbol{x}}_k|), \left[U(|\hat{\boldsymbol{x}}_i - \hat{\boldsymbol{x}}_j|), \hat{\boldsymbol{p}}_i^2\right]\right] \\ &= -\frac{1}{m}\sum_{i,j\neq i,k\neq i}\left(\frac{\mathrm{d}U(\hat{\boldsymbol{x}}_{ij})}{\mathrm{d}\hat{\boldsymbol{x}}_i}\right)\left(\frac{\mathrm{d}U(\hat{\boldsymbol{x}}_{ik})}{\mathrm{d}\hat{\boldsymbol{x}}_i}\right). \\ &= -\frac{1}{m}\sum_i\left(\sum_{j\neq i}\frac{\mathrm{d}U(\hat{\boldsymbol{x}}_{ij})}{\mathrm{d}\hat{\boldsymbol{x}}_i}\right)^2 \equiv -\frac{1}{m}\hat{F}, \end{aligned} \tag{7.46}$$

where $\hat{\boldsymbol{x}}_{ij}$ was defined as $\hat{\boldsymbol{x}}_{ij} \equiv |\hat{\boldsymbol{x}}_i - \hat{\boldsymbol{x}}_j|$ and the force $\hat{F} = \sum_{j\neq i}\frac{\mathrm{d}U(\hat{\boldsymbol{x}}_{ij})}{\mathrm{d}\hat{\boldsymbol{x}}_i}$ was introduced. This is why the quartic approximation is also often called the *force approximation*. Note that $\hat{F}$ is diagonal in position space.

The total decomposition of a single timeslice now reads

$$\begin{aligned}e^{2\epsilon\hat{V}+2\epsilon\hat{T}} &= e^{\frac{1}{3}\epsilon\hat{V}}e^{\epsilon\hat{T}}e^{\frac{4}{3}\epsilon(\hat{V}-\frac{1}{12}\epsilon^2[\hat{V},[\hat{V},\hat{T}]])}e^{\epsilon\hat{T}}e^{\frac{1}{3}\epsilon\hat{V}} + \mathcal{O}(\epsilon^5) \\ &= e^{\frac{1}{3}\epsilon\hat{V}}e^{\epsilon\hat{T}}e^{\frac{4}{3}\epsilon(\hat{V}+\frac{1}{12m}\epsilon^2\hat{F})}e^{\epsilon\hat{T}}e^{\frac{1}{3}\epsilon\hat{V}} + \mathcal{O}(\epsilon^5). \end{aligned} \tag{7.47}$$

As before, the matrix elements of this expression are needed:

$$\begin{aligned}\langle \boldsymbol{R}_{i-1}|e^{2\epsilon\hat{V}+2\epsilon\hat{T}}|\boldsymbol{R}_{i+1}\rangle &= \langle \boldsymbol{R}_{i-1}|e^{\frac{1}{3}\epsilon\hat{V}}e^{\epsilon\hat{T}}e^{\frac{4}{3}\epsilon(\hat{V}+\frac{1}{12m}\epsilon^2\hat{F})}e^{\epsilon\hat{T}}e^{\frac{1}{3}\epsilon\hat{V}}|\boldsymbol{R}_{i+1}\rangle \\ &= \int \mathrm{d}\boldsymbol{R}_i \langle \boldsymbol{R}_{i-1}|e^{\frac{1}{3}\epsilon\hat{V}}e^{\epsilon\hat{T}}|\boldsymbol{\mathcal{R}}_i\rangle\langle\boldsymbol{\mathcal{R}}_i|e^{\frac{4}{3}\epsilon(\hat{V}+\frac{1}{12m}\epsilon^2\hat{F})}e^{\epsilon\hat{T}}e^{\frac{1}{3}\epsilon\hat{V}}|\boldsymbol{R}_{i+1}\rangle.\end{aligned} \tag{7.48}$$

This makes it easy to read off the translation into timeslices. In the quartic approximation, not all slices are treated in the same way any more:

$$\langle \boldsymbol{R}_{i-1}|e^{\frac{1}{3}\epsilon\hat{V}}e^{\epsilon\hat{T}}|\boldsymbol{\mathcal{R}}_i\rangle$$

is very similar to the primitive approximation – only the coefficients are different. The matrix elements

$$\langle \boldsymbol{\mathcal{R}}_i|e^{\frac{4}{3}\epsilon(\hat{V}+\frac{1}{12m}\epsilon^2\hat{F})}e^{\epsilon\hat{T}}e^{\frac{1}{3}\epsilon\hat{V}}|\boldsymbol{R}_{i+1}\rangle$$

are more interesting, as they require evaluation of the potential forces. The last $e^{\frac{1}{3}\hat{V}}$ term can be put into the potential term of the next timeslice, such that the following recipe is valid:

- For an even number of timeslices, treat everything just as before and attribute a factor $\frac{2}{3}$ to the potential energy term.
- For an odd number of timeslices, treat the kinetic part as before, but use the potential term $e^{\frac{4}{3}\epsilon(\hat{V}+\frac{1}{12m}\epsilon^2\hat{F})}$ instead of the standard potential.

The final decomposition of the partition function in the quartic approximation is

$$\begin{aligned}Z = \frac{1}{N!}\sum_{\mathcal{P}}\left(\prod_{t=0}^{\frac{M}{2}-1}\int \mathrm{d}\boldsymbol{R}_{2t}\,\mathrm{d}\boldsymbol{R}_{2t+1}\right)\left(\prod_{t=0}^{\frac{M}{2}-1}\rho(\boldsymbol{R}_{2t},\boldsymbol{R}_{2t+1},\epsilon)e^{-\frac{2}{3}\epsilon V(\boldsymbol{R}_{2t})}\right)\times \\ \times\left(\prod_{t=0}^{\frac{M}{2}-1}\rho(\boldsymbol{R}_{2t+1},\boldsymbol{R}_{2t+2},\epsilon)e^{-\frac{4}{3}\epsilon V(\boldsymbol{R}_{2t+1})}e^{-\frac{1}{9m}\epsilon^3 F(\boldsymbol{R}_{2t+1})}\right)+\mathcal{O}(\epsilon^4)\end{aligned} \tag{7.49}$$

with $\boldsymbol{R}_M = \mathcal{P}(\boldsymbol{R}_0)$.

7.4. Observables

After establishing the core of the PIMC simulation, it is time to introduce typical observables. These are classified as diagonal or nondiagonal, corresponding to measurements in the partition function sector or worm sector[4]. In general, observables can be classified as scalar or vector, depending on whether a concrete measurement of the observable yields a scalar or vector result. If no further specification is given, we refer to a canonical simulation of particles in the primitive approximation. The extension of the observables to the other approximations and ensembles introduced in previous chapters is straightforward.

[4]Note the strong similarities with Ref. [97].

7.4.1. Energy

As a first observable, the energy estimator is discussed. The ensemble average of the total energy is given by

$$E = \langle \hat{H} \rangle = \frac{\mathrm{tr}(\hat{H} e^{-\beta \hat{H}})}{Z}. \tag{7.50}$$

Rewriting this expression in terms of a derivative with respect to β gives access to a suitable estimator

$$E = -\frac{1}{Z} \frac{\partial Z}{\partial \beta}. \tag{7.51}$$

If this form is used with the partition function in the path integral language, i.e.,

$$Z = \frac{1}{N!} \sum_{\mathcal{P}} \left(\prod_{t=0}^{M-1} \int \mathrm{d}\boldsymbol{R}_t \right) \left(\prod_{t=0}^{M-1} \rho(\boldsymbol{R}_t, \boldsymbol{R}_{t+1}, \epsilon) e^{-\epsilon V(\boldsymbol{R}_t)} \right) + \mathcal{O}(\epsilon), \tag{7.52}$$

the following estimator is derived by explicit evaluation of the derivative (remember that $\epsilon = \beta/M$):

$$\begin{aligned}
E =& -\frac{1}{N!} \frac{1}{Z} \sum_{\mathcal{P}} \left(\prod_{t=0}^{M-1} \int \mathrm{d}\boldsymbol{R}_t \right) \frac{\partial}{\partial \beta} \left(\prod_{t=0}^{M-1} \rho(\boldsymbol{R}_t, \boldsymbol{R}_{t+1}, \epsilon) e^{-\epsilon V(\boldsymbol{R}_t)} \right) \\
=& -\frac{1}{N!} \frac{1}{Z} \sum_{\mathcal{P}} \left(\prod_{t=0}^{M-1} \int \mathrm{d}\boldsymbol{R}_t \sum_{\boldsymbol{W}_t} \right) \frac{\partial}{\partial \beta} \left(\prod_{t=0}^{M-1} \left(\frac{m}{2\pi\epsilon} \right)^{\frac{Nd}{2}} e^{-\frac{m(\boldsymbol{R}_{t+1} - \boldsymbol{R}_t + \boldsymbol{W}_t)^2}{2\epsilon}} e^{-\epsilon V(\boldsymbol{R}_t)} \right) \\
=& -\frac{1}{N!} \frac{1}{Z} \sum_{\mathcal{P}} \left(\prod_{t=0}^{M-1} \int \mathrm{d}\boldsymbol{R}_t \sum_{\boldsymbol{W}_t} \right) \left(\prod_{t=0}^{M-1} \left(\frac{m}{2\pi\epsilon} \right)^{\frac{Nd}{2}} e^{-\frac{m(\boldsymbol{R}_{t+1} - \boldsymbol{R}_t + \boldsymbol{W}_t)^2}{2\epsilon}} e^{-\epsilon V(\boldsymbol{R}_t)} \right) \times \\
& \times \sum_{t=0}^{M-1} \left(-\frac{Nd}{2M\epsilon} + \frac{m(\boldsymbol{R}_{t+1} - \boldsymbol{R}_t + \boldsymbol{W}_t)^2}{2\epsilon^2 M} - \frac{V(\boldsymbol{R}_t)}{M} \right) \\
=& \left\langle \frac{Nd}{2\epsilon} - \sum_{t=0}^{M-1} \frac{m(\boldsymbol{R}_{t+1} - \boldsymbol{R}_t + \boldsymbol{W}_t)^2}{2\epsilon^2 M} + \sum_{t=0}^{M-1} \frac{V(\boldsymbol{R}_t)}{M} \right\rangle
\end{aligned} \tag{7.53}$$

A measurement now consists of evaluating the bracketed expression for the current worldline configuration and adding its value to a running sum. Looking closely, the second and third term of the estimator are just averages over all timeslices.

7.4.2. Superfluid density

We present a derivation of the superfluid density in terms of the static partition function, following the argumentation of Ref. [98]. The superfluid fraction of a quantum liquid is defined as the part of the liquid that is not responding to a rotation induced from outside (the normal liquid just follows this motion). If the liquid is rotated with infinitesimal angular velocity, the rotation is equivalent to a straight displacement of the system with some velocity $\boldsymbol{v}$. For our analysis, we employ two reference frames, a laboratory frame denoted by $\mathcal{F}$ and a moving frame called $\mathcal{F}'$, where the relative velocity between the frames is $\boldsymbol{v}$. The liquid is moving with velocity $\boldsymbol{v}$ with respect to the laboratory frame $\mathcal{F}$. This means that it is at rest in $\mathcal{F}'$ – all expressions from the previous sections can be reused in $\mathcal{F}'$ and the corresponding partition function Z and Hamiltonian $\hat{H}$ remain unchanged. This setup is illustrated in Fig. 7.10.

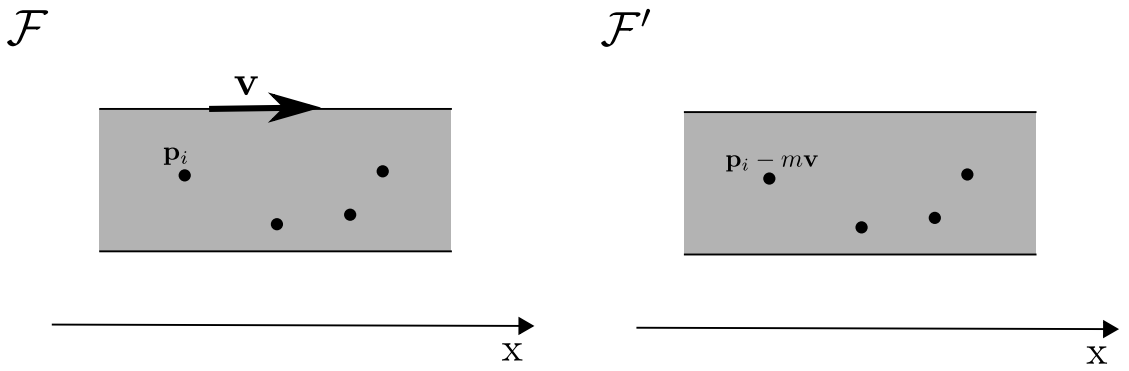

Figure 7.10.: Two reference frames are used to derive the superfluid density. In the left panel, the laboratory frame $\mathcal{F}$ is shown, while the right panel illustrates the moving system $\mathcal{F}'$.

Now, we introduce the boost operator as

$$\hat{U}_{\boldsymbol{v}} = \exp\left(-im\boldsymbol{v}\sum_{n=1}^{N}\hat{\boldsymbol{r}}_n\right). \tag{7.54}$$

If the total momentum operator is given by $\hat{\boldsymbol{P}}_{\text{tot}} = \sum_{i=1}^{N}\hat{\boldsymbol{p}}_i$, the following statements can be shown by using $[\hat{x}^n, \hat{p}] = ni\hat{x}^{n-1}$:

$$\hat{U}_{\boldsymbol{v}}^\dagger \hat{\boldsymbol{r}}_i \hat{U}_{\boldsymbol{v}} = \hat{\boldsymbol{r}}_i \tag{7.55}$$
$$\hat{U}_{\boldsymbol{v}}^\dagger \hat{\boldsymbol{p}}_i \hat{U}_{\boldsymbol{v}} = \hat{\boldsymbol{p}}_i - m\boldsymbol{v} \tag{7.56}$$
$$\hat{U}_{\boldsymbol{v}} \hat{\boldsymbol{p}}_i \hat{U}_{\boldsymbol{v}}^\dagger = \hat{\boldsymbol{p}}_i + m\boldsymbol{v} \tag{7.57}$$
$$\hat{U}_{\boldsymbol{v}}^\dagger \hat{\boldsymbol{P}}_{\text{tot}} \hat{U}_{\boldsymbol{v}} = \hat{\boldsymbol{P}}_{\text{tot}} - m\boldsymbol{v}\hat{N} \tag{7.58}$$
$$\hat{U}_{\boldsymbol{v}} \hat{\boldsymbol{P}}_{\text{tot}} \hat{U}_{\boldsymbol{v}}^\dagger = \hat{\boldsymbol{P}}_{\text{tot}} + m\boldsymbol{v}\hat{N}. \tag{7.59}$$

From these relations, it is easy to see that the macroscopic expectation value $\langle\hat{\boldsymbol{P}}_{\text{tot}}\rangle_{\mathcal{F}}$ has to be equal to $\langle\hat{\boldsymbol{P}}_{\text{tot}} + m\boldsymbol{v}\hat{N}\rangle_{\mathcal{F}'}$. Further evaluation yields

$$\begin{aligned}\langle\hat{\boldsymbol{P}}_{\text{tot}}\rangle_{\mathcal{F}} &= \langle\hat{\boldsymbol{P}}_{\text{tot}} + m\boldsymbol{v}\hat{N}\rangle_{\mathcal{F}'} \\ &= \langle\hat{U}_{\boldsymbol{v}}^\dagger\hat{\boldsymbol{P}}_{\text{tot}}\hat{U}_{\boldsymbol{v}}\rangle_{\mathcal{F}'} = \frac{1}{Z}\text{tr}\left(\hat{U}_{\boldsymbol{v}}\hat{\boldsymbol{P}}_{\text{tot}}\hat{U}_{\boldsymbol{v}}^\dagger e^{-\beta\hat{H}}\right) = \frac{1}{Z}\text{tr}\left(\hat{\boldsymbol{P}}_{\text{tot}}\hat{U}_{\boldsymbol{v}}^\dagger e^{-\beta\hat{H}}\hat{U}_{\boldsymbol{v}}\right) \\ &= \frac{1}{Z}\text{tr}\left(\hat{\boldsymbol{P}}_{\text{tot}} e^{-\beta\hat{U}_{\boldsymbol{v}}^\dagger\hat{H}\hat{U}_{\boldsymbol{v}}}\right) = \frac{1}{Z}\text{tr}\left(\hat{\boldsymbol{P}}_{\text{tot}} e^{-\beta\hat{H}_{\boldsymbol{v}}}\right),\end{aligned} \tag{7.60}$$

where we used the invariance of the trace under cyclic permutations in the fourth equality and defined $\hat{H}_{\boldsymbol{v}} = \hat{U}_{\boldsymbol{v}}^\dagger\hat{H}\hat{U}_{\boldsymbol{v}}$. The identity $\hat{U}_{\boldsymbol{v}}^\dagger e^{-\beta\hat{H}}\hat{U}_{\boldsymbol{v}} = e^{-\beta\hat{U}_{\boldsymbol{v}}^\dagger\hat{H}\hat{U}_{\boldsymbol{v}}}$ can be shown by expanding the exponential and using the unitarity of U. By definition, the normal part of the system yields a classical momentum in a statistical average. Thereby, the expectation value of the total momentum must be equal to

$$\rho_n N m\boldsymbol{v} = \frac{1}{Z}\text{tr}\left(\hat{\boldsymbol{P}}_{\text{tot}} e^{-\beta\hat{H}_{\boldsymbol{v}}}\right) \tag{7.61}$$

with the normal liquid fraction ρ_n. Next, have a look at

$$\boldsymbol{\nabla}_{\boldsymbol{v}}\hat{H}_{\boldsymbol{v}} = \boldsymbol{\nabla}_{\boldsymbol{v}}(\hat{U}_{\boldsymbol{v}}^\dagger\hat{H}\hat{U}_{\boldsymbol{v}}) = (\boldsymbol{\nabla}_{\boldsymbol{v}}\hat{U}_{\boldsymbol{v}}^\dagger)\hat{H}\hat{U}_{\boldsymbol{v}} + \hat{U}_{\boldsymbol{v}}^\dagger\hat{H}(\boldsymbol{\nabla}_{\boldsymbol{v}}\hat{U}_{\boldsymbol{v}}) \tag{7.62}$$

$$= im\sum_{n=1}^{N}\hat{U}_{\boldsymbol{v}}^{\dagger}\hat{\boldsymbol{r}}_n\hat{H}\hat{U}_{\boldsymbol{v}} - im\sum_{n=1}^{N}\hat{U}_{\boldsymbol{v}}^{\dagger}\hat{H}\hat{\boldsymbol{r}}_n\hat{U}_{\boldsymbol{v}} = im\sum_{n=1}^{N}\hat{U}_{\boldsymbol{v}}^{\dagger}[\hat{\boldsymbol{r}}_n,\hat{H}]\hat{U}_{\boldsymbol{v}}.$$

The commutator is evaluated with the help of the canonical commutation relations as $[\hat{\boldsymbol{r}}_n,\hat{H}] = \frac{i}{m}\hat{\boldsymbol{p}}_n$. This means that the gradient of $\hat{H}_{\boldsymbol{v}}$ is

$$\boldsymbol{\nabla}_{\boldsymbol{v}}\hat{H}_{\boldsymbol{v}} = -\hat{U}_{\boldsymbol{v}}^{\dagger}\sum_{n=1}^{N}\hat{\boldsymbol{p}}_n\hat{U}_{\boldsymbol{v}} = -\hat{U}_{\boldsymbol{v}}^{\dagger}\hat{\boldsymbol{P}}_{\mathrm{tot}}\hat{U}_{\boldsymbol{v}} = -\hat{\boldsymbol{P}}_{\mathrm{tot}} + m\boldsymbol{v}\hat{N}. \tag{7.63}$$

We can substitute this expression into Eq. (7.61):

$$\begin{aligned}\rho_n N m\boldsymbol{v} &= \frac{1}{Z}\mathrm{tr}\left((-\boldsymbol{\nabla}_{\boldsymbol{v}}\hat{H}_{\boldsymbol{v}} + m\boldsymbol{v}\hat{N})e^{-\beta\hat{H}_{\boldsymbol{v}}}\right) \\ &= -\frac{1}{Z}\mathrm{tr}\left(\boldsymbol{\nabla}_{\boldsymbol{v}}\hat{H}_{\boldsymbol{v}}e^{-\beta\hat{H}_{\boldsymbol{v}}}\right) + m\boldsymbol{v}\frac{1}{Z}\mathrm{tr}\left(\hat{N}e^{-\beta\hat{H}_{\boldsymbol{v}}}\right) \\ &= \frac{1}{\beta Z}\boldsymbol{\nabla}_{\boldsymbol{v}}\mathrm{tr}\left(e^{-\beta\hat{H}_{\boldsymbol{v}}}\right) + m\boldsymbol{v}\frac{1}{Z}\mathrm{tr}\left(\hat{N}e^{-\beta\hat{H}_{\boldsymbol{v}}}\right) \\ &= \frac{1}{\beta Z}\boldsymbol{\nabla}_{\boldsymbol{v}}Z_{\boldsymbol{v}} + m\boldsymbol{v}\frac{1}{Z}\mathrm{tr}\left(\hat{N}e^{-\beta\hat{H}_{\boldsymbol{v}}}\right),\end{aligned} \tag{7.64}$$

where we defined $Z_{\boldsymbol{v}} = \mathrm{tr}(e^{-\beta\hat{H}_{\boldsymbol{v}}})$. We now take the derivative with respect to $\boldsymbol{v}$ on both sides:

$$\begin{aligned}\boldsymbol{\nabla}_{\boldsymbol{v}}\cdot(\rho_n N m\boldsymbol{v}) &= \rho_n N m d + (\boldsymbol{\nabla}_{\boldsymbol{v}}\rho_n)N m\boldsymbol{v} \\ &= \frac{1}{\beta Z}\boldsymbol{\nabla}_{\boldsymbol{v}}^2 Z_{\boldsymbol{v}} + md\frac{1}{Z}\mathrm{tr}\left(\hat{N}e^{-\beta\hat{H}_{\boldsymbol{v}}}\right) + m\boldsymbol{v}\frac{1}{Z}\mathrm{tr}\left(\hat{N}e^{-\beta\hat{H}_{\boldsymbol{v}}}(-\beta\boldsymbol{\nabla}_{\boldsymbol{v}}\hat{H}_{\boldsymbol{v}})\right).\end{aligned} \tag{7.65}$$

Taking the limit $\boldsymbol{v}\to 0$ on both sides and noticing that $\lim_{\boldsymbol{v}\to 0}\left[m\boldsymbol{v}\frac{1}{Z}\mathrm{tr}\left(\hat{N}e^{-\beta\hat{H}_{\boldsymbol{v}}}(-\beta\boldsymbol{\nabla}_{\boldsymbol{v}}\hat{H}_{\boldsymbol{v}})\right)\right] = 0$ and $\lim_{\boldsymbol{v}\to 0}\hat{H}_{\boldsymbol{v}} = \hat{H}$ yields

$$\begin{aligned}\rho_n N m d &= \frac{1}{\beta Z}\lim_{\boldsymbol{v}\to 0}\boldsymbol{\nabla}_{\boldsymbol{v}}^2 Z_{\boldsymbol{v}} + md\frac{1}{Z}\mathrm{tr}\left(\hat{N}e^{-\beta\hat{H}}\right) \\ &= \frac{1}{\beta Z}\lim_{\boldsymbol{v}\to 0}\boldsymbol{\nabla}_{\boldsymbol{v}}^2 Z_{\boldsymbol{v}} + mdN.\end{aligned} \tag{7.66}$$

If the superfluid fraction is denoted by ρ_s, the equation $\rho_n + \rho_s = 1$ can be used to write

$$\rho_s = -\frac{1}{\beta Z N m d}\lim_{\boldsymbol{v}\to 0}\boldsymbol{\nabla}_{\boldsymbol{v}}^2 Z_{\boldsymbol{v}}. \tag{7.67}$$

Now, we have to find an appropriate decomposition of $Z_{\boldsymbol{v}}$ in the PIMC language[5]. As $Z_{\boldsymbol{v}} = \mathrm{tr}(e^{-\beta\hat{H}_{\boldsymbol{v}}})$, we rewrite

$$Z_{\boldsymbol{v}} = \frac{1}{N!}\sum_{\mathcal{P}}\int \mathrm{d}\boldsymbol{R}\,\mathrm{d}\boldsymbol{R}_1\,\mathrm{d}\boldsymbol{R}_2\ldots\mathrm{d}\boldsymbol{R}_{M-1}\langle\boldsymbol{R}|e^{-\epsilon\hat{H}_{\boldsymbol{v}}}|\boldsymbol{R}_1\rangle\langle\boldsymbol{R}_1|e^{-\epsilon\hat{H}_{\boldsymbol{v}}}|\boldsymbol{R}_2\rangle\ldots\langle\boldsymbol{R}_{M-1}|e^{-\epsilon\hat{H}_{\boldsymbol{v}}}|\mathcal{P}\boldsymbol{R}\rangle. \tag{7.68}$$

in analogy to the derivation of Z in Eq. (7.6). We further note that $\hat{U}_{\boldsymbol{v}}^{\dagger}\hat{V}\hat{U}_{\boldsymbol{v}} = \hat{V}$ and

$$\hat{U}_{\boldsymbol{v}}^{\dagger}\hat{T}\hat{U}_{\boldsymbol{v}} = \hat{U}_{\boldsymbol{v}}^{\dagger}\sum_{i=1}^{N}\frac{\hat{\boldsymbol{p}}_i^2}{2m}\hat{U}_{\boldsymbol{v}} = \frac{1}{2m}\sum_{i=1}^{N}\hat{U}_{\boldsymbol{v}}^{\dagger}\hat{\boldsymbol{p}}_i\hat{U}_{\boldsymbol{v}}\hat{U}_{\boldsymbol{v}}^{\dagger}\hat{\boldsymbol{p}}_i\hat{U}_{\boldsymbol{v}} = \frac{1}{2m}\sum_{i=1}^{N}(\hat{\boldsymbol{p}}_i - m\boldsymbol{v})(\hat{\boldsymbol{p}}_i - m\boldsymbol{v}). \tag{7.69}$$

[5]In this derivation, we treat distinguishable particles. The extension to identical bosons is straightforward.

This implies that

$$\hat{H}_{\boldsymbol{v}} = \frac{1}{2m}\sum_{i=1}^{N}(\hat{\boldsymbol{p}}_i - m\boldsymbol{v})(\hat{\boldsymbol{p}}_i - m\boldsymbol{v}) + \hat{V} \equiv \hat{T}' + \hat{V}. \tag{7.70}$$

If this is plugged into the matrix elements of Eq. (7.68), it follows that

$$\begin{aligned}\langle \boldsymbol{R}_{i-1}|e^{-\epsilon\hat{H}_{\boldsymbol{v}}}|\boldsymbol{R}_i\rangle &= \langle \boldsymbol{R}_{i-1}|e^{-\epsilon\hat{T}'}e^{-\epsilon\hat{V}}|\boldsymbol{R}_i\rangle + \mathcal{O}(\epsilon^2) = \\ &= \langle \boldsymbol{R}_{i-1}|e^{-\epsilon\hat{T}'}|\boldsymbol{R}_i\rangle e^{-\epsilon V(\boldsymbol{R}_i)} + \mathcal{O}(\epsilon^2).\end{aligned} \tag{7.71}$$

The evaluation of the kinetic matrix element yields

$$\begin{aligned}\langle \boldsymbol{R}_{i-1}|e^{-\epsilon\hat{T}'}|\boldsymbol{R}_i\rangle =& \frac{1}{V^{2N}}\sum_{\boldsymbol{P}_1,\boldsymbol{P}_2}\langle \boldsymbol{R}_{i-1}|\boldsymbol{P}_1\rangle\langle \boldsymbol{P}_1|e^{-\epsilon\hat{T}'}|\boldsymbol{P}_2\rangle\langle \boldsymbol{P}_2|\boldsymbol{R}_i\rangle \\ =& \frac{1}{V^{2N}}\sum_{\boldsymbol{P}_1,\boldsymbol{P}_2} e^{i\boldsymbol{R}_{i-1}\boldsymbol{P}_1}\langle \boldsymbol{P}_1|e^{-\epsilon\hat{T}'}|\boldsymbol{P}_2\rangle e^{-i\boldsymbol{P}_2\boldsymbol{R}_i} \\ =& \frac{1}{V^{2N}}\sum_{\boldsymbol{P}_1,\boldsymbol{P}_2} e^{i\boldsymbol{R}_{i-1}\boldsymbol{P}_1}V\delta_{\boldsymbol{P}_1,\boldsymbol{P}_2}e^{-\epsilon T'(\boldsymbol{P}_1)}e^{-i\boldsymbol{P}_2\boldsymbol{R}_i} \\ =& \frac{1}{V^{N}}\sum_{\boldsymbol{P}} e^{-i\boldsymbol{P}(\boldsymbol{R}_i-\boldsymbol{R}_{i-1})}e^{-\frac{\epsilon}{2m}\left(\boldsymbol{P}^2-2m\boldsymbol{V}\boldsymbol{P}+Nm^2\boldsymbol{v}^2\right)} \\ =& \frac{1}{V^{N}}\sum_{\boldsymbol{P}} e^{-i\boldsymbol{P}(\boldsymbol{R}_i-\boldsymbol{R}_{i-1}-i\epsilon\boldsymbol{V})}e^{-\frac{\epsilon}{2m}\boldsymbol{P}^2}e^{-\frac{\epsilon}{2}Nm\boldsymbol{v}^2} \\ =& \left(\frac{m}{2\pi\epsilon}\right)^{\frac{Nd}{2}}\sum_{\boldsymbol{W}} e^{-\frac{m(\boldsymbol{R}_i-\boldsymbol{R}_{i-1}+\boldsymbol{W}-i\epsilon\boldsymbol{V})^2}{2\epsilon}}e^{-\frac{\epsilon}{2}Nm\boldsymbol{v}^2} \\ =& \left(\frac{m}{2\pi\epsilon}\right)^{\frac{Nd}{2}}\sum_{\boldsymbol{W}} e^{-\frac{m(\boldsymbol{R}_i-\boldsymbol{R}_{i-1}+\boldsymbol{W})^2}{2\epsilon}}e^{im\boldsymbol{V}(\boldsymbol{R}_i-\boldsymbol{R}_{i-1}+\boldsymbol{W})}e^{\frac{Nm\epsilon\boldsymbol{v}^2}{2\epsilon}}e^{-\frac{\epsilon}{2}Nm\boldsymbol{v}^2} \\ =& \left(\frac{m}{2\pi\epsilon}\right)^{\frac{Nd}{2}}\sum_{\boldsymbol{W}} e^{-\frac{m(\boldsymbol{R}_i-\boldsymbol{R}_{i-1}+\boldsymbol{W})^2}{2\epsilon}}e^{im\boldsymbol{V}(\boldsymbol{R}_i-\boldsymbol{R}_{i-1}+\boldsymbol{W})}\end{aligned} \tag{7.72}$$

where the Poisson summation formula is used (see Eq. (7.3)) and $\boldsymbol{V}$ is defined as the composite vector of N single vectors $\boldsymbol{v}$. The final decomposition of the partition function gives

$$Z_{\boldsymbol{v}} = \frac{1}{N!}\sum_{\mathcal{P}}\left(\prod_{t=0}^{M-1}\int \mathrm{d}\boldsymbol{R}_t\sum_{\boldsymbol{W}_t}\right)\left(\prod_{t=0}^{M-1}\left(\frac{m}{2\pi\epsilon}\right)^{\frac{Nd}{2}} e^{-\frac{m(\boldsymbol{R}_{t+1}-\boldsymbol{R}_t+\boldsymbol{W}_t)^2}{2\epsilon}}e^{im\boldsymbol{V}(\boldsymbol{R}_i-\boldsymbol{R}_{i-1}+\boldsymbol{W}_t)}e^{-\epsilon V(\boldsymbol{R}_t)}\right). \tag{7.73}$$

If the product of all timeslices is taken, all $\boldsymbol{R}$ coordinates will drop out of $e^{im\boldsymbol{V}(\boldsymbol{R}_i-\boldsymbol{R}_{i-1}+\boldsymbol{W}_t)}$ because each position is occurring two times with opposite signs. Permutations would not change this fact as the product $\boldsymbol{V}\boldsymbol{R}$ is invariant under particle exchange. This means that

$$\begin{aligned}\frac{Z_{\boldsymbol{v}}}{Z} =& \frac{1}{Z}\frac{1}{N!}\sum_{\mathcal{P}}\left(\prod_{t=0}^{M-1}\int \mathrm{d}\boldsymbol{R}_t\sum_{\boldsymbol{W}_t}\right)\left(\prod_{t=0}^{M-1}\left(\frac{m}{2\pi\epsilon}\right)^{\frac{Nd}{2}} e^{-\frac{m(\boldsymbol{R}_{t+1}-\boldsymbol{R}_t+\boldsymbol{W}_t)^2}{2\epsilon}}e^{-\epsilon V(\boldsymbol{R}_t)}\right)\left(\prod_{t=0}^{M-1}e^{im\boldsymbol{V}\boldsymbol{W}_t}\right) \\ =& \left\langle\prod_{t=0}^{M-1}e^{im\boldsymbol{V}\boldsymbol{W}_t}\right\rangle_Z,\end{aligned} \tag{7.74}$$

where the ensemble average is taken with respect to Z. This expression makes it easy to compute the derivative that is needed for the superfluid density:

$$\begin{aligned}\rho_s &= -\frac{1}{\beta Z N m d}\lim_{\boldsymbol{v}\to 0}\boldsymbol{\nabla}_{\boldsymbol{v}}^2 Z_{\boldsymbol{v}} \\ &= -\frac{1}{\beta N m d}\lim_{\boldsymbol{v}\to 0}\left\langle -m^2\left(\sum_{t=0}^{M-1}\boldsymbol{W}_t\right)\left(\prod_{t=0}^{M-1}e^{im\boldsymbol{V}\boldsymbol{W}_t}\right)\right\rangle_Z \\ &= \frac{m}{\beta N d}\left\langle\sum_{t=0}^{M-1}\boldsymbol{W}_t\right\rangle_Z .\end{aligned} \tag{7.75}$$

This expression is commonly referred to as winding estimator [99]. The evaluation of $\sum_{t=0}^{M-1}\boldsymbol{W}_t$ is nothing but a summation over all particle trajectories that leave the box and use periodic boundary conditions. It is remarkable that the superfluid density, a quantity that is originating from a moving system, can be extracted from the static partition function.

7.4.3. Pair correlation function

The pair correlation function measures the probability that two particles are separated by a certain distance in the box. It is defined as [100]

$$\begin{aligned}g(\boldsymbol{r}',\boldsymbol{r}'') &= \frac{V^2}{N(N-1)}\sum_{i=1}^{N}\sum_{j=1,j\neq i}^{N}\left\langle\delta(\boldsymbol{r}_i-\boldsymbol{r}')\delta(\boldsymbol{r}_j-\boldsymbol{r}'')\right\rangle \\ &\approx \frac{V^2}{N^2}\sum_{i\neq j}\left\langle\delta(\boldsymbol{r}_i-\boldsymbol{r}')\delta(\boldsymbol{r}_j-\boldsymbol{r}'')\right\rangle\end{aligned} \tag{7.76}$$

where we choose a normalization which ensures that $g(\boldsymbol{r}',\boldsymbol{r}'')=1$ for a noninteracting system and approximate $N\approx N-1$ for large N in the second line. The pair correlation function is sometimes also referred to as radial distribution function.

For translationally invariant systems, g depends only on the relative distance $\boldsymbol{r}=\boldsymbol{r}_1-\boldsymbol{r}_2$. This allows to rewrite $g(r)$ as an average over all pairs of points in the simulation box that are separated by $\boldsymbol{r}$, i.e.,

$$\begin{aligned}g(\boldsymbol{r}) &\equiv \frac{1}{V}\int \mathrm{d}\boldsymbol{r}'\,\mathrm{d}\boldsymbol{r}''\; g(\boldsymbol{r}',\boldsymbol{r}'')\;\delta\left(\boldsymbol{r}-(\boldsymbol{r}'-\boldsymbol{r}'')\right) \\ &= \frac{V}{N^2}\sum_{i\neq j}\int \mathrm{d}\boldsymbol{r}'\,\mathrm{d}\boldsymbol{r}''\;\left\langle\delta(\boldsymbol{r}_i-\boldsymbol{r}')\delta(\boldsymbol{r}_j-\boldsymbol{r}'')\right\rangle\delta\left(\boldsymbol{r}-(\boldsymbol{r}'-\boldsymbol{r}'')\right) \\ &= \left\langle\frac{V}{N^2}\sum_{i\neq j}\delta(\boldsymbol{r}_i-\boldsymbol{r}_j-\boldsymbol{r})\right\rangle .\end{aligned} \tag{7.77}$$

Expanding this expectation value in the usual PIMC decomposition is particularly simple as it is diagonal in position space. This means that one of two following strategies can be applied:

1. Place the observable on one preselected timeslice of Eq. (7.17). A measurement consists in evaluating the current value of the bracketed expression on this timeslice.

2. Alternatively, the observable can be distributed among all timeslices. This requires that a global factor $1/M$ be introduced for the pair correlation function.

It is important to measure particle distances with respect to periodic boundary conditions, meaning that the shortest distance between two particles has to be chosen. The finite size of

the simulation box and periodic boundary conditions imply that only measurements of the pair correlation function up to distances $|\boldsymbol{r}| = \min(L_1, \ldots, L_d)/2$ are giving meaningful results. The relation $\lim_{|\boldsymbol{r}|\to 0} g(\boldsymbol{r}) = 1$ can help to determine whether the system size is chosen large enough so that no important features of the pair correlation function are lost.

Finally, if only $g(|\boldsymbol{r}|)$ is of interest (which is the case in isotropic systems), the Monte Carlo estimator of the pair correlation function can be rewritten by averaging over volume shells of width Δr:

$$g(r_i) = \frac{\int_{r_i-\Delta r/2}^{r_i+\Delta r/2} \mathrm{d}r' r'^2 \int_0^{2\pi} \mathrm{d}\phi \int_{-1}^{1} \mathrm{d}\cos\theta \; g\left(\boldsymbol{r} = (r', \phi, \theta)\right)}{\frac{4}{3}\pi\left((r_i + \Delta r/2)^3 - (r_i - \Delta r/2)^3\right)} \tag{7.78}$$

In this result, $r_i = 2i\Delta r$ with integer i. A similar expression can be derived for two-dimensional systems.

7.4.4. Static structure factor

The static structure factor is defined as

$$S(\boldsymbol{q}) = 1 + \frac{N}{V}\int \mathrm{d}\boldsymbol{r} \; [g(\boldsymbol{r}) - 1] e^{-i\boldsymbol{q}\boldsymbol{r}}. \tag{7.79}$$

Plugging in the definition of $g(\boldsymbol{r})$, Eq. (7.77), this can be rewritten as [101]

$$S(\boldsymbol{q}) = \left\langle \frac{1}{N}\left(\sum_{j=1}^{N} e^{-i\boldsymbol{q}\boldsymbol{r}_j}\right)\left(\sum_{k=1}^{N} e^{i\boldsymbol{q}\boldsymbol{r}_k}\right)\right\rangle - N\delta_{\boldsymbol{q},\boldsymbol{0}}. \tag{7.80}$$

For $\boldsymbol{q} \neq \boldsymbol{0}$, the $\delta_{\boldsymbol{q},\boldsymbol{0}}$ factor can be omitted. Rewriting the exponentials in terms of trigonometric functions yields

$$S(\boldsymbol{q}) = \left\langle \frac{1}{N}\left|\sum_{j=1}^{N}\left(\cos\left(\boldsymbol{q}\boldsymbol{r}_j\right) - i\sin\left(\boldsymbol{q}\boldsymbol{r}_j\right)\right)\right|^2\right\rangle = \left\langle \frac{1}{N}\left|\sum_{j=1}^{N}\cos\left(\boldsymbol{q}\boldsymbol{r}_j\right)\right|^2 + \frac{1}{N}\left|\sum_{j=1}^{N}\sin\left(\boldsymbol{q}\boldsymbol{r}_j\right)\right|^2\right\rangle. \tag{7.81}$$

Broadly speaking, the static structure factor gives a Fourier analysis of the pair correlation function and makes it easy to analyze if a system crystallizes or not. For low momenta, it yields $\lim_{|\boldsymbol{q}|\to 0} S(\boldsymbol{q}) = 0$, while $\lim_{|\boldsymbol{q}|\to\infty} S(\boldsymbol{q}) = 1$, as shown in Ref. [101]. In isotropic systems, it suffices to measure the static structure factor on a discrete grid of points of one of the coordinate axes.

7.4.5. Green's functions

After discussing diagonal observables, we turn to observables measured in the worm sector. Here, we assume that the simulation is grand-canonical. We assume finite-temperature and define $\hat{K} = \hat{H} - \mu\hat{N}$. The equilibrium Green's function is defined as [89]

$$\begin{aligned} G(\tau, \boldsymbol{x}_1, \boldsymbol{x}_2) &\equiv \frac{1}{Z} g(\tau, \boldsymbol{x}_1, \boldsymbol{x}_2) \equiv \left\langle \mathcal{T}\left\{\hat{\psi}(\boldsymbol{x}_1, \tau)\hat{\psi}^\dagger(\boldsymbol{x}_2, 0)\right\}\right\rangle \\ &= \frac{1}{Z}\mathrm{tr}\left(\mathcal{T}\left\{\hat{\psi}(\boldsymbol{x}_1, \tau)\hat{\psi}^\dagger(\boldsymbol{x}_2, 0)e^{-\beta\hat{K}}\right\}\right), \end{aligned} \tag{7.82}$$

where $\hat{\psi}^{(\dagger)}(\boldsymbol{r}, \tau)$ is the annihilation (creation) operator of a boson at imaginary time τ and position $\boldsymbol{r}$. $\mathcal{T}$ denotes the time-ordering operator. For simplicity, we will restrict ourselves to

$\tau > 0$ which can be straightforwardly translated into $\tau < 0$ through the commutation relations of $\hat{\psi}$ and $\hat{\psi}^\dagger$. We already exploited the fact that the Green's function only depends on one relative time coordinate. ψ is related to the symmetrized position states by

$$|\boldsymbol{\mathcal{R}}^{(N)}\rangle = \frac{1}{\sqrt{N!}}\hat{\psi}^\dagger(\boldsymbol{r}_1)\hat{\psi}^\dagger(\boldsymbol{r}_2)\dots\hat{\psi}^\dagger(\boldsymbol{r}_N)|0\rangle, \tag{7.83}$$

where $|0\rangle$ is the vacuum. Plugging in the explicit time dependence of the Heisenberg field operators $\hat{\psi}(\boldsymbol{r},\tau) = e^{\tau\hat{K}}\hat{\psi}(\boldsymbol{r},0)e^{-\tau\hat{K}}$ and using the invariance of the trace under cyclic permutations yields

$$\begin{aligned} g(\tau,\boldsymbol{x}_1,\boldsymbol{x}_2) &= \mathrm{tr}\left(e^{\tau\hat{K}}\hat{\psi}(\boldsymbol{x}_1)e^{-\tau\hat{K}}\hat{\psi}^\dagger(\boldsymbol{x}_2)e^{-\beta\hat{K}}\right) \\ &= \mathrm{tr}\left(e^{-\beta\hat{K}}e^{\tau\hat{K}}\hat{\psi}(\boldsymbol{x}_1)e^{-\tau\hat{K}}\hat{\psi}^\dagger(\boldsymbol{x}_2)\right). \end{aligned} \tag{7.84}$$

Now, the trace can be evaluated in a many-body basis and a complete set of states is inserted as

$$\begin{aligned} &g(\tau,\boldsymbol{x}_1,\boldsymbol{x}_2) = \\ &= \sum_{N=0}^{\infty}\int \mathrm{d}\boldsymbol{R}^{(N)}\,\mathrm{d}\boldsymbol{R}'^{(N)}\langle\boldsymbol{\mathcal{R}}^{(N)}|e^{-(\beta-\tau)\hat{K}}|\boldsymbol{\mathcal{R}}'^{(N)}\rangle\langle\boldsymbol{\mathcal{R}}'^{(N)}|\hat{\psi}(\boldsymbol{x}_1)e^{-\tau\hat{K}}\hat{\psi}^\dagger(\boldsymbol{x}_2)|\boldsymbol{\mathcal{R}}^{(N)}\rangle \\ &= \sum_{N=0}^{\infty}\int \mathrm{d}\boldsymbol{R}^{(N)}\,\mathrm{d}\boldsymbol{R}'^{(N)}\langle\boldsymbol{\mathcal{R}}^{(N)}|e^{-(\beta-\tau)\hat{K}}|\boldsymbol{\mathcal{R}}'^{(N)}\rangle(N+1)\langle\boldsymbol{\mathcal{R}}'^{(N)},\boldsymbol{x}_1|e^{-\tau\hat{K}}|\boldsymbol{\mathcal{R}}^{(N)},\boldsymbol{x}_2\rangle \\ &= \sum_{N=0}^{\infty}\int \mathrm{d}\boldsymbol{R}^{(N)}\,\mathrm{d}\boldsymbol{R}'^{(N)}\langle\boldsymbol{\mathcal{R}}^{(N)}|e^{-(\beta-\tau)\hat{H}}|\boldsymbol{\mathcal{R}}'^{(N)}\rangle(N+1)\langle\boldsymbol{\mathcal{R}}'^{(N)},\boldsymbol{x}_1|e^{-\tau\hat{H}}|\boldsymbol{\mathcal{R}}^{(N)},\boldsymbol{x}_2\rangle e^{\tau\mu+\beta\mu N}. \end{aligned} \tag{7.85}$$

The notation $|\boldsymbol{\mathcal{R}},\boldsymbol{r}\rangle$ labels the symmetrized state with one particle at $\boldsymbol{r}$ and the other particles positions in the set $\boldsymbol{\mathcal{R}}$. The matrix elements $\langle\boldsymbol{\mathcal{R}}^{(N)}|e^{-(\beta-\tau)\hat{H}}|\boldsymbol{\mathcal{R}}'^{(N)}\rangle$ and $\langle\boldsymbol{\mathcal{R}}'^{(N)},\boldsymbol{x}_1|e^{-\tau\hat{H}}|\boldsymbol{\mathcal{R}}^{(N)},\boldsymbol{x}_2\rangle$ can be expanded by introducing timeslices. In the worldline picture, they have the following interpretation: $\langle\boldsymbol{\mathcal{R}}^{(N)}|e^{-(\beta-\tau)\hat{H}}|\boldsymbol{\mathcal{R}}'^{(N)}\rangle$ is an off-diagonal matrix element of $(N+1)$ particles which is propagating with imaginary time length $(\beta-\tau)$, whereas $\langle\boldsymbol{\mathcal{R}}'^{(N)},\boldsymbol{x}_1|e^{-\tau\hat{H}}|\boldsymbol{\mathcal{R}}^{(N)},\boldsymbol{x}_2\rangle$ describes a system of N particles that propagates in an imaginary time interval τ. This is exactly what the worm algorithm delivers: One part of the system is containing $(N+1)$ particles per timeslice, the other part has N particles per timeslice. The two sectors are separated by the dangling world line ends, $\mathcal{I}$ and $\mathcal{M}$ – these are the positions that correspond to the arguments $\boldsymbol{x}_1$ and $\boldsymbol{x}_2$ of the Green's function, Eq. (7.82), where particles are being created/annihilated. Expanding $|\boldsymbol{\mathcal{R}}^{(N)}\rangle$ and $|\boldsymbol{\mathcal{R}}'^{(N)}\rangle$ into regular, nonsymmetrized states now results in a factor $\frac{1}{(N+1)!}$ coming from the normalization of $|\boldsymbol{\mathcal{R}}^{(N)},\boldsymbol{r}_2\rangle$ as defined in Eq. (7.10) which combines nicely with the $(N+1)$ term:

$$\sum_{N=0}^{\infty}\sum_{\mathcal{P}}\frac{1}{N!}\int \mathrm{d}\boldsymbol{R}^{(N)}\,\mathrm{d}\boldsymbol{R}'^{(N)}\langle\boldsymbol{R}^{(N)}|e^{-(\beta-\tau)\hat{H}}|\boldsymbol{R}'^{(N)}\rangle\langle\boldsymbol{R}'^{(N)},\boldsymbol{x}_1|e^{-\tau\hat{H}}|\mathcal{P}(\boldsymbol{R}^{(N)},\boldsymbol{x}_2)\rangle e^{\mu(\tau+\beta)N}, \tag{7.86}$$

where $|\mathcal{P}(\boldsymbol{R}^{(N)},\boldsymbol{x}_2)\rangle$ denotes the permutation $\mathcal{P}$ of the state $|\boldsymbol{r}_1\dots\boldsymbol{r}_N\boldsymbol{x}_2\rangle$.

In the worm sector, the simulation generates the sum

$$\begin{aligned} \sum_{N,\mathcal{P}}\sum_{t=1}^{M}\frac{\mathcal{C}}{(N+1)!}\int \mathrm{d}\boldsymbol{R}_0^{(N)}\,\mathrm{d}\boldsymbol{R}_1^{(N)}\dots\,\mathrm{d}\boldsymbol{R}_{M-t}^{(N)}\,\mathrm{d}\boldsymbol{R}_{M-t+1}^{(N+1)}\dots\,\mathrm{d}\boldsymbol{R}_{M-1}^{(N+1)}\,\mathrm{d}\boldsymbol{r}_{\mathcal{M}}\,\mathrm{d}\boldsymbol{r}_{\mathcal{I}}\;e^{\mu(t+\beta)N} \\ \rho\left(\boldsymbol{R}_0^{(N)},\boldsymbol{R}_1^{(N)},\epsilon\right)\dots\;\rho\left(\boldsymbol{R}_{M-t-1}^{(N)},\boldsymbol{R}_{M-t}^{(N)},\epsilon\right)\rho\left(\boldsymbol{R}'^{(N+1)}_{M-t},\boldsymbol{R}_{M-t+1}^{(N+1)},\epsilon\right) \end{aligned}$$

$$\ldots \ \rho\left(\boldsymbol{R}_{M-1}^{(N+1)}, \mathcal{P}\boldsymbol{R'}_{0}^{(N+1)}, \epsilon\right) \tag{7.87}$$

with $\boldsymbol{R'}_{M-t}^{(N+1)} = (\boldsymbol{R}_{M-t}^{(N)}, \boldsymbol{r}_{\mathcal{M}})$ and $\boldsymbol{R'}_{0}^{(N+1)} = (\boldsymbol{R}_{0}^{(N)}, \boldsymbol{r}_{\mathcal{I}})$. Several adjustments need to be taken into account when measuring with this expression:

- The expression (7.87) has to be divided by $\mathcal{C}$ in order to remove this arbitrary parameter.

- Within the worm algorithm framework, one samples the sum of partition sector and worm sector. It is necessary to formalize this intuitive picture by introducing the generalized partition function Z_{tot} of the whole sampling space and the partition function of the worm sector Z'. They are linked by $Z_{\text{tot}} = Z + Z'$. Up to now, we measured diagonal quantities corresponding to Z. Naturally, these measurements were only performed on diagonal configurations, which made the averaging very easy: One simply had to divide by the number of measurements in the diagonal sector.

  For the Green's function $G = g/Z$, this is more complicated, as the numerator and the denominator live in different sectors of Z_{tot}. A way out is given by measuring two additional observables $\langle \delta^Z \rangle_{Z_{\text{tot}}}$ and $\langle \delta^{Z'} \rangle_{Z_{\text{tot}}}$, where $\delta^Z = 1$ in the diagonal sector and $\delta^Z = 0$ otherwise, while $\delta^{Z'}$ is defined the other way around. These observables are measured after every Monte Carlo move. Now it is possible to access G:

$$G = \frac{g}{Z} = \frac{g}{Z_{\text{tot}} \frac{Z}{Z_{\text{tot}}}} = \frac{g}{Z_{\text{tot}} \langle \delta^Z \rangle_{Z_{\text{tot}}}} = \frac{\langle g \rangle_{Z'} Z'}{Z_{\text{tot}} \langle \delta^Z \rangle_{Z_{\text{tot}}}} = \frac{\langle g \rangle_{Z'} \langle \delta^{Z'} \rangle_{Z_{\text{tot}}}}{\langle \delta^Z \rangle_{Z_{\text{tot}}}}. \tag{7.88}$$

- It is important to emphasize that Eq. (7.87) requires that the worldline containing $\mathcal{M}$ be labeled with the highest possible particle label, $(N+1)$. To raise efficiency, it is beneficial to abandon this requirement and allow arbitrary particle labels of $\mathcal{M}$ for measurements, thus enhancing the estimator by $(N+1)$ – however, note that this is exactly the missing factor to balance the factorials of Eq. (7.86) and Eq. (7.87).

- Eq. (7.87) assumes that the part of the worm sector with $(N+1)$ particles is put in the upper part of the x-τ diagram. This is not strictly what is sampled with the worm updates described above – the part with $(N+1)$ particles can be located on every timeslice as the configuration can be opened freely. This means that the worm sector is repeated M times with respect to the partition sector, thus an estimator for the Green's function has to be divided by M in the end. In the quartic approximation, this number is $M/2$ because the worm ends can only be on even timeslices.

In summary, a suitable estimator for G is given by

$$G(\tau, \boldsymbol{x}_1, \boldsymbol{x}_2) = \frac{\langle g \rangle_{Z'} \langle \delta^{Z'} \rangle_{Z_{\text{tot}}}}{\langle \delta^Z \rangle_{Z_{\text{tot}}}} \tag{7.89}$$

with

$$\langle g \rangle_{Z'} = \frac{1}{M\mathcal{C}} \left\langle \delta(\boldsymbol{x}_1 - \boldsymbol{r}_{\mathcal{M}}) \delta(\boldsymbol{x}_2 - \boldsymbol{r}_{\mathcal{I}}) \ \delta_{\tau, t\epsilon} \right\rangle_{Z'}. \tag{7.90}$$

In systems with translational invariance, the Green's function only depends on the relative distance $\boldsymbol{r} = \boldsymbol{x}_2 - \boldsymbol{x}_1$, while spherical symmetric systems allow radial binning. The implementation of these special cases works analogously to the pair correlation function. There are two special cases of the Green's function that will be discussed in the following.

One-body density matrix The one-body density matrix (or one-particle density matrix) measures the correlations between different positions in the simulation box at one instant in imaginary time. For a canonical simulation, it is defined [90] as $n(\boldsymbol{x}_1, \boldsymbol{x}_2) = \frac{V}{N} \left\langle \hat{\psi}(\boldsymbol{x}_1)\hat{\psi}^\dagger(\boldsymbol{x}_2) \right\rangle$. The normalization ensures that $n(\boldsymbol{x}, \boldsymbol{x}) = 1$. Extracting the one-body density matrix from G is straightforward

$$n(\boldsymbol{x}_1, \boldsymbol{x}_2) = \frac{V}{N} G(\beta^-, \boldsymbol{x}_1, \boldsymbol{x}_2). \tag{7.91}$$

Here, we have chosen β instead of 0 such that Eq. (7.87) remains valid. Note that $\langle g \rangle_{Z'} \langle \delta^{Z'} \rangle_{Z_{\text{tot}}}$ has to be adjusted to $\langle g \rangle_{Z''} \langle \delta^{Z''} \rangle_{Z_{\text{tot}}}$ for these measurements, where Z'' is the part of Z' with both worm ends on the same timeslice. Analyzing the spatial dependence of $n(\boldsymbol{x}_1, \boldsymbol{x}_2)$, it is possible to identify superfluid phases [89]. Additionally, the condensate fraction can be estimated in three dimensions.

Zero-momentum Green's function It is also possible to calculate the zero-momentum Green's function $G(\tau, \boldsymbol{p} = 0)$ from G by integrating over all positions:

$$G(\tau, \boldsymbol{p} = 0) = \int \mathrm{d}\boldsymbol{r}\ G(\tau, \boldsymbol{r}), \tag{7.92}$$

where $G(\tau, \boldsymbol{r}) = \frac{1}{V} \int \mathrm{d}\boldsymbol{x}_1\, \mathrm{d}\boldsymbol{x}_2 G(\tau, \boldsymbol{x}_1, \boldsymbol{x}_2) \delta(\boldsymbol{x}_1 - \boldsymbol{x}_2 - \boldsymbol{r})$. $G(\tau, \boldsymbol{r})$ is a very important quantity for understanding the algorithmic performance, since it gives detailed insight into the probabilitity of separating the worms with distance τ in imaginary time.

7.4.6. Exchanges

The last observable presented is the exchange cycle distribution, a very helpful measurement that gives feedback about the ability of the code to generate bosonic particle exchanges efficiently. For a given worldline, the length of the corresponding bosonic particle exchange cycle is defined by counting the number of times a worldline propagates from $\tau = 0$ to $\tau = \beta$ until it returns to its initial position. The number of involved worldlines gives the length of the particle exchange. This means that exchange lengths from 1 to N are possible. A measurement consists in selecting an arbitrary worldline and adding the corresponding exchange cycle length to a histogram.

7.5. Testing the algorithm

A general first step in computational physics problems consists in establishing the code's correctness and robustness. This can be achieved by several testing strategies. Unit tests are a standard way of controlling the behavior of small parts of the code base. However, the statistical nature of Monte Carlo makes it hard to apply this strategy without limiting the test to edge cases or modifying the code to make it deterministic.

Therefore, another strategy is applied: On the configurational level of the code, several properties of the simulation are defined and checked occasionally during the runs. These checks include:

- Test if all particles are still inside the simulation box.
- Test if each bead is correctly linked to its neighbors.
- Test if each particle is correctly assigned to its corresponding cell.

- Recalculate the energy and compare it with the subsequently updated value (this also checks a large part of the Metropolis weights).
- Check if the number of beads equals the number of particles times the number of slices.
- Recalculate windings and compare them with the subsequently updated values.

Every bug that is found in the code triggers another check that is supposed to prevent this bug in the future. Regarding the statistical part of the code, several test cases are written that simulate large portions of the code and compare the results with known analytical or numerical results. As these tests involve a considerable runtime, it is not possible to run them after every small modification.

7.5.1. Ideal bosons

The system of ideal bosons, a gas of noninteracting Bose particles, is easily accessible by analytic and simple numerical approaches. An exhaustive treatment is given in Ref. [4] from which we take our results for comparison. There are five tests using ideal bosons:

1. One canonical classical particle is put in a periodic box. This situation can be simulated by restricting the sampling to diagonal updates. The observed energy has to agree with results from the equipartition theorem.
2. One canonical boson is put in a periodic box. The result for the total energy is known analytically. The estimator should agree with this result within two sigma.
3. Two canonical distinguishable particles are put in a periodic box. The distinguishability is implemented by disallowing Reconnect. This should give the same energy per particle as test number 2.
4. Two canonical bosons are put in a periodic box. This energy can be calculated by computing the partition sum of the system [4].
5. 16 canonical bosons are put in a periodic box. This energy can be calculated as test number 4.

7.5.2. Weakly-interacting Bose gas

The weakly interacting Bose gas is, roughly speaking, a system dominated by kinetic energy with small potential contributions. At low temperatures, the potential interaction is described by a single parameter, the two-body scattering length. For our test, we use the Gaussian-core interaction which is specified in the next chapter with appropriate values of ϵ and σ. The results have to agree with Fig. 14 of Ref. [102]. Note that the energy-density has to be divided by T_c to be compared.

7.5.3. Helium

One of the main applications of PIMC is the simulation of ^{4}He. The corresponding potential resembles potentials of Lennard-Jones type and is conventionally described by the Aziz potential [89]. The helium test consists in reproducing Figs. 2.2 and 2.3 of Ref. [90].

8

Ground-state phase diagram of the Gaussian-core model

Chapter 8 presents results of PIMC simulations at low temperature of a 2D system of spin-zero bosons interacting via

$$V(r) = \epsilon \exp\left[-\frac{r^2}{2\sigma^2}\right]. \tag{8.1}$$

This potential is called Gaussian-core potential [37] with parameters ϵ and σ. In the absence of disorder, frustration, or an external potential, the ground state of interacting scalar Bose systems like this is always ordered, i.e., a well-defined symmetry of the Hamiltonian is spontaneously broken. Only two types of order are believed to be possible, namely, crystalline order, which breaks translational symmetry, or off-diagonal long-range order (superfluid), in which case the global $U(1)$ symmetry is broken.

Normally, only one of these two types of order is present, as a result of the competition between particle interactions, typically favoring crystallization, and quantum delocalization, promoting superfluidity. Such is the case for ^{4}He, featuring either a superfluid or an insulating crystal in the ground state, depending on the external pressure [88]. No exceptions are known in continuous space when the interaction potential is of Lennard-Jones type. However, *supersolid* ground states, simultaneously displaying both types of order [40], have been predicted for a class of Bose systems with pair wise interparticle potentials featuring a soft and flat repulsive core at short distances. The supersolid phase arises through the formation at high density of a cluster crystal (CC) with more than one particle per unit cell. At sufficiently low temperature, particle tunneling across adjacent clusters establishes superfluid phase coherence throughout the whole system [103–105].

Cluster crystals have been extensively investigated in the context of classical soft-core systems [41]. It has been conjectured [106] that a necessary condition for the presence of a CC phase in a soft-core system is that the Fourier transform of the potential go negative in a wave-vector range close to $k \sim 1/d$, with d the range of the soft core. Computer simulations of a classical two-dimensional (2D) system of particles interacting through a Gaussian-Core potential whose Fourier transform is positive-definite, has yielded no evidence of a CC at low temperature [39], thus supporting the hypothesis of Ref. [106]. The classical ground state is a crystal at all densities; at low temperature, equilibrium low- and high-density fluid phases exist on both sides of the crystal, with hexatic phases, characterized by the absence of positional order but by a nonvanishing orientational order parameter, separating the crystal from the fluid.

An interesting theoretical question is to what a degree quantum-mechanical effects alter the classical phase diagram. Mean field theoretical treatments based on the Gross-Pitaevskii [107, 108] equation suggest that a negative Fourier component in the pair potential is a necessary condition for a roton instability toward crystallization [109–112]. On the other hand, such an approach essentially describes a supersolid as a superfluid with a density modulation, and is therefore applicable to crystals with a very large number of particles per unit cell. If the number

of particles per unit cell is only a few, it is known that Bose statistics can considerably extend the domain of existence of the CC in soft-core systems with respect to what one would observe classically [113]. Thus, it is conceivable that a CC phase (turning superfluid at low temperature) could be stabilized by quantum-mechanical exchanges in a system of Gaussian-Core bosons. Also, the investigation of a quantum-mechanical version of the Gaussian-Core model can offer insight into the role of those quantum fluctuations in the context of soft matter systems[1].

Our study shows that, as expected, quantum effects strengthen the fluid phase, which extends all the way to temperature $T = 0$ in a wide region of the quantum phase diagram. No cluster crystal and no supersolid phase is found. Indeed, superfluid and (insulating) crystal are the only two phases observed. The resulting quantum phase diagram is qualitatively identical with that of 2D Yukawa bosons [114, 115], suggesting that it may generically describe all Bose systems featuring the same type of repulsive interaction at short distances, i.e., one that is strong enough to prevent the formation of clusters of particles but not enough to stabilize the crystalline phase at high density.

The remainder of this chapter is organized as follows: Sec. 8.1 summarizes two main effects of 2D melting, the Mermin-Wagner theorem and the Berezinsky-Kosterlitz-Thouless transition. In Sec. 8.2, we describe the model of our system of interest and provide details of the calculation, while the ground-state phase-diagram is presented in Sec. 8.3. Last, Sec. 8.4 discusses the unconventional properties of the reentrant superfluid phase.

8.1. Classical two-dimensional phase transitions

The present section gives a short overview of the peculiar properties of two-dimensional phase transitions in classical systems.

The Mermin-Wagner theorem Many effects of statistical mechanics can be studied by analyzing prototypical models that share certain properties such as symmetry or dimension, i.e., models that belong to the same universality class [116]. Therefore, investigating basic models such as the Ising or Heisenberg model of ferromagnetism yields results that go far beyond the actual model. While the Ising model has a phase transition between an unordered high-temperature phase and a magnetized low-temperature phase in two dimensions, the Heisenberg model does not order in this case [116].

In 1966, Mermin and Wagner gave a strict proof why the Heisenberg model (and a large class of generalizations) cannot show spontaneous symmetry-breaking in one- and two-dimensional systems [117] which became known as Mermin-Wagner theorem or Mermin–Wagner–Hohenberg theorem. More concretely, they showed that the order parameter (which is a quantity that has a nonzero average in the ordered phase and is zero otherwise) of the theory is zero at finite temperature if the interactions are sufficiently short-ranged. Their proof uses the continuous $SU(2)$ spin rotation symmetry of the problem which explains why the Ising model (which has a discrete symmetry) does exhibit a ferromagnetic phase with finite magnetization. Note that the theorem does not exclude ordering at zero temperature – indeed, the Heisenberg model is obviously ordered at this temperature in two dimensions. A very similar argument was used in an independent study by Hohenberg that ruled out long-range superfluidity in one and two dimensions [118]. Later, the theorem was generalized to quantum field theory by Coleman [119].

The Berezinsky-Kosterlitz-Thouless transition Although the Mermin-Wagner theorem disallows spontaneous symmetry-breaking for continuous symmetries in one and two dimensions, it

[1] Note that the Gaussian-core potential is used, for example, to model colloids in a solvent. See, for instance, Ref. [41].

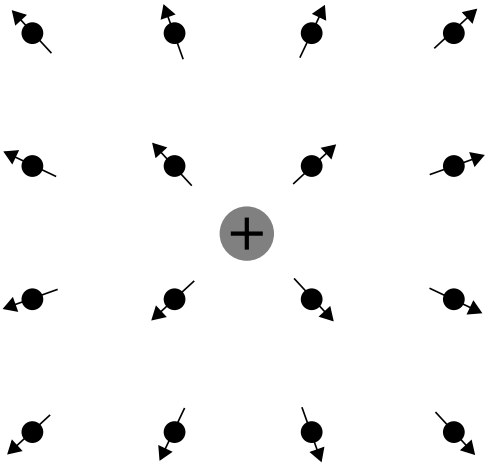

Figure 8.1.: Illustration of a (positive) vortex in the 2D XY-model.

does not imply that phase transitions are impossible in these dimensionalities. In the following, we will give a short summary of the Berezinsky-Kosterlitz-Thouless transition (BKT transition) which will be relevant for the transition of the Gaussian-core system from a low-temperature superfluid phase to a high-temperature normal phase. In 2016, Kosterlitz and Thouless were awarded the Nobel Prize for this work[2].

Since the superfluid-to-normal transition is in the same universality class as the XY-model [116, 120], it is possible to restrict the discussion to the latter model which is defined by the Hamiltonian

$$H = -J \sum_{<ij>} \boldsymbol{S}_i \cdot \boldsymbol{S}_j = -J \sum_{<ij>} \cos(\theta_i - \theta_j). \tag{8.2}$$

Here, $\sum_{<ij>}$ is the sum over all neighboring sites of a 2D square lattice, J is the spin stiffness and $\boldsymbol{S} = (\cos\theta,\ \sin\theta)$ is a spin vector with two components where θ is the angle with the x-axis. At low temperature, the harmonic approximation can be used to evaluate the correlation function as [120]

$$\langle \boldsymbol{S}(\boldsymbol{r}_i) \cdot \boldsymbol{S}(\boldsymbol{r}_j) \rangle \sim |\boldsymbol{r}_i - \boldsymbol{r}_j|^{-\nu} \tag{8.3}$$

for a critical exponent $\nu = k_B T / 2\pi J$, where T is the temperature of the system and k_B is Boltzmann's constant. This means that correlations decay algebraically which ensures that the Mermin-Wagner theorem is not violated. However, as an unordered state is expected to have exponentially decaying correlation functions, a first indication is given that the XY-model in two dimensions has unconventional properties. In the following, algebraically decaying correlations will be called quasi-long-range order. The BKT transition can be seen as a transition between a phase with quasi-long-range order and a disordered phase [121, 122] at a critical temperature T_{KT} with $k_B T_{\mathrm{KT}} = J\pi/2$ [120]. This implies that the correlation function decays as $|\boldsymbol{r}_i - \boldsymbol{r}_j|^{-1/4}$ at the critical temperature. Likewise, for $T < T_{\mathrm{KT}}$, the exponent ν has to be smaller than $1/4$. These results are valid for any model that is in the same universality class as the XY-model.

Intuitively, the BKT transition can be understood by considering vortex configurations (see Fig. 8.1); following an arbitrary path on the lattice and monitoring the change $\Delta\theta$ of the spin configuration angles θ on this path, a vortex can be characterized by yielding $\Delta\theta = \pm n 2\pi \neq 0$ for integer n. At low temperature, it can be shown [120] that only vortex-antivortex pairs yield energetically relevant configurations since the energy cost of a single vortex is unfavorable. Above T_{KT}, the pairs begin to separate into single vortices and yield exponentially decaying correlations.

For superfluid systems, the transition temperature can be estimated by solving the equation

[2] See http://www.nobelprize.org/nobel_prizes/physics/laureates/2016.

[120]

$$\rho_s(T_{\mathrm{KT}}) = \frac{k_B T_{\mathrm{KT}} 2m^2}{\pi\hbar^2}, \tag{8.4}$$

where ρ_s is the superfluid density and $\hbar$ is Planck's constant. Note that Prestipino et al. reference the Kosterlitz-Thouless-Halperin-Nelson-Young (KTHNY) scenario of melting which consists of a two-step procedure of phase transitions from a solid to a hexatic phase and from a hexatic to a liquid phase [39]. Both of these phase transition are possibly of the BKT type.

8.2. Model and Methodology

Model We consider a system of N spin-zero bosons of mass m, enclosed in a simulation box with periodic boundary conditions in both directions. The aspect ratio of the box is designed to fit a triangular solid. Particles interact via the pair potential described by Eq. (8.1). The many-body Hamiltonian of this systems reads

$$\hat{H} = \sum_{i=1}^{N} \frac{\hat{p}_i^2}{2m} + \sum_{i<j} \epsilon \exp\left[-\frac{|\hat{\boldsymbol{x}}_i - \hat{\boldsymbol{x}}_j|^2}{2\sigma^2}\right] \tag{8.5}$$

where $\hat{\boldsymbol{x}}_i$ is the position operator acting on the ith boson. Defining $\Lambda \equiv 1/(m\epsilon\sigma^2)$, the reduced Hamiltonian $\hat{H}' = \hat{H}/\epsilon$ can be written as

$$\hat{H}' = \frac{\Lambda}{2} \sum_{i=1}^{N} \hat{p}_i'^2 + \sum_{i<j} \exp\left[-\frac{1}{2}\left|\hat{\boldsymbol{x}}_i' - \hat{\boldsymbol{x}}_j'\right|^2\right] \tag{8.6}$$

with $\hat{\boldsymbol{p}}' = \hat{\boldsymbol{p}}\sigma$ and $\hat{\boldsymbol{x}}' = \hat{\boldsymbol{x}}/\sigma$ – all lengths are expressed in units of σ, whereas ϵ sets the energy and temperature scale (Boltzmann's constant k_B is set to 1). Besides Λ, the only other parameter of the system at temperature $T = 0$ is the density ρ, or, equivalently, the (dimensionless) mean interparticle distance $r_s = 1/\sqrt{\rho\sigma^2}$.

Method We obtained the thermodynamic phase diagram by means of PIMC simulations based on the Worm Algorithm (see Chapter 7). Technical aspects of the calculations are standard. We carried out simulations of systems comprising up to 1024 particles, using both the quartic action as well as the primitive approximation (the smoothness of the potential allows to obtain accurate results with this form in similar CPU time). We identify the different thermodynamic phases (superfluid and crystalline) through the computation of the superfluid density, the one-body density matrix, as well as the pair-correlation function. As we aim at obtaining the ground-state ($T = 0$) phase diagram, we performed calculations at temperatures sufficiently low so as not to see any changes in the values of cogent physical quantities (e.g., the energy) within the statistical uncertainties of the calculations; typically, this means $T \lesssim T^\star \equiv \Lambda/r_s^2$.

8.3. Phase Diagram

Our findings are summarized in Fig. 8.2, showing the ground-state phase diagram of the system, as described by the Hamiltonian (Eq. (8.6)), in the (r_s–Λ) plane. All of the results presented here are extrapolated to the $\tau \to 0$ limit. We identify the following phases:

1. A superfluid phase at all densities for $\Lambda \gtrsim 0.03$, and in the low- and high-density limit for lower values of Λ, where the physics of the system is dominated by quantum delocalization and Bose statistics. All of our numerical data at finite temperature show consistency

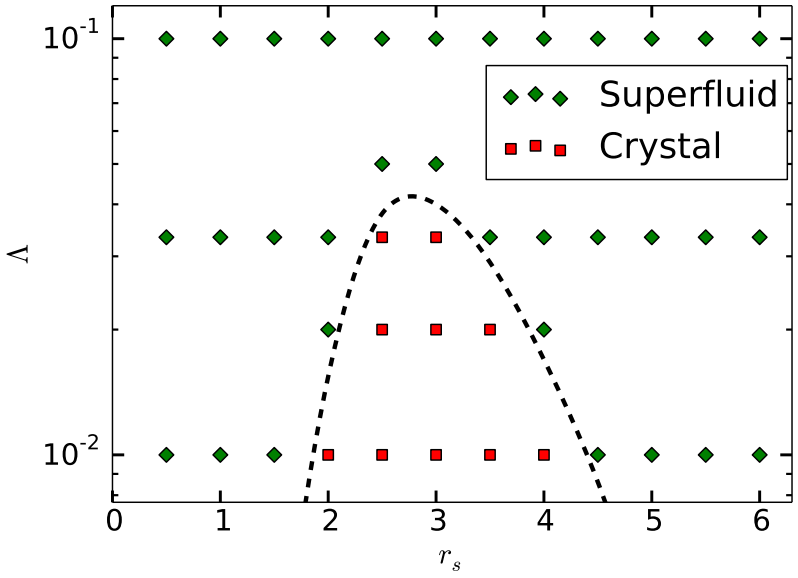

Figure 8.2.: Ground-state phase diagram of a Bose system with Gaussian-Core interaction for different values of the parameter Λ (see text) and mean interparticle spacing r_s. For low values of Λ a crystal phase becomes increasingly stable. At low densities a superfluid phase is seen, while a reentrant superfluid phase is found for high densities. Numerical data are represented by symbols. The dashed line is a guide for the eye.

with the BKT scenario of the superfluid transition in 2D, i.e., the transition between a quasi-long-range superfluid and a normal phase at finite temperature occurs through the standard unbinding of vortex–anti-vortex pairs with charge 1. However, the microscopic properties of the reentrant superfluid phase are unconventional (see below).

2. A crystalline (triangular) phase becomes stable for $\Lambda \lesssim 0.03$, centered around $r_s = 3$. It extends its domain of existence as $\Lambda \to 0$, as the potential energy plays an increasingly important role.

We found no evidence of other phases, such as supersolid phases.

On general grounds we expect a superfluid phase at $T = 0$ in the low density limit by analogy to superfluid helium: In the dilute limit, the potential energy is much smaller than the energy of zero point fluctuations, i.e., the quantum pressure prevents crystallization. That a superfluid phase might also occur at high densities is different from helium. In the present case the soft core of the potential is unable to prevent the overlap of particles at high enough density, leading to a reentrant superfluid, just as in the phase diagram of 2D Yukawa bosons [114, 115].

Insight into the structure of the various phases is offered by the pair-correlation function $g(r)$, shown in Fig. 8.3 for the crystal and both conventional and reentrant superfluids. For $r_s \geq 3$ (i.e., in the crystalline and low-density superfluid phases), the physics effectively mimics that of a hard-core system, characterized by a vanishing $g(r)$ at short distances and resulting in conventionally looking pair-correlation functions, as is shown in Fig. 8.3 for $r_s = 3$. The peak structure in $g(r)$ is washed out as the system is compressed and r_s is reduced below 3, at which point $g(r)$ suddenly acquires a finite value at the origin, as the finite potential energy cost no longer prevents particles from overlapping. Further compression of the system into the reentrant superfluid phase has the effect of raising the value of $g(0)$, as the system approaches the behavior of a free Bose gas. Note that the first peak of $g(r)$ in the conventional superfluid phase is more pronounced than the corresponding peak of the reentrant superfluid; this is a consequence of the effective hard-core interaction between the particles. As a finite-temperature method is employed,

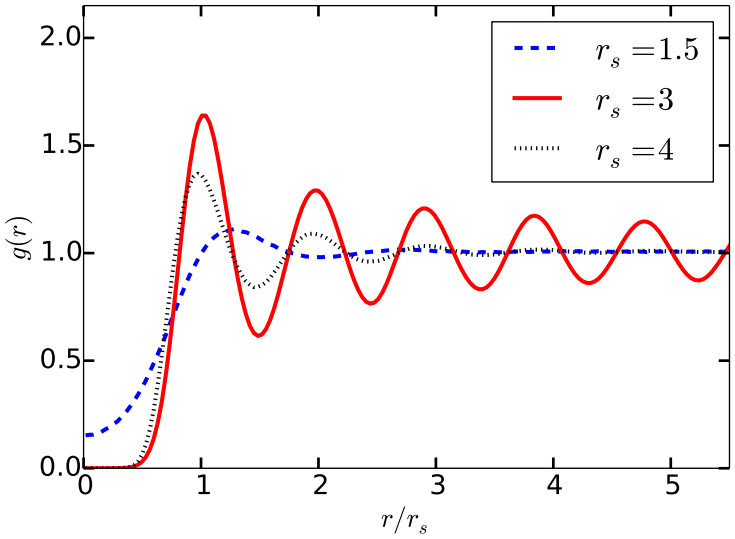

Figure 8.3.: Ground-state pair-correlation functions for different values of r_s at $\Lambda = 1/30$. Error bars are too small to be seen on the scale of the figure. While the pair-correlation functions for $r_s = 4$ and $r_s = 3$ (corresponding to the superfluid and crystal phases) show hard-core separation of particles, the reentrant superfluid phase ($r_s = 1.5$) acquires a finite value at the origin. In this phase, only very weak peaks are left, rendering $g(r)$ essentially flat for $r \gtrsim 2$.

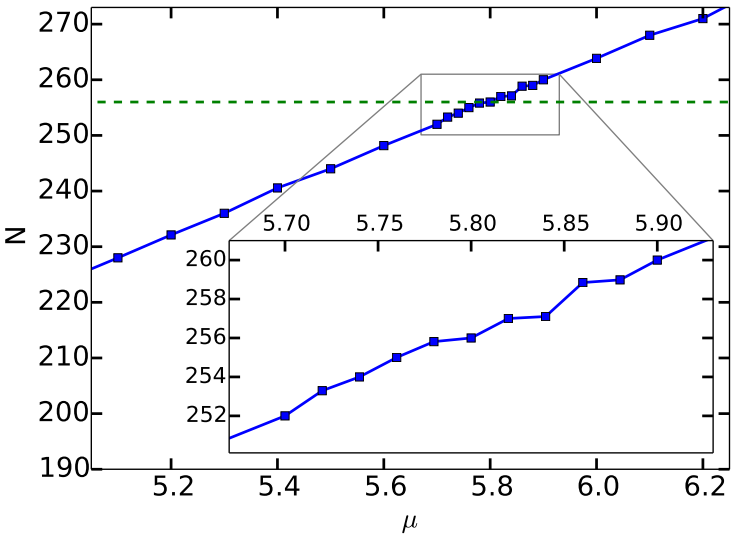

Figure 8.4.: Particle number as a function of grand-canonical chemical potential μ for $r_s = 1$, $T = 0.001$ and $\Lambda = 1/1000$. The initial configuration is always a solid configuration at $N = 256$ in a commensurate box. As the grand-canonical simulation allows the particle number to fluctuate, noninteger values of N are possible. However, for the point of $\mu = 5.8$ (corresponding to $N = 256$), no particle number changes are observed; this happens for several values of μ. The horizontal line corresponds to 256 particles. Error bars are not visible on this scale. In the inset, a zoom on the data shows regions of nearly constant particle number.

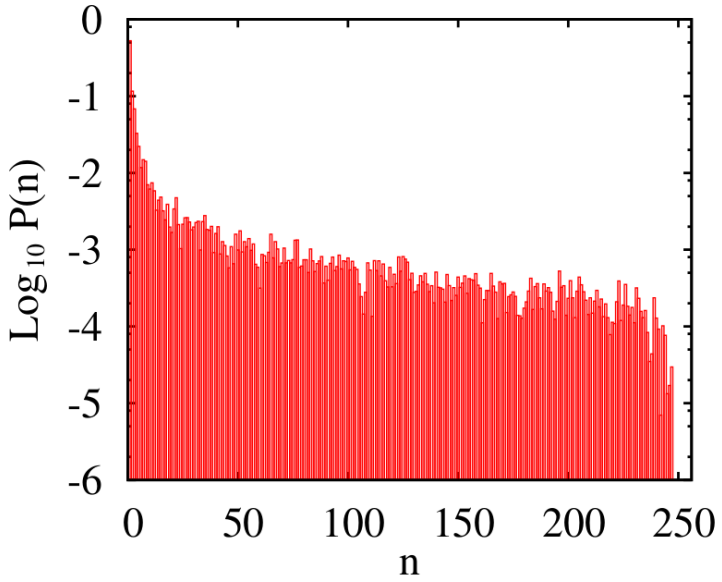

Figure 8.5.: For $r_s = 1$, $\Lambda = 0.001$, $T = 1/6400$ and 256 particles, the probability $P(n)$ of bosonic exchanges involving n particle worldlines is shown.

the magnitude of the peaks of $g(r)$ decreases even in the solid phase. This is expected, as thermal fluctuations do not allow true crystalline order in two dimensions. The important observation is that the distance between neighboring peaks is constant over a large range of r.

8.4. Reentrant superfluid phase in the limit of weak quantum fluctuations

Next, we investigate the point $r_s = 1$, $\Lambda = 0.001$ and $T = 0.001$, which corresponds to high density and weak quantum fluctuations. Fig. 8.4 shows the total number of particles for different grand-canonical simulations in an initially solid configuration of $N = 256$ particles for several values of the chemical potential μ. While the curve suggests a linear relationship between chemical potential and particle number (implying a constant nonzero compressibility), tiny deviations of much lower compressibility can be seen. These may hint at a tendency towards insulating behavior, but this is not the case here; they are a consequence of low temperature and finite system size, similar to the observation of finite charging levels in a quantum dot. It is well known that in dilute superfluids the compressibility at very low temperatures can also be very small on small system sizes and very low temperatures due to the same mechanism. What is surprising here is that this occurs already for temperatures of the order of the BKT temperature. Nevertheless, a gapped solidlike structure can certainly be ruled out in the thermodynamic limit on the basis of the pair-correlation function. In addition, the corresponding Green's function at zero momentum, $G(\tau, p = 0)$, goes up with increasing system size for $|\tau| \gg 0$, i.e., adding particles to the simulation becomes easier. This is one of the manifestations that this parameter regime is very difficult to simulate.

In particular, the superfluid density has anomalously large autocorrelation times, which are unusual for the worm algorithm. Interestingly, bosonic particle exchanges do not suffer from the same decorrelation problem. Fig. 8.5 shows a typical distribution of particle permutations where exchanges up to the total number of particles are reached. The distribution can already be reliably measured in early stages of the simulation without observing any superfluid response.

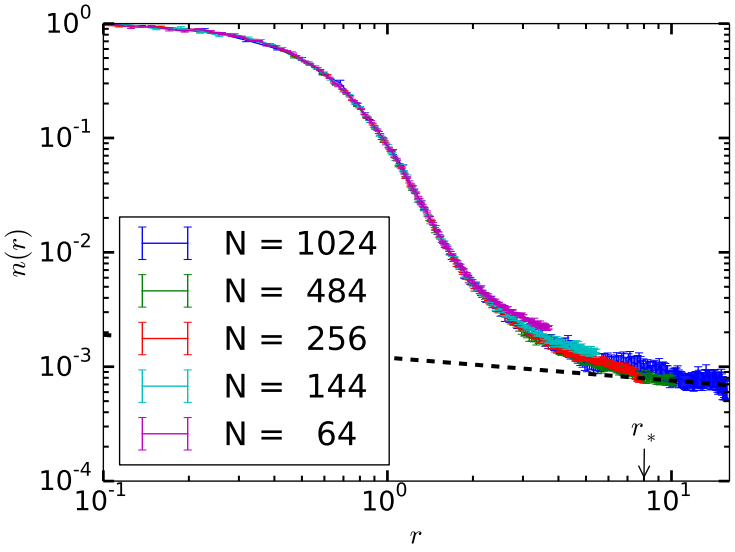

Figure 8.6.: The equal-time one-body density matrix at $r_s = 1$ for $\Lambda = 0.002$, $T = 0.002$ and different system sizes. After a rapid initial decay, a nonintegrable power-law decay is seen for big enough system sizes, rendering the phase a superfluid. The dashed line illustrates the linear regime which holds for all $r > r_*$ (see text).

This disagrees with the perception that macroscopic exchanges directly trigger superfluidity (which holds for dilute systems). The superfluidity of the phase is never in doubt though, as can be seen from the the one-body density matrix $n(r)$, shown for a similar point ($\Lambda = 0.002$) in Fig. 8.6. It experiences a weak power-law decay (setting in at a distance r_*) after a fast initial drop with a power less than 1/4, demonstrating the existence of off-diagonal long-range order in the system. Although the asymptotic behavior of the curve is consistent with conventional superfluids, the low value of $n(r_*)$ at which this power law sets in is unusual. Comparing this curve with measurements for higher Λ, it follows that we can tune $n(r_*)$ with Λ. For increasing Λ, the winding estimator yields the correct superfluid response more and more reliably (cf. Fig. 8.2).

On the basis of all these observations, we can state that the system is ultimately a superfluid based on its properties for big enough system sizes. The unusual microscopics are due to the denseness witnessed in this parameter regime. Finally, we note that the behavior of $n(r)$ and $g(r)$ for sufficiently large values of r, as well as of the superfluid density, is remarkably similar to the observations of the superglass in Ref. [123]. However, as we are looking for the thermodynamic ground state of the system, such a metastable state can be excluded. Hence, the claim for a superglass, as in Ref. [123], should only be made on the basis of additional real-time considerations. We leave for future work the static response of this phase, i.e., how it responds to pinning or disorder.

9 Conclusion and outlook

In this thesis, we used two of the most recent techniques for interacting many-particle problems, diagrammatic Monte Carlo for fermionic systems and Path integral Monte Carlo for bosons. In both cases, the ground state properties of the respective systems were examined by a careful analysis of Monte Carlo observables. While the main challenges of diagrammatic Monte Carlo were series convergence and extrapolation, i.e., generic issues that affect the method as a whole, the situation was more specific in the case of Path integral Monte Carlo, meaning that the unconventional findings originated from the concrete potential.

More precisely, the first part of the thesis applied diagrammatic Monte Carlo to the Fermi polaron problem. This is an important limiting case of population imbalanced Fermi gases and allows to estimate key properties of its phase diagram. We elaborated on the convergence of the diagrammatic series in a number of ways. First, an additional regrouping technique was presented which speeds up extrapolation to infinite diagram order for absolutely convergent series. Secondly, we illustrated a critical analysis and alternative check of diagrammatic Monte Carlo as well as a partially bold approach, thus broadening the toolbox of the method.

For the quasi-two-dimensional Fermi-polaron problem, we emulated realistic cold-gas experiments by adding a laser with a strong trapping frequency in the z direction to our system. The validity of this approach was checked by comparing results for different trapping frequencies and the pure 2D limit, showing good agreement for the confinement we used. The resulting transition point between the polaron and molecular ground states is shifted with respect to the variational first-order calculations but is in very good agreement with variational results in the two-particle-hole (2-ph) subspace. Our Monte Carlo results have shown that the difference between 2-ph and 3-ph contributions is vanishing within the error bars, and this holds order per order in the Feynman expansion using the T matrix as the expansion parameter. We therefore suggest computing the 2-ph contributions by using the wave-function approach and switching to diagMC for the computation of corrections to the 2-ph contributions. The number of hole lines can still be used as the expansion parameter for polaron problems at finite momentum, where the wave-function approach is no longer variational. It is the restricted phase space for hole excitations [20] that enables this.

In the case of a three-dimensional Fermi polaron, our work extends the diagrammatic Monte Carlo polaron routines to the more general case of a mass-imbalanced polaron. While the first-order variational ansatz could give qualitative and quantitative good results for the polaron energy at different polaron masses, discrepancies are more pronounced for the polaron residue. For this quantity, higher orders have to be included in order to capture the whole physics. Concerning Tan's contact coefficient, an excellent agreement was found with the Chevy variational wave function. The polaronic spectral function was extracted from imaginary time representation of diagrammatic Monte Carlo data by means of analytic continuation. It demonstrates a clean parabolic dispersion as well as the existence of the repulsive polaron. The 2-ph wave-function ansatz provides an equally good description of quasi-particle energies in three dimensions. Therefore, using 1-ph trial functions will lead to a phase diagram which overestimates molecular

contributions and might lead to a weakening of the FFLO state found in Ref. [17].

The second part of the thesis switched to bosonic particle statistics, namely to a system of two-dimensional Gaussian-core bosons. A first-principles numerical investigation of the phase diagram by Path integral Monte Carlo yielded two different phases: A crystal and a superfluid, which also showed reentrant behavior at high densities. No supersolid or cluster crystal phases were found. This was anticipated by the positiveness of the interaction potential in Fourier space and affirms the cluster crystal conjecture of Ref. [106]. The reentrant superfluid phase demonstrates unexpected behavior for high particle mass. The power-law decay of the one-body density matrix sets in at large distances, where its value is already quite low. This requires big system sizes to capture the relevant length scales. Likewise, grand-canonical simulations experience deviations from nonzero compressibility for finite systems. This is complemented by the occurrence of large cycles of particle worldline permutations, independent of system size.

Whether such a system may lend itself to experimental realization is difficult to assess. Recent progress in cold-atom manipulation allows one to tailor, to some degree, the interaction among atoms [48]. The other aspects of the system, including its detection, are already well within current technology [48]. Crucially, the Gaussian potential has no preferred length scale, unlike the softened dipolar [124] or Rydberg potentials, whereas a system of Yukawa bosons [114, 115] shows a qualitatively similarly looking phase diagram.

There are several open questions that could be addressed in subsequent projects. Regarding the Fermi polaron problem, the quasi-2D limit could be accessed by incorporating the full harmonic occupancy, enabling the use of arbitrary ω_z. As the different oscillator levels are usually introduced by summation, a simple broadening of diagrammatic space is sufficient to solve this problem. Also, the case of different masses of impurity and bath atoms has not been evaluated by diagrammatic Monte Carlo in these reduced dimensionalities so far. Lastly, an extension of the Fermi polaron problem to finite temperature or non-equilibrium could be promising.

A follow-up project for the system of Gaussian-core bosons could consist of a thorough analysis of a possible hexatic phase between the superfluid and crystal phases. As orientational order was only seen in a very small subspace of parameter space for classical Gaussian-core bosons [39], a very good resolution seems necessary for this investigation.

Another idea that comes to mind is the application of Path integral Monte Carlo to the case of a Bose polaron. In contrast to the Fermi polaron, this system is composed by the impurity and a weakly interacting *bosonic* bath. The system could be designed by using Gaussian-core potentials for the boson-boson and boson-impurity interactions with different ϵ and σ so that the desired ratio of scattering lengths is generated. If one worldline is excluded from exchanges, PIMC can model this system by extrapolating to the thermodynamic limit. Establishing theoretical control of the Bose polaron is a challenging question, as the limit of intermediate coupling is still under debate [125].

A Scattering Theory

This appendix gives a full treatment of the derivations omitted in Chapter 2.

A.1. Scattering in three dimensions

Partial waves As we assume that V is a central potential, a standard separation ansatz [126]

$$\psi_{\boldsymbol{k}}(\boldsymbol{r}) = \sum_{l=0}^{\infty} \sum_{m=-l}^{l} i^l \sqrt{4\pi(2l+1)} R_{lm}(r) Y_{lm}(\theta, \phi). \tag{A.1}$$

in terms of spherical harmonics Y_{lm} can be used in Eq. (2.7). Here, l and m label individual solutions $R_{lm}(r)Y_{lm}(\theta,\phi)$ of Eq. (2.7). The constant factor $i^l\sqrt{4\pi(2l+1)}$ was appended for convenience. As $\psi_{\boldsymbol{k}}$ does not depend on ϕ, it follows that all terms with $m \neq 0$ do not contribute to the ansatz. This reduces Eq. (A.1) to

$$\begin{aligned}
\psi_{\boldsymbol{k}}(\boldsymbol{r}) &= \sum_{l} i^l \sqrt{4\pi(2l+1)} R_{l0}(r) Y_{l0}(\theta, \phi) \\
&= \sum_{l} i^l \sqrt{4\pi(2l+1)} R_l(r) \sqrt{\frac{2l+1}{4\pi}} P_l(\cos\theta) \\
&= \sum_{l} i^l (2l+1) R_l(r) P_l(\cos\theta)
\end{aligned} \tag{A.2}$$

with the Legendre polynomial P_l [126]. As

$$\left(-\frac{1}{r^2 \sin\theta} \frac{\partial}{\partial\theta} \left(\sin\theta \frac{\partial}{\partial\theta} \right) - \frac{1}{r^2 \sin^2\theta} \frac{\partial^2}{\partial\phi^2} \right) Y_{l0} = \frac{l(l+1)}{r^2} Y_{l0}, \tag{A.3}$$

the equation for the radial part R is

$$\left[-\frac{1}{r^2} \frac{\mathrm{d}}{\mathrm{d}r} \left(r^2 \frac{\mathrm{d}}{\mathrm{d}r} \right) + \frac{l(l+1)}{r^2} - k^2 + 2m_r V(r) \right] R_l(r) = 0. \tag{A.4}$$

The strategy of the partial wave expansion is the following: The scattering process is fully characterized by the behavior of the scattered wave far from the scattering center. In this regime, the potential may be neglected and the equation

$$\left[-\frac{1}{r^2} \frac{\mathrm{d}}{\mathrm{d}r} \left(r^2 \frac{\mathrm{d}}{\mathrm{d}r} \right) + \frac{l(l+1)}{r^2} - k^2 \right] R_l(r) = 0 \tag{A.5}$$

can be identified as the spherical Bessel differential equation. It is solved by a linear combination

of spherical Bessel functions, or, alternatively, by spherical Hankel functions [126] of first and second kind,

$$R_l(r) = A_l \left(h_l^{(2)}(kr) + e^{2i\delta_l} h_l^{(1)}(kr) \right). \tag{A.6}$$

A_l and $e^{2i\delta_l}$ denote the linear coefficients. The scattering phase shift δ_l has to be real because of flux conservation [47, 126]. Using the asymptotic form of the spherical Hankel functions yields [47]

$$R_l(r) \sim A_l \left(\frac{i^{l+1} e^{-ikr}}{kr} + e^{2i\delta_l} \frac{(-i)^{l+1} e^{ikr}}{kr} \right) \tag{A.7}$$

for $kr \gg 1$. Thus, the wave function is given by

$$\psi_{\boldsymbol{k}}(\boldsymbol{r}) \sim \sum_{l=0}^{\infty} i^l \frac{(2l+1)}{kr} A_l \left(i^{l+1} e^{-ikr} + e^{2i\delta_l} (-i)^{l+1} e^{ikr} \right) P_l(\cos\theta), \tag{A.8}$$

or, equivalently,

$$\psi_{\boldsymbol{k}}(\boldsymbol{r}) \sim \sum_{l=0}^{\infty} \frac{(2l+1)}{ikr} P_l(\cos\theta) \left(e^{2i\delta_l} e^{ikr} - (-1)^l e^{-ikr} \right) A_l. \tag{A.9}$$

Since we want to match this result with the expected asymptotic form of Eq. (2.8), the incoming plane wave has to be written in terms of partial waves [126]

$$e^{ikz} = \sum_{l=0}^{\infty} i^l (2l+1) j_l(kr) P_l(\cos\theta), \tag{A.10}$$

where $j_l(kr)$ denotes the spherical Bessel function of the first kind [70]. Furthermore, the scattering amplitude can be expanded in a Fourier-Legendre series as

$$f_k(\theta) = \sum_{l=0}^{\infty} (2l+1) f_l P_l(\cos\theta) \tag{A.11}$$

for some coefficients f_l. Plugging the expressions for e^{ikz} and $f_k(\theta)$ into Eq. (2.8) and using the asymptotic form of $j_l(kr)$ leaves

$$\psi_{\boldsymbol{k}}(\boldsymbol{r}) \sim \sum_{l=0}^{\infty} \frac{2l+1}{kr} P_l(\cos\theta) \left(\frac{i^l}{2i} \left(e^{i(kr - \frac{l\pi}{2})} - e^{-i(kr - \frac{l\pi}{2})} \right) + k f_l e^{ikr} \right). \tag{A.12}$$

This can be reorganized as

$$\begin{aligned} \psi_{\boldsymbol{k}}(\boldsymbol{r}) &\sim \sum_{l=0}^{\infty} \frac{2l+1}{2ikr} P_l(\cos\theta) \left(e^{ikr} - (-1)^l e^{-ikr} + 2ik f_l e^{ikr} \right) = \\ &= \sum_{l=0}^{\infty} \frac{2l+1}{2ikr} P_l(\cos\theta) \left(e^{ikr}(1 + 2ik f_l) - (-1)^l e^{-ikr} \right). \end{aligned} \tag{A.13}$$

Low-energy scattering The rest of this section presents an alternative way of introducing the scattering length. For $l = 0$ Eq. (A.6) leads to

$$R_0(r) \propto h_0^{(2)}(kr) + e^{2i\delta_0} h_0^{(1)}(kr) \propto e^{-ikr} - e^{2i\delta_0} e^{ikr} \tag{A.14}$$

$$\propto e^{-ikr-i\delta_0} - e^{ikr+i\delta_0} \propto \sin(kr+\delta_0) = \sin(k(r+\delta_0/k)),$$

where the explicit form of $h_0^{(1)}$ and $h_0^{(2)}$ was used [47]. Remembering $a_{3D} = -\lim_{k\to 0^+} \frac{\delta_0}{k}$, it follows that the radial wave-function is zero for $r = a_{3D}$ in the limit of small k. This view gives a very intuitive picture of δ_0 as the relative phase shift of a scattered wave with respect to free propagation. It is important to emphasize that R_0 of Eq. (A.14) is only correct in the limit of large r, where the potential goes to zero. Nevertheless, once R_0 is determined from the large r behavior of the system, there is no problem to fit it by $\sin(k(r+\delta_0/k))$ and continue it to low r in order to read off the scattering length, although it is not the correct solution of the radial equation in that limit.

A.2. Scattering in two dimensions

Partial waves For a central potential $V(r,\phi) = V(r)$, Eq. (2.20) allows a solution of the form $\psi_{\boldsymbol{k}}(r,\phi) = \sum_m R_m(r)T_m(\phi)$, where each $R_m(r)T_m(\phi)$ is a separate solution. The angular part,

$$\frac{\mathrm{d}^2 T_m(\phi)}{\mathrm{d}\phi^2} = -m^2 T_m(\phi), \tag{A.15}$$

admits solutions of the form $T_m(\phi) = c_m\cos(m\phi) + d_m\sin(m\phi)$ for some coefficients c_m and d_m. m has to be a real integer because of the requirement $T(\phi+2\pi) = T(\phi)$. Since

- $T(0)$ might be nonzero and
- $T(\phi) = \pm T(-\phi)$ because of the cyclindrical symmetry of the problem,

the sine part of the solution is suppressed. This leaves $T_m(\phi) = \frac{1}{\sqrt{\pi}}\cos(m\phi)$, where we have chosen a convenient normalization.

After solving the angular subequation, the radial part of Eq. (2.20) in the limit $r\to\infty$,

$$\frac{1}{r}\frac{\mathrm{d}}{\mathrm{d}r}\left(r\frac{\mathrm{d}R_m(r)}{\mathrm{d}r}\right) - \frac{m^2}{r^2}R_m(r) + k^2 R_m(r) = 0, \tag{A.16}$$

is solved by Bessel functions of the first and second kind[1]:

$$\begin{aligned}
R'_m(kr) &= A'_m J_m(kr) + B'_m Y_m(kr) = A'_m\left(J_m(kr) + \frac{B'_m}{A'_m}Y_m(kr)\right)\\
&= A'_m\left(J_m(kr) + \tan(-\delta_m)Y_m(kr)\right)\\
&= \frac{A'_m}{\cos(\delta_m)}\left(\cos(\delta_m)J_m(kr) - \sin(\delta_m)Y_m(kr)\right)\\
&\xrightarrow[kr\to\infty]{} A_m\sqrt{\frac{2}{\pi kr}}\left(\cos(\delta_m)\cos\left(kr - \frac{m\pi}{2} - \frac{\pi}{4}\right) - \sin(\delta_m)\sin\left(kr - \frac{m\pi}{2} - \frac{\pi}{4}\right)\right)\\
&= A_m\sqrt{\frac{2}{\pi kr}}\cos\left(kr - \frac{m\pi}{2} - \frac{\pi}{4} + \delta_m\right).
\end{aligned} \tag{A.17}$$

The transformation in the third step can be seen as the definition of the scattering phase shift $\delta_m \in]-\pi,\pi]$, while the asymptotic analytic forms of the Bessel functions were used for the large

[1] This expression is the Bessel differential equation for $R'_m(kr)$ if the relation $\partial/\partial r = k\,\partial/\partial(kr)$ is used. It is important to note that $R_m(r) = R'_m(kr)$.

kr limit. Summing up, the scattering wave function takes the following shape:

$$\psi_{\boldsymbol{k}}(\boldsymbol{r}) = \sum_{m=0}^{\infty} A_m \frac{\sqrt{2}}{\pi\sqrt{kr}} \cos(m\phi) \cos\left(kr - \frac{m\pi}{2} - \frac{\pi}{4} + \delta_m\right) =$$
$$= \sum_{m=0}^{\infty} A_m \frac{\sqrt{2}}{\pi\sqrt{kr}} \cos(m\phi) \frac{1}{2} \left(e^{i(kr - \frac{m\pi}{2} - \frac{\pi}{4} + \delta_m)} + e^{-i(kr - \frac{m\pi}{2} - \frac{\pi}{4} + \delta_m)}\right). \tag{A.18}$$

In the following, we want to match this expression with the asymptotic form (Eq. (2.21)) so that the scattering amplitude can be identified. Decomposing the plane wave of Eq. (2.21) into polar coordinates yields [52]

$$\psi_{\boldsymbol{k}}(\boldsymbol{r}) = \sum_{m=0}^{\infty} \epsilon_m i^m \cos(m\phi) J_m(kr) - \sqrt{\frac{i}{8\pi}} f_k(\phi) \frac{e^{ikr}}{\sqrt{kr}}. \tag{A.19}$$

ϵ_m is 2 for $m \neq 0$ and 1 for $m = 0$. Plugging in the asymptotics of J_m gives [70]

$$\psi_{\boldsymbol{k}}(\boldsymbol{r}) \underset{kr\to\infty}{\longrightarrow} \sum_{m=0}^{\infty} \epsilon_m i^m \cos(m\phi) \sqrt{\frac{2}{\pi kr}} \cos\left(kr - \frac{m\pi}{2} - \frac{\pi}{4}\right) - \sqrt{\frac{i}{8\pi}} f_k(\phi) \frac{e^{ikr}}{\sqrt{kr}} =$$
$$= \sum_{m=0}^{\infty} \epsilon_m i^m \cos(m\phi) \sqrt{\frac{2}{\pi kr}} \frac{1}{2} \left(e^{i(kr - \frac{m\pi}{2} - \frac{\pi}{4})} + e^{-i(kr - \frac{m\pi}{2} - \frac{\pi}{4})}\right) - \sqrt{\frac{i}{8\pi}} f_k(\phi) \frac{e^{ikr}}{\sqrt{kr}}. \tag{A.20}$$

Finally, a comparison of Eqs. (A.18) and Eq. (A.20) makes it possible to get an expression of the scattering amplitude in terms of the scattering phase shifts. In Eq. (A.20), all terms containing e^{-ikr} are on the left, thus $A_m e^{-i\delta_m} = \epsilon_m i^m \sqrt{\pi}$. This fixes A_m. The remaining equation is

$$\sqrt{\frac{i}{8\pi}} f_k(\phi) \frac{1}{\sqrt{kr}} = \sum_{m=0}^{\infty} \cos(m\phi) \sqrt{\frac{2}{kr}} \frac{1}{2} e^{i(-\frac{m\pi}{2} - \frac{\pi}{4})} \left(-e^{i\delta_m} \frac{A_m}{\pi} + \frac{i^m}{\sqrt{\pi}} \epsilon_m\right) =$$
$$= \sum_{m=0}^{\infty} \cos(m\phi) \sqrt{\frac{2}{kr}} \frac{1}{2} e^{i(-\frac{m\pi}{2} - \frac{\pi}{4})} \left(-e^{2i\delta_m} \epsilon_m i^m \sqrt{\pi} \frac{1}{\pi} + \frac{i^m}{\sqrt{\pi}} \epsilon_m\right) =$$
$$= \sum_{m=0}^{\infty} \cos(m\phi) \sqrt{\frac{2}{\pi kr}} \frac{1}{2} e^{i(-\frac{m\pi}{2} - \frac{\pi}{4})} \epsilon_m i^m \left(-e^{2i\delta_m} + 1\right) \tag{A.21}$$

Further rewriting shows that

$$f_k(\phi) = \sum_{m=0}^{\infty} 2(-i) \cos(m\phi) \epsilon_m (1 - e^{2i\delta_m}) = \sum_{m=0}^{\infty} 2(-i) \cos(m\phi) \epsilon_m e^{i\delta_m} (e^{-i\delta_m} - e^{i\delta_m}) =$$
$$= \sum_{m=0}^{\infty} 2(-i) \cos(m\phi) \epsilon_m e^{i\delta_m} (-2i \sin(\delta_m)) = -4 \sum_{m=0}^{\infty} \cos(m\phi) \epsilon_m e^{i\delta_m} \sin(\delta_m). \tag{A.22}$$

This is the partial wave expansion of the scattering amplitude in two dimensions.

Low energy scattering Finally, the scattering of particles with low energy is investigated. The Schrödinger equation in polar coordinates illustrates that only low m will contribute in this regime. Focusing on $m = 0$, the scattering amplitude takes the form

$$f_k(\phi) = -4e^{i\delta_0} \sin(\delta_0) = -\frac{4 \sin(\delta_0)}{\cos(\delta_0) - i \sin(\delta_0)} = \frac{4}{-\cot(\delta_0) + i}. \tag{A.23}$$

Next, the relation between the scattering length and δ_0 is established. In two dimensions, we define the scattering length by finding the roots of $R_0(r)$. Going back to Eq. (A.17),

$$R_0'(kr) = A_0' \left(J_0(kr) - \tan(\delta_0) Y_0(kr) \right) \stackrel{!}{=} 0, \tag{A.24}$$

the asymptotic expansions of the Bessel functions for small kr can be used:

$$\cot(\delta_0) = \frac{2}{\pi} \left(\ln\left(\frac{k a_{2D}^*}{2} \right) + \gamma \right), \tag{A.25}$$

where γ is the Euler-Mascheroni constant (≈ 0.5772) and the two-dimensional scattering length a_{2D}^* was introduced as root of the radial wave function. The final result for the low energy scattering amplitude is

$$f_k(\phi) = \frac{4\pi}{-2\ln(k a_{2D}) + i\pi}, \tag{A.26}$$

where $a_{2D} = a_{2D}^* e^{\gamma}/2$ was rescaled to make this expression more compact – the scattering length possesses an 'inherent uncertainty' in two dimensions [127] since it is always defined with respect to some finite k (unlike the three-dimensional scattering length which is defined in the $k \to 0$ limit).

Bibliography

[1] P. Kroiss and L. Pollet, Phys. Rev. B **90**, 104510 (2014).

[2] P. Kroiss and L. Pollet, Phys. Rev. B **91**, 144507 (2015).

[3] P. Kroiss, M. Boninsegni, and L. Pollet, Phys. Rev. B **93**, 174520 (2016).

[4] W. Krauth, *Statistical Mechanics: Algorithms and Computations* (Oxford University Press, UK, 2006).

[5] M. Kalos and P. Whitlock, *Monte Carlo Methods* (Wiley, 2008).

[6] N. Metropolis and S. Ulam, J. Amer. Stat. Assoc. **44**, 335 (1949).

[7] M. Troyer and U. Wiese, Phys. Rev. Lett. **94**, 170201 (2005).

[8] W. Zwerger, ed., *The BCS-BEC Crossover and the Unitary Fermi Gas* (Springer, Berlin, Heidelberg, 2012).

[9] N. V. Prokof'ev and B. V. Svistunov, Phys. Rev. B **77**, 125101 (2008).

[10] N. V. Prokof'ev and B. V. Svistunov, Phys. Rev. B **77**, 020408 (2008).

[11] A. Schirotzek, C. H. Wu, A. Sommer, and M. W. Zwierlein, Phys. Rev. Lett. **102**, 230402 (2009).

[12] S. Nascimbène, N. Navon, K. J. Jiang, L. Tarruell, M. Teichmann, J. McKeever, F. Chevy, and C. Salomon, Phys. Rev. Lett. **103**, 170402 (2009).

[13] C. Kohstall, M. Zaccanti, M. Jag, A. Trenkwalder, P. Massignan, G. M. Bruun, F. Schreck, and R. Grimm, Nature (London) **485**, 615 (2012).

[14] M. M. Parish and J. Levinsen, Phys. Rev. A **87**, 033616 (2013).

[15] S. Pilati and S. Giorgini, Phys. Rev. Lett. **100**, 030401 (2008).

[16] G. Bertaina and S. Giorgini, Phys. Rev. Lett. **106**, 110403 (2011).

[17] C. J. M. Mathy, M. M. Parish, and D. A. Huse, Phys. Rev. Lett. **106**, 166404 (2011).

[18] F. Chevy, Phys. Rev. A **74**, 063628 (2006).

[19] R. Combescot, A. Recati, C. Lobo, and F. Chevy, Phys. Rev. Lett. **98**, 180402 (2007).

[20] R. Combescot and S. Giraud, Phys. Rev. Lett. **101**, 050404 (2008).

[21] C. Mora and F. Chevy, Phys. Rev. A **80**, 033607 (2009).

[22] M. Punk, P. T. Dumitrescu, and W. Zwerger, Phys. Rev. A **80**, 053605 (2009).

[23] R. Combescot, S. Giraud, and X. Leyronas, Europhys. Lett. **88**, 60007 (2009).

[24] P. Massignan and G. M. Bruun, Eur. Phys. J. D **65**, 83 (2011).

[25] C. Trefzger and Y. Castin, Europhys. Lett. **101**, 30006 (2013).

[26] J. E. Baarsma, J. Armaitis, R. A. Duine, and H. T. C. Stoof, Phys. Rev. A **85**, 033631 (2012).

[27] R. Schmidt and T. Enss, Phys. Rev. A **83**, 063620 (2011).

[28] C. Lobo, A. Recati, S. Giorgini, and S. Stringari, Phys. Rev. Lett. **97**, 200403 (2006).

[29] P. Massignan, M. Zaccanti, and G. M. Bruun, Rep. Prog. Phys **77**, 034401 (2014).

[30] E. V. H. Doggen and J. J. Kinnunen, Phys. Rev. Lett. **111**, 025302 (2013).

[31] M. Koschorreck, D. Pertot, E. Vogt, B. Fröhlich, M. Feld, and M. Köhl, Nature (London) **485**, 619 (2012).

[32] S. Zöllner, G. M. Bruun, and C. J. Pethick, Phys. Rev. A **83**, 021603 (2011).

[33] M. M. Parish, Phys. Rev. A **83**, 051603 (2011).

[34] O. I. Kartavtsev and A. V. Malykh, J. Phys. B **40**, 1429 (2007).

[35] D. Blume, Phys. Rev. Lett. **109**, 230404 (2012).

[36] J. Levinsen and M. M. Parish, Phys. Rev. Lett. **110**, 055304 (2013).

[37] F. H. Stillinger, J. Chem. Phys. **65**, 3968 (1976).

[38] S. Prestipino, F. Saija, and P. V. Giaquinta, Phys. Rev. E **71**, 050102 (2005).

[39] S. Prestipino, F. Saija, and P. V. Giaquinta, Phys. Rev. Lett. **106**, 235701 (2011).

[40] M. Boninsegni and N. V. Prokof'ev, Rev. Mod. Phys. **84**, 759 (2012).

[41] C. N. Likos, Phys. Rep. **348**, 267 (2001).

[42] N. Metropolis, A. W. Rosenbluth, M. N. Rosenbluth, A. H. Teller, and E. Teller, J. Chem. Phys. **21**, 1087 (1953).

[43] V. Ambegaokar and M. Troyer, Am. J. Phys. **78**, 150 (2010).

[44] B. Bauer et al., J. Stat. Mech., P05001 (2011).

[45] `http://www.pcg-random.org/paper.html` (visited on 12/12/2016).

[46] P. Kroiss, "The Fermi polaron problem for unequal masses", Diploma thesis (Technical University Munich, 2013).

[47] D. Griffiths, *Introduction to quantum mechanics* (Pearson Prentice Hall, 2005).

[48] I. Bloch, J. Dalibard, and W. Zwerger, Rev. Mod. Phys. **80**, 885 (2008).

[49] H. Stoof, K. Gubbels, and D. Dickerscheid, *Ultracold Quantum Fields* (Springer, Berlin, 2009).

[50] H. A. Bethe, Phys. Rev. **76**, 38 (1949).

[51] M. Inguscio, W. Ketterle, and C. Salomon, *Ultra-Cold Fermi Gases: Varenna 20-30 June 2006* (IOS Press, Amsterdam, 2007).

[52] S. K. Adhikari, Am. J. Phys. **54**, 362 (1986).

[53] D. S. Petrov and G. V. Shlyapnikov, Phys. Rev. A **64**, 012706 (2001).

[54] N. N. Khuri, A. Martin, J. M. Richard, and T. T. Wu, J. Math. Phys. **50**, 072105 (2009).

[55] M. W. Zwierlein, C. H. Schunck, A. Schirotzek, and W. Ketterle, Nature (London) **442**, 54 (2006).

[56] M. W. Zwierlein, A. Schirotzek, C. H. Schunck, and W. Ketterle, Science **311**, 492 (2006).

[57] G. B. Partridge, W. Li, R. I. Kamar, Y. Liao, and R. G. Hulet, Science **311**, 503 (2006).

[58] C. Chin, R. Grimm, P. Julienne, and E. Tiesinga, Rev. Mod. Phys. **82**, 1225 (2010).

[59] S. Giraud and R. Combescot, Phys. Rev. A **79**, 043615 (2009).

[60] M. Ku, J. Braun, and A. Schwenk, Phys. Rev. Lett. **102**, 255301 (2009).

[61] G. M. Bruun and P. Massignan, Phys. Rev. Lett. **105**, 020403 (2010).

[62] S. Giraud and R. Combescot, Phys. Rev. A **85**, 013605 (2012).

[63] V. Ngampruetikorn, J. Levinsen, and M. M. Parish, Europhys. Lett. **98**, 30005 (2012).

[64] J. Levinsen and S. K. Baur, Phys. Rev. A **86**, 041602 (2012).

[65] J. Levinsen, P. Massignan, F. Chevy, and C. Lobo, Phys. Rev. Lett. **109**, 075302 (2012).

[66] R. Schmidt, T. Enss, V. Pietilä, and E. Demler, Phys. Rev. A **85**, 021602 (2012).

[67] J. Vlietinck, J. Ryckebusch, and K. Van Houcke, Phys. Rev. B **87**, 115133 (2013).

[68] A. L. Fetter and J. D. Walecka, *Quantum Theory of Many-particle Systems* (Dover Publications, 2003).

[69] M. E. Peskin and D. V. Schroeder, *An introduction to quantum field theory* (Addison-Wesley, Reading, 1995).

[70] M. Abramowitz, *Handbook of mathematical functions, with formulas, graphs, and mathematical tables* (Dover Publications, 1974).

[71] V. Pietilä, D. Pekker, Y. Nishida, and E. Demler, Phys. Rev. A **85**, 023621 (2012).

[72] L. D. Landau, E. M. Lifshitz, and L. P. Pitaevskii, *Statistical Physics, Part 2: Theory of the Condensed State*, Vol. 8 of Course of Theoretical Physics (Elsevier Butterworth Heinemann, Oxford, 1980).

[73] A. S. Mishchenko, N. V. Prokof'ev, A. Sakamoto, and B. V. Svistunov, Phys. Rev. B **62**, 6317 (2000).

[74] N. V. Prokof'ev and B. V. Svistunov, Phys. Rev. Lett. **81**, 2514 (1998).

[75] N. V. Prokof'ev and B. V. Svistunov, Phys. Rev. Lett. **99**, 250201 (2007).

[76] E. Kozik, K. Van Houcke, E. Gull, L. Pollet, N. V. Prokof'ev, B. V. Svistunov, and M. Troyer, Europhys. Lett. **90**, 10004 (2010).

[77] L. Pollet, N. V. Prokof'ev, and B. V. Svistunov, Phys. Rev. B **83**, 161103 (2011).

[78] K. Van Houcke, F. Werner, E. Kozik, N. V. Prokof'ev, B. Svistunov, M. J. H. Ku, A. T. Sommer, L. W. Cheuk, A. Schirotzek, and M. W. Zwierlein, Nat. Phys **8**, 366 (2012).

[79] S. A. Kulagin, N. V. Prokof'ev, O. A. Starykh, B. Svistunov, and C. N. Varney, Phys. Rev. Lett. **110**, 070601 (2013).

[80] S. A. Kulagin, N. V. Prokof'ev, O. A. Starykh, B. Svistunov, and C. N. Varney, Phys. Rev. B **87**, 024407 (2013).

[81] M. Jarrell and J. E. Gubernatis, Phys. Rep. **269**, 133 (1996).

[82] E. Kozik, M. Ferrero, and A. Georges, Phys. Rev. Lett. **114**, 156402 (2015).

[83] J. Levinsen and M. M. Parish, Annu. Rev. Cold At. Mol. **3** (2015).

[84] J. Vlietinck, J. Ryckebusch, and K. Van Houcke, Phys. Rev. B **89**, 085119 (2014).

[85] F. J. Dyson, Phys. Rev. **85**, 631 (1952).

[86] X. Cui and H. Zhai, Phys. Rev. A **81**, 041602 (2010).

[87] P. W. Anderson, Phys. Rev. Lett. **18**, 1049 (1967).

[88] D. M. Ceperley, Rev. Mod. Phys. **67**, 279 (1995).

[89] M. Boninsegni, N. V. Prokof'ev, and B. V. Svistunov, Phys. Rev. E **74**, 036701 (2006).

[90] S. Pilati, "Studies of ultracold gases using quantum Monte Carlo techniques", PhD thesis (Università degli studi di Trento, 2008).

[91] `https://github.com/agdelma/pimc-notes` (visited on 12/12/2016).

[92] P. Lévy, Compos. Math. **7**, 283 (1940).

[93] M. Boninsegni, N. V. Prokof'ev, and B. V. Svistunov, Phys. Rev. Lett. **96**, 070601 (2006).

[94] N. V. Prokof'ev, B. V. Svistunov, and I. S. Tupitsyn, Phys. Lett. A **238**, 253 (1998).
[95] M. Suzuki, Phys. Lett. A **201**, 425 (1995).
[96] S. A. Chin, Phys. Lett. A **226**, 344 (1997).
[97] N. V. Prokof'ev and B. V. Svistunov, Phys. Rev. Lett. **87**, 160601 (2001).
[98] V. G. Rousseau, Phys. Rev. B **90**, 134503 (2014).
[99] E. L. Pollock and D. M. Ceperley, Phys. Rev. B **36**, 8343 (1987).
[100] M. Holzmann and Y. Castin, Eur. Phys. J. D **7**, 425 (1999).
[101] G. Giuliani and G. Vignale, *Quantum Theory of the Electron Liquid* (Cambridge University, Cambridge, 2005).
[102] B. Capogrosso-Sansone, S. Giorgini, S. Pilati, L. Pollet, N. V. Prokof'ev, B. Svistunov, and M. Troyer, New J. Phys. **12**, 043010 (2010).
[103] F. Cinti, P. Jain, M. Boninsegni, A. Micheli, P. Zoller, and G. Pupillo, Phys. Rev. Lett. **105**, 135301 (2010).
[104] S. Saccani, S. Moroni, and M. Boninsegni, Phys. Rev. B **83**, 092506 (2011).
[105] M. Boninsegni, J. Low Temp. Phys. **168**, 137 (2012).
[106] M. Rossi, S. L. Zavattari, D. E. Galli, and L. Reatto, Phys. Rev. B **84**, 052504 (2011).
[107] L. P. Pitaevskii, Sov. Phys. JETP **13**, 451 (1961).
[108] E. P. Gross, J. Math. Phys. **4**, 195 (1963).
[109] D. A. Kirzhnits and Y. A. Nepomnyashchii, Sov. Phys. JETP **32**, 1191 (1971).
[110] Y. A. Nepomnyashchii, Theor. Math. Phys. **8**, 928 (1971).
[111] Y. A. Nepomnyashchii and A. A. Nepomnyashchii, Theor. Math. Phys. **9**, 1033 (1971).
[112] C. Josserand, Y. Pomeau, and S. Rica, Phys. Rev. Lett. **98**, 195301 (2007).
[113] F. Cinti, M. Boninsegni, and T. Pohl, New J. Phys. **16**, 033038 (2014).
[114] W. R. Magro and D. M. Ceperley, Phys. Rev. B **48**, 411 (1993).
[115] O. N. Osychenko, G. E. Astrakharchik, F. Mazzanti, and J. Boronat, Phys. Rev. A **85**, 063604 (2012).
[116] J. Cardy, *Scaling and Renormalization in Statistical Physics* (Cambridge University, Cambridge, 1996).
[117] N. D. Mermin and H. Wagner, Phys. Rev. Lett. **17**, 1133 (1966).
[118] P. C. Hohenberg, Phys. Rev. **158**, 383 (1967).
[119] S. Coleman, Comm. Math. Phys. **31**, 259 (1973).
[120] `http://www.nobelprize.org/nobel_prizes/physics/laureates/2016/advanced-physicsprize2016.pdf` (visited on 12/12/2016).
[121] V. L. Berezinskii, Sov. Phys. JETP **32**, 493 (1971).
[122] J. M. Kosterlitz and D. J. Thouless, J. Phys. C: Solid State Phys. **6**, 1181 (1973).
[123] M. Boninsegni, N. V. Prokof'ev, and B. V. Svistunov, Phys. Rev. Lett. **96**, 105301 (2006).
[124] S. Moroni and M. Boninsegni, Phys. Rev. Lett. **113**, 240407 (2014).
[125] L. A. P. Ardila and S. Giorgini, Phys. Rev. A **92**, 033612 (2015).
[126] F. Schwabl, *Quantum Mechanics* (Springer, 2007).
[127] S. K. Adhikari and W. G. Gibson, Phys. Rev. A **46**, 3967 (1992).